2D DC Resistivity modeling for anisotropic subsurface with variable topography based on mimetic finite-difference method

विद्या वाचस्पति की
उपाधि की अपेक्षाओं की आंशिक पूर्ति में प्रस्तुत शोध प्रबंध

A thesis submitted in partial fulfillment of the requirements of the degree of Doctor of Philosophy

द्वारा
दीपक सूर्यवंशी

By
Deepak Suryavanshi

पंजीकरण सं. / Registration No.: **20183581**

शोध प्रबंध पर्यवेक्षक / Thesis Supervisor
Dr. Rahul Dehiya

IISER PUNE
भारतीय विज्ञान शिक्षा एवं अनुसंधान संस्थान पुणे
INDIAN INSTITUTE OF SCIENCE EDUCATION AND RESEARCH PUNE

2024

Certificate

Certified that the work incorporated in this thesis entitled ' 2D DC Resistivity modeling for anisotropic subsurface with variable topography based on mimetic finite-difference method' submitted by Deepak Suryavanshi was carried out by the candidate under my supervision. The work presented here or any part of it has not been included in any other thesis submitted previously for the award of any degree or diploma from any other University or institution.

Dr. Rahul Dehiya
Thesis Supervisor
Indian Institute of Science Education and Research
Pune, Maharashtra

Date: April 8, 2024

Declaration

I declare that this written submission represents my ideas in my own words and where others' ideas have been included, I have adequately cited and referenced the original sources. I also declare that I have adhered to all principles of academic honesty and integrity and have not misrepresented or fabricated or falsified any idea/data/fact/source in my submission. I understand that violation of the above will be cause for disciplinary action by the Institute and can also evoke penal action from the sources which have thus not been properly cited or from whom proper permission has not been taken when needed.

Deepak Suryavanshi
Roll no. - 20183581

Date: April 8, 2024

Dedicated to “Dada ji, Papa, Mummy, and Neha"

Abstract

The Direct Current (DC) resistivity method is a classical geophysical method to obtain subsurface geoelectrical images. This technique is utilized in groundwater, mineral mapping, subsurface pollution monitoring, saltwater intrusion and other civil engineering applications, where a reliable data analysis requires a versatile and robust forward modeling algorithm. The present study develops a 2-dimensional (2D) DC resistivity forward modeling algorithm employing mimetic finite difference methods (MFDM). The MFDM preserves the valuable properties of the continuum governing partial difference equation in discrete space, leading to a better representation of actual electrical potential by simulated potential. This study presents the first application of MFDM for DC resistivity modeling. The accuracy of the developed scheme is benchmarked utilizing analytical responses of a dyke model and two-layer anisotropic models. Since there are no analytical solutions for the variable topography cases, the accuracy of the scheme is demonstrated by comparing the solution with the published responses. A three-layer model is used to examine the stability of the devised algorithm by incorporating non-orthogonal grids. Non-orthogonal grids are produced by randomly varying the nodal coordinate of orthogonal grids. The observed error trends show that the algorithm is highly stable with regard to grid distortion and can accurately simulate complicated models involving topography and anisotropic subsurface. Furthermore, the numerical computation time analysis reveals that the developed algorithm is computationally stable to grid distortion.

To efficiently accommodate the 3D character of the source in a 2D DC resistivity modeling, a new space domain approach is devised in this study. The developed algorithm is valuable in the case of long current-potential electrode spacing, including the case of high resistivity contrast and anisotropic subsurface. A half-space model was employed to examine the limitations of various wavenumber schemes. In the case of wavenumber-based modeling techniques, these wavenumber schemes are used in inverse cosine transform needed for space domain computation. It was observed that after a particular offset, all the wavenumber schemes deviated from the analytical result except the Gauss quadrature method with 120 wavenumbers, suggesting the long offset data requires simulation of large wavenumbers. Consequently, the wavenumber scheme becomes computationally

expensive in the case of long offset simulation. Motivated by this analysis, a space domain modeling algorithm that utilizes a new boundary condition applicable to the plane that passes through the source position is developed. The proposed approach is computationally competitive with the wavenumber domain approach. It is likely to be even more efficient in case of large offsets as a small number of grids are sufficient to discretize the space in the strike direction. Extensive numerical simulations are carried out to demonstrate that the developed method is reliable and versatile for deep imaging surveys having variable topography and anisotropic subsurface, including tilted transversely isotropic cases.

The construction of an algorithm based on a modified boundary condition, which aids in overcoming the wavenumber problem and gives accurate solutions for huge offsets, can be used as an essential tool to study responses for geophysical models till large offsets. Hence, we use the developed algorithm to obtain azimuthal apparent resistivity curves for various two-layered models, including isotropic, tri-axial anisotropic, and tilted transversely isotropic (TTI) models. The simulated azimuthal apparent resistivity plots provide insight into the scenarios when these plots behave like an isotropic case, even in the case of anisotropic subsurface. Further, the sensitivity curves are generated by taking the derivatives of apparent resistivity values with respect to the parameters that govern anisotropy. It is found that for a 2D case, the DC data generally shows sensitivity to all four parameters governing the anisotropy, which include the three principal resistivity values and one angle defining the angle of the tilted symmetry of anisotropy. However, when the azimuthal apparent resistivity plot evolves circularly, the principal resistivity along the profile direction becomes insensitive to the observed data.

Acknowledgements

I want to express my gratitude to my supervisor, Dr. Rahul Dehiya, an outstanding mentor who provided me with a dynamic lab environment, invaluable insights, and the opportunity to grow during my PhD at IISER Pune. I am grateful to have had a mentor who encouraged me to set high standards for myself and work hard and regularly to achieve them. He set examples for developing new ideas and to implement them with perfection. He also taught me to handle failures, step back, reflect, and keep trying until I succeed. He gave me a lot of motivation and encouraged me to aim for excellence, which helped me develop both personally and professionally. Being among the first students in the lab and seeing it grow was a unique experience for me during my doctoral research.

I am also grateful to my research advisory committee members, Prof. Shyam Rai and Prof. Pravin Gupta, for their insightful comments and viewpoints during my yearly presentations. They were always readily available, participated in in-depth conversations, provided valuable information, and made insightful recommendations. I would also like to thank Prof. Arun Singh for joining one of my RAC seminars and giving me helpful advice.

Furthermore, the welcoming and supportive lab members provided a stimulating environment suitable for research advancement. I consider myself fortunate to have these buddies. Every person in the lab has never failed to go above and beyond to assist me in solving any problems I have encountered with my work. I want to express my gratitude to Iktesh, Rashi, Vivek, and Sujith for making the lab a fun place to work.

Together with my PhD batchmates, I had a great time. Attended classes together with Amrita, Akash, Niyor, Smruti, Prayas, JD, Devesh, Arijeet, and Shubhangi and had endless conversations about science and life. Special appreciation to Sarang, Kashyap, Devansh, Niyor, Bhavin, Yogesh, Saurabh bhaiya, Rajat, Nitesh, Ravi, Dhruv, and Suraj for always supporting me throughout. I share a special bond with my IISER TVM friends Sarang, Niyor, and Devansh, who have all been a part of my daily life for a very long time. A special shout out to my school friends Kashyap, Sanjana, Ashish, Sidharth, Narender, and Rajni for helping me during the difficult times of my PhD. My evening walk buddies in IISER Pune, Iktesh and Suraj, deserve a special mention. My trekking group with Dipjyoti,

Nitesh, Chitra, Shobhit, Saurabh, and others also played an important role during my PhD journey.

I am grateful to IISER Pune for giving me a chance to complete my Ph.D. study here and for the institute fellowship that supported me throughout my time. I also want to thank IISER Pune's ECS Department for their resources and assistance. I want to express my profound appreciation to my ECS office coworkers, Vibhas, Vikrant, and Ruby, for their support throughout my doctoral journey.

It also makes me happy that I have a battalion of supportive and caring cousins and relatives who helped me get here by offering guidance and inspiration. I want to express my heartfelt gratitude to Amit, Akash, Priya didi, and Rajni for never losing faith in me and always being there.

Above all, none of this would have been possible without my family, including my grandfather, father, mother, and my wife Neha. My parents have always been a source of strength and support for me in all of the decisions I have made in life. I cannot even begin to express how much my parents have given me, but I can tell that they have always supported me and done everything they could to help me when I was lost. My gratitude for Neha, my better half, who has supported me through all of my hardships and never lost trust in me, is beyond words. I can't help but be grateful for her effort to put a smile on my face in difficult situations. Neha, thank you so much for everything. She is a wonderful partner on this exciting journey through life. This dissertation is an expression of the enduring love, constant inspiration, and support I have received from my family.

Deepak Suryavanshi

Table of contents

List of figures

Chapter 1

Introduction

The Direct Current (DC) resistivity method is a classical geophysical technique used for subsurface imaging, particularly near-surface investigations. It is employed for deciphering the variations in the electrical resistivity of the subsurface. DC resistivity has a history of more than a century. Since its inception, it has evolved immensely in instrumentation, survey design, and data analysis. This chapter presents an overview of the DC resistivity method with particular emphasis on numerical modeling, which plays a vital role in data analysis.

1.1 Fundamental Relations and Mathematical Basis of the DC resistivity Method

The foundational principle governing the DC resistivity method is Ohm's law, which describes the relationship between electrical current (I), voltage (V), and resistance (R), where the resistance is a constant for an object, and it depends on the electrical property and geometry of the object. Since the shapes of the subsurface anomalies are not known before geophysical investigations, the resistance is of little use in these studies. Therefore, a more general form of Ohm's law, which relates the current density, **J**, electric field intensity, **E**, via the electrical conductivity, σ, is used in DC resistivity data analysis, and this relation is given as [37],

$$\mathbf{J} = \sigma \mathbf{E}. \tag{1.1}$$

For brevity, the electric field intensity and electrical conductivity are referred to as electric field and conductivity, hereafter, in this thesis. The current density and electric field are vector quantities, and the conductivity is a second-order tensor. For operational pur-

poses, working with potential differences rather than an electric field is more convenient. Therefore, it is instructive to write the above equation in terms of electric potential. It is achieved by the relationship that connects electric field to the negative gradient of a potential, u, and it can be written as,

$$\mathbf{E} = -\nabla u. \tag{1.2}$$

Furthermore, using equation of continuity and principle of conservation of charge, we can write,

$$\nabla.\mathbf{J} = f, \tag{1.3}$$

where f depends on the externally applied known electric field, which is measured (consequently known) in terms of applied electric current in the DC resistivity method. The above three equations can be combined to write a partial differential equation for potential as,

$$-\nabla.\sigma\nabla u = f. \tag{1.4}$$

The equation 1.4 is solved under appropriate boundary conditions. Since the physical laws state that no current can flow across the earth-air interface (say, Γ_s), hence the boundary conditions on Γ_s are given by,

$$\frac{\partial u}{\partial n} = 0, \text{ on } \Gamma_s, \tag{1.5}$$

where n is the outward unit normal on the ground surface Γ_s. The homogeneous Dirichlet boundary conditions (i.e., the potentials are set to zero) or Neumann boundary conditions can be applied to the other domain boundaries. However, it is observed that these assumptions result in under or overshooting of potentials, respectively, in the numerically calculated potentials at a certain distance from the point source [28]. Because of this, [37] suggested mixed boundary conditions based on the potential's asymptotic behavior and gradient at vast distances from the point source. Therefore, the solution of equation 1.4 under appropriate boundary conditions provide the potential distribution, u, in the region having conductivity given by σ due to an external source expressed by f. An alternative material property referred to as resistivity is generally used in DC resistivity methods, which is simply defined as the inverse of conductivity as,

$$\sigma = \frac{1}{\rho} \tag{1.6}$$

The objective of a DC resistivity experiment is to obtain the subsurface resistivity (or conductivity) image, which is subsequently interpreted in terms of subsurface geology fluid type/saturation, etc. Next, the section presents a brief summary of its application in subsurface imaging.

1.1.1 Applications

DC resistivity has a wide range of applications in scientific research and practical domains. Initial applications were mineral exploration and hydrocarbon investigation, and it led to the birth of one of the most successful oil and gas service companies, SLB, starting with the DC resistivity application pioneered by the Schlumberger brothers [33]. With time, it has extended into environmental studies like aquifer protection studies [20] and study of waste disposal site and its environments [5, 121], civil engineering studies [58] like building site investigation [107] and pavement engineering [1], archaeological investigations like findings of archaeological targets [39], geothermal resource assessment [133] like exploring geothermal reservoir and physical parameters of the host rock [75], critical zone study involving the influence of subsurface heterogeneity on critical zone characterizations [27], and geological hazard monitoring like water inrush in tunnels and coal mines [84]. The current's penetration depth in the subsurface increases with the distance between current injection points [30] and also depends on the conductivity distribution of the underlying medium. Generally, the depth of investigation is around one-third to one-fifth of the current injection point separation. The greater the separation between current source points, the stronger the current must be injected to be recorded faithfully. Consequently, the applications of DC resistivity methods primarily lie in near-surface investigations. The subsurface imaging in the DC resistivity method also depends on the survey design. The following subsection briefly reviews the survey design and data acquisition.

1.1.2 Survey Setup, Configurations & Data Acquisition

The field measurement of the DC resistivity method involves measuring the potential differences induced by a controlled electric field [30]. The electric field is generated by injecting the electric current into the ground by the current electrodes connected to a battery that supplies the current. The current electrodes are also connected to an ammeter for measuring the injecting current. The voltmeter is used to estimate the potential difference between electrodes, referred to as potential electrodes. There are two types of electrodes, namely polarizing and non-polarizing [78]. Non-polarizing electrodes

overcome the issue of charge accumulation at the electrode; hence, they are superior. However, they are costly and delicate to handle. Therefore, most of the time, polarizing electrodes are used until the survey needs to take care of charge accumulation. Advanced equipment includes a data logger and multichannel system that significantly speeds up the data acquisition, which is essential for 2- and 3-dimensional surveys [90, 134].

The current and potential electrodes can be arranged in various configurations. The electrodes may be placed arbitrarily or in a co-linear fashion. Some of the notable array configurations are cited here. Wenner Array: This array is widely used for general resistivity surveys and involves four equally spaced electrodes. The outer electrodes serve as current sources, while the inner electrodes measure voltage. Schlumberger Array: Suitable for deep resistivity investigations, this array employs a fixed-spacing configuration with adjustable electrode spacings, enabling measurements at various depths. Dipole-Dipole Array: For high-resolution surveys, the dipole-dipole array features a pair of current electrodes and two pairs of voltage electrodes, facilitating detailed subsurface information. Pole-Pole Array: One of the potential electrodes and one of the receiver electrodes are both moved to infinity in a pole-pole survey but in different directions. To put it another way, a stationary infinity electrode is placed on either side of the survey region in a pole-pole array. More details on these arrays can be found at [78, 143]. The following factors influence the survey geometry selection: (1) the desired conductivity structure, the horizontal and vertical resolution being the most important factor; (2) field limitations for electrode placement; (3) noise floor in the survey area; (4) depth of investigation; and (5) time available for acquisition.

Various survey types can be designed, employing the above-mentioned array(s) to meet the survey objective, such as obtaining 1-, 2- or 3-dimensional resistivity images of the subsurface. The 1-dimensional (1D) survey is generally referred to as sounding, where measurement is made of various current/potential electrodes separations around a fixed center to obtain the resistivity variation with depth [13, 173]. The change in the horizontal direction is mapped by moving a fixed array along a line, which is known as profiling [3, 8]. A combination of sounding and profiling led to a 2D survey when data is recorded along a profile, and if measurements are made over a surface area, it leads to a 3D survey [76]. 2D data acquisition delivered the subsurface resistivity details below the profile, while 3D provided the resistivity information in volume below the survey plane. The 3D survey is generally expensive due to the requirement of equipment and survey time. Generally, for research purposes, 2D surveys are conducted [2, 9, 147].

DC Resistivity data are presented either as resistance, defined as a ratio of voltage differences by current, or as apparent resistivity values, ρ_a, defined as,

$$\rho_a = K.\frac{\Delta V}{I}, \tag{1.7}$$

where K is a geometric factor that depends on the electrode configuration. The apparent resistivity has the same unit as resistivity, and it is identical to the true resistivity of the subsurface in the case of half-space. The apparent resistivity is often represented by pseudosections for 2D and 3D cases [4, 8, 38]. These measurements are transformed into subsurface resistivity models using inverse modeling during interpretation.

1.1.3 Interpretation

Once the resistivity surveys are done, the final step is to estimate the true distribution of intrinsic resistivities [126]. The first step is to analyze the pattern of apparent resistivities that were measured. It is instructive to plot apparent resistivities as pseudosections. The pseudosections are helpful in identifying abnormalities in the data, identifying defective electrodes, and verifying any normalizations that may have been done. However, it has to be kept in mind that pseudosection is not a true geological cross-section and should not be interpreted as a subsurface image [48, 69].

Inversion algorithms [23] are employed to estimate subsurface resistivity models using observed data [50, 96]. It generally delivers a smooth model due to the regularization needed to stabilize the inversion that attains a pre-assigned misfit tolerance to observed data [49, 145]. The inverted models are interpreted by building a subsurface geological model [131, 149] by utilizing the subsurface resistivity distributions and any other information available about the study area. The geological models are further used to prove or falsify the hypothesis that exists of the problem being investigated [104, 162]. Therefore, the final outcome depends heavily on the accuracy of inversion. The DC resistivity inversion [102, 132] is a non-linear optimization problem [50, 123]. This entails creating a model from raw data and fine-tuning the inversion until measured data and calculated data agree well. There are various inversion schemes that have been utilized for DC resistivity studies [18, 120]. Irrespective of the scheme, an inversion involves several forward modeling computations that involve simulation data for a given model [98, 166]. Furthermore, the efficiency, accuracy, and robustness of the forward modeling algorithm are the primary factors in a successful inversion algorithm. Consequently, it plays a vital role in DC resistivity data analysis. The focus of this thesis lies in the development of a forward modeling algorithm for the DC resistivity problem. Therefore, a detailed review of DC modeling is presented in the next section.

1.2 Forward Modeling of DC resistivity Data

The equation 1.4 is the mathematical formulation for the DC resistivity problem, which has to be solved for the unknown potential u. The analytical solution of this equation is only possible for some very simple models [11]. For the 1D models, semi-analytical solutions are preferred [119, 125]. For a general subsurface conductivity distribution and arbitrarily shaped boundary, numerical methods are adopted to obtain an approximate solution. Numerical methods try to find an approximate solution of the governing partial differential equation under the suitable condition applied to the computation domain. Some of the commonly used numerical methods for DC resistivity modeling are,

- Finite Difference Method (FDM) [135, 168]
- Integral Method [59, 148]
- Finite Element Method (FEM) [136, 160]
- Meshless Method [81, 93]

Some of the chief challenges encountered in DC resistivity modeling are field singularities at the source location, enormous conductivity contrasts, complex geometries of heterogeneity, rugged topography, and anisotropy. Some of these complications also affect the choice of numerical methods. Therefore, we first present a discussion on source singularity, variable topography and electrical anisotropy.

1.2.1 Source Singularity & Topography

The steep gradient of the potential field occurs where the source is placed in the modeling domain. Furthermore, at the position of the source, the potential is undefined or a singularity. The occurrence of singularity at the source position poses challenges for any approximation of source term using discrete points. Therefore, various approaches have attempted to overcome the problem of representing the Dirac delta function by discrete points. The modeling scheme where the Dirac delta function is approximated by discrete points delivers approximate total potential due to the source for the given model. Therefore, such schemes are also known as the total potential approach or the total field approach. Such schemes have been used in many studies on DC resistivity forward modeling [41] and consequently in inverse modeling [47, 47, 170]. These approaches may result in relatively large errors around the source position because the source is

not adequately represented on a discrete grid [168]. The accuracy depends on the local refinement around the source, and accuracy generally demands very fine grids near the source position. The problem arises when the source location is shifted to multiple points within the model domain, for example, in the case of 2D/3D inverse modeling of DC resistivity data. This creates very fine grids at multiple locations in the modeling domain, thereby increasing unnecessary computational costs. Consequently, in the case of inversion, using a total filed approach necessitates a source-specific discretization to make the inversion computationally tractable. In turn, source-specific discretization requires separate discretization for forward and inverse modeling and interpolation between the forward grid and the inversion grid of the potential values and conductivities.

An alternative approach to the singularity removal method is called the primary-secondary decomposition approach, also known as the secondary field approach. In this technique, the potential term is split into primary and secondary potentials, given by $u = u_p + u_s$, where u_p is the primary potential and u_s is the secondary potential. u_p is potential due to the source for a background conductivity σ_p for which analytical/semi-analytical solution is possible. The two most common choices for background conductivity are half-space or a stack of horizontal layers. The secondary potential is computed by solving the governing equation for subsurface conductivity due to a scattered source that depends on the primary potential and anomalous conductivity, which is defined as $\sigma - \sigma_p$. The background conductivity is chosen such that the anomalous conductivity vanishes at and around the source location. Such a choice of background conductivity causes a smooth scattered source term, which can be approximated on relative coarse discretization compared to one needed total source formulation. This process, known as the secondary potential approach or singularity removal technique, was given by [91, 168]. This singularity removal technique greatly increases the accuracy of the numerical results [86, 112, 117, 156]. However, in the case of variable topography, there is no analytical formula to obtain the primary field.

1.2.2 Electrical Anisotropy

Anisotropy refers to the direction dependency of physical property. Earth material shows the anisotropic nature of most of its physical properties, including electrical conductivity. It is frequently seen in rock with prominent lineation, such as slate, shale, and clay, as well as in platy fabrics. Rock texture and crystal symmetry have an impact on its intrinsic anisotropy, also known as micro-anisotropy. When a stack of layers of different isotropic materials senses like a single unit to any geophysical method due to their resolution power, it manifests a macroscopic anisotropy. Rock cleavage, jointing, and fracture can all cause

structural anisotropy, which results in anisotropic resistivities in the subsurface (rock and joint fill).

The true ground resistivities and the geologic structure inferred from the DC resistivity data may be inaccurate if anisotropy in the ground is present but is disregarded during data analysis. According to [154], anisotropy's influence shouldn't be disregarded even if it is around 1.1. The assumption of electrical isotropy of the medium has been made in many of the studies about subsurface heterogeneity mapping. It is erroneous to make such an assumption when working with stratified, fractured, and jointed rocks. A homogeneous anisotropic half-space with different electrode arrays and their depth of investigation was examined by [12]. A few papers that address the impact of anisotropy on surface resistivity measurements include [53, 54, 97]. The problem of investigating anisotropic resistivity in boreholes has been examined by [6, 99]. To address anisotropic circumstances quantitatively, researchers have also created imaging and inversion programs [56, 77, 108]. However, the anisotropic inversion is a challenging task, particularly in the case of the tilted symmetry axis case. The absence of anisotropic resistivity imaging has been attributed to several significant factors, including (i) the need to estimate extra parameters during the inversion of an often under-determined problem, (ii) the difficulty of defining the form of anisotropy in the initial model, and (iii) the inability to detect anisotropy from surface field measurements [47]. Nonetheless, the most crucial element of an inversion algorithm is accurate and efficient forward modeling. In the case of an anisotropic inversion algorithm, forward modeling should be able to simulate the response of the anisotropic subsurface.

1.2.3 Numerical Methods

Even though many numerical techniques have been implemented for DC resistivity modeling, the FEM [15, 28, 114] and the FDM [37, 91, 135] are two methods that are utilized extensively. The FDM is straightforward to implement and, therefore, employed most frequently, particularly in initial studies. However, FDM works with structured (more specifically orthogonal) grids, severely restricting their ability to handle variable topography. Another problem with FDM is that grid refinement can not be limited to a particular region as the orthogonal grid extends up to the boundaries, which leads to unnecessary refinement to a bigger subdomain. On the other hand, FEM can be adapted to varying topography as it allows one to choose various shapes of elements that can have varying sizes in the modeling domain. This flexibility in discretization allows for problem-specific refinement of the modeling domain. However, it is not trivial to obtain the optimum discretization, and it may depend on issues such as current and potential electrodes' position apart from the topography and the conductivity distribution in the subsurface.

Therefore, code development and discretization are challenging issues in FEM algorithm development.

The apparent resistivities derived from DC resistivity studies are significantly influenced by topography. A ridge can result in a high resistivity zone directly beneath the ridge, and a valley can cause low resistivity anomalies beneath it [42, 144]. These artifacts have the potential to produce a false interpretation. Therefore, topography needs to be considered during modeling to prevent artifacts [40]. Since the EFM allows greater flexibility in discretization, the handling of topography is easy to accommodate in the FEM algorithms. Therefore, FEM has been used by many studies in DC resistivity modeling when topography is included [40, 42, 86, 89, 144]. On the other hand, in case of FDM, the topography needs to be represented by a staircase approximation, which may be a good approximation for gentle topography. Generally, the number of unknowns is much higher in EEM than in FDM for numerical accuracy acceptable in geophysical modeling, particularly for flat or mild topography. Thus, the FDM general scores higher in efficiency; hence, the FDM technique is preferred if the topography is simple [40, 86]. Therefore, attempts have been made to modify the FDM such that it can handle rugged topography. [40] employed a triangular discretization with FDM at the air/earth interface instead of the more popular rectangular discretization. Their method yields slightly less accuracy than the FEM distorted-mesh, but triangular FDM is still as accurate as triangular FEM. But compared to both FEM, their triangular FDM algorithm operates much more quickly. When topography is present, [138] used a coordinate transformation on the FDM mesh to improve the accuracy of their solutions. Coordinate transformation is a concept that was previously applied to electromagnetic modeling by [7] to include seafloor topography.

An additional method of incorporating topography is presented by [146]. This study presents a hybrid finite difference–finite element approach, sometimes known as a hybrid finite difference - finite element (FD–FE) or, short, HB. Where topography exists, the rectangular FD nodes at the air/earth interface are replaced with triangular FE components. The FDM and FEM systems of equations are combined to form the system of equations for this hybrid approach. A hybrid system of equations is thus closer to the FD system of equations since FD is employed inside the model while FE is mostly used at the earth's surface. As a result, while HB's computing time is closer to FDM's, its numerical precision is identical to FEM's. Hybrid forms of FDM and FEM methods have also found applications in practical scenarios such as elastic wave modeling [44, 73] and applications in hydrology [130]. FDM and FEM are both methods of approximation. It has been demonstrated that when applied to the same grid, both FE and FD produce comparable discrete approximations [172]. This information is vital for the hybrid approach. A hybrid approach would

not work if there were any significant discrepancies between the two approximations. In this situation, it is necessary to provide a transition zone between FDM and FEM, and vice versa [44].

As the FEM method allows refinement in a user-defined region during the discretization, hence it can be employed more efficiently for total field formulation for source singularity than FDM because the refinement in a localized region extends to a large domain in FDM. However, the primary and secondary approaches allow coarser discretization near the source location; hence, this is a manageable problem for FDM if the primary field is efficiently computable, therefore, variable topography case is a challenging problem to be solved using primary and secondary approach. For uneven topography, a scheme suggested by [51], where the elements whose resistivities need to be found are defined by a relatively coarser parameter grid. A secondary potential approach is used for the forward calculations in each inversion step on the secondary field grid. At the start of the inversion process, a one-time simulation on the highly refined primary field grid provides the primary fields. An alternate technique to deal with cases involving topography was given by [112]. In this method, a modified boundary condition is used, and the primary field is taken as per the half-space.

The handling of electric anisotropy, which has been observed in both field and laboratory measurements, is another crucial problem in modeling DC resistivity data. According to [103], naturally occurring rock can have an anisotropy factor of up to 4.5. Significant errors will occur if these anisotropic structures are regarded as isotropic [6, 165]. Numerical codes must be able to manage anisotropy to interpret anisotropic structures. Analytical solutions exist for simple anisotropic models like the anisotropic layered media [150, 164] and the tilted transversely isotropic (TTI) uniform half-space [54]. For benchmarking, [82, 83] provided analytical solutions for several basic anisotropic models. Solutions for simple anisotropic models can be derived by analytical approach [46], however, for arbitrary distribution of resistivity numerical methods are used [56, 87, 108, 165, 170]. Electric anisotropic media were also considered by [57, 151] using FDM techniques and by [14, 87] employing FEM approach. [87] used a FEM approach for modeling anisotropic resistivity with structured hexahedral grids. [85] took anisotropy into account using adaptive finite elements. Other numerical simulation schemes for anisotropic models have been attempted using volume integral methods [82, 83], the spectral element methods [170]. To calculate the response of anisotropic structures, [170] used the "Gaussian quadrature grid," a modified version of the spectral element method.

FDM and FEM have been compared by Li and Spitzer [86] for three-dimensional DC resistivity forward modeling. Also, there has been a comparison study by Osiadacz and

Yedroudj [106] in the case of a simulation for a gas pipeline. These studies highlight that although FEM is quite accurate in terms of numerical approximation, it turns out to be computationally expensive. Also, if there is further refining required of the grid, the number of variables increases manifold in the case of a FEM approach. In such a scenario, the computation time and storage space demand for FEM will increase. These studies also comment upon the robustness of these approaches and clearly state that FDM is quite robust compared to FEM, especially concerning coarsening of the grid. Hence, slight changes in parameters would render the FEM scheme more erroneous than FDM. On comparing the memory requirements, it was observed that space taken by the FEM scheme is 3.4 times the requirement of the FD scheme [86]. Hence, we examine another novel numerical scheme known as the mimetic finite difference method (MFDM) that has the properties of both FDM and FEM.

1.2.4 Mimetic Methods

Numerical modeling problems involving complex physical processes, discontinuities, and strong nonlinearities must be solved using a numerical method that is robust and accurate to address these challenges because numerical approximation is a decisive factor for the simulations' efficiency, precision, and reliability. The predictions and insights obtained by the numerical simulation should be a good representation of the physical processes being examined. When the discrete representative mimics or preserves the underlying mathematical features of the physical system, the best outcomes are expected to be achieved. On general meshes, the MFDM aims to produce discrete approximations of the continuum operators that maintain important characteristics of continuum equations [26].

The mimetic discretizations started around the middle of the 1970s. The need to solve complex PDEs with discontinuous coefficients on non-orthogonal meshes was a major driving factor. The mimetic technique has been used to address various real-world problems, such as the diffusion equation [61, 62, 100], the gas dynamics equations [24], the equations of continuum mechanics [95], Maxwell's first-order curl equations [67], and the equations of magnetic diffusion [67]. Complexly shaped domains, several linked physical processes (such as heat conduction, gas dynamics, and electromagnetism), and the Lagrangian approach in which the mesh moves with fluid are also studied using mimetic methods.

MFDMs are also known as support-operator methods, basic or reference operators in literature [129]. The method of support operators is described in detail in [122, 127, 128]. As per the construction of mimetic operators, every discrete operator has an invariant def-

inition, meaning coordinate invariant values like volumes, areas, and angles are included in the definitions. It means that the discrete operators can be applied in any coordinate system by modifying the formulas for these geometric values. After establishing the fundamentals of support-operator methods, it is possible to demonstrate that the discretized problem shares many significant properties with the original continuum problem by using discrete analogs of continuum operator identities. For the above reasons, the difference schemes developed are considered to be a family of mimetic methods [63, 128].

Selecting a discrete representation of the scalar, vector, and tensor fields on a computational mesh using appropriate degrees of freedom is the first step in building a mimetic discretization [17]. The discrete operators work on the grid functions and match the first-order continuum operators like the gradient, curl, and divergence. Firstly, the relationships between a mathematical model's most critical analytic features and the first-order differential operators are determined to serve as its formulation [29]. An integral identity typically expresses a duality relationship between the first-order operators. Depending on the problem at hand, a discrete form is selected for a few first-order operators, referred to as the primary operators. The other operators are constructed using the primary operators, referred to as the secondary or derived operators [60].

The grids used with mimetic methods are produced via smooth mappings; as a result, every cell is convex and resembles a slightly distorted rectangle [21]. The best rough grids are produced by moving the node randomly by a tiny amount while maintaining the convexity of all the cells, starting with a basic uniform grid. No matter how rough the grids are, the approach works incredibly well for grids with convex cells [79]. The only issue is that the iterative matrix solution might not converge for grids with nonconvex cells. However, there are revised algorithms to address this issue that are more reliable for such cases. Discussion of such algorithms is not within the scope of this thesis.

The conductivity discontinuities in the studies that are taken into consideration are just straight line jumps across the interface [88]. The theory of interfaces suggests that the normal flux is continuous at such interfaces. In summary, MFDMs are a special class of methods that guarantee the scheme to be conservative and second-order accurate; the system matrix formulated is symmetric and positive-definite for Dirichlet, Neumann, and Robin boundary conditions. MFDMs rigorously handle the discontinuities in the physical properties across interfaces. Moreover, the integral identity imposed over the discrete operators guarantees that the primary and secondary operators are dual to each other [67].

1.2.5 Wavenumber Domain

Two-dimensional DC resistivity modeling involves the potential simulation due to the point source for the subsurface model, where conductivity varies in two dimensions only, say $\sigma = \sigma(x,z)$. However, the 3D nature of the source causes the potential to be the function of three-dimensional space coordinates. Hence, the problem remains 3D in the space domain [19, 32]. However, the problem can be transformed in the wavenumber domain using the Fourier transform in the direction in which the conductivity is invariant [113, 146]. It leads to a PDE with two space variables, though it depends on the wavenumber. Therefore, the space domain response can be efficiently obtained by first performing a simulation in the wavenumber domain followed by taking the inverse Fourier transform of the wavenumber domain responses [31, 109]. A useful characteristic of potential for the 2D conductivity model is that the potential is symmetric about the plane perpendicular to the strike direction that passes through the source position. Further, the electric potential is real quantity. The above-mentioned properties of potential lead to further simplification of the Fourier transform to the cousin transform. The forward and inverse cosine transform defined is simply given as [36],

$$F(x,k,z) = \int_0^{+\infty} f(x,y,z)\ cos(ky)\ dy \tag{1.8}$$

and

$$f(x,y,z) = \frac{2}{\pi} \int_0^{+\infty} F(x,k,z)\ cos(ky)\ dk, \tag{1.9}$$

respectively, where k is the wavenumber. Since the potential in the DC resistivity method varies smoothly in space, it approaches zero as one increases the wavenumber. Therefore, the upper limit of the Fourier transform turns out to be a finite value, making numerical calculation of inverse Fourier transform practical. However, choosing optimum wavenumbers is a non-trivial task to perform 2D DC resistivity modeling. Various researchers have tried to come up with efficient schemes to choose the best schemes for selecting the optimum k values. To select the best values of k, [157] used an optimization approach, where he used a two-step gradient-based optimization technique to handle discrete wavenumbers and associated weights at distinct places. In the first step, the linear least-squares approach is used to determine the associated weights, followed by the second step, which uses the non-linear least-squares method to get the optimal k for the acquired weights. The ideal k and weights that cause the objective function to attain a minimum can be found after a sufficient number of repetitions.

In order to solve the non-linear optimization problem for estimating the appropriate Fourier coefficients, [109] introduced the differential evolution algorithm by [110, 137].

This has been consistently ranked as one of the best search algorithms for solving global optimization problems in several case studies. This ensures that not only computational speed increases but that the search is not trapped in a local minimum. [166] modified further the optimization approach proposed by [157] for the selection of wavenumbers. [115] go over a method for selecting the ideal set of logarithmic scale equispaced wavenumbers. [113] outlines an improved technique for selecting the wavenumbers that builds on [157] strategy. The optimisation strategy uses a gradient-based search to find the most advantageous coefficients. But this is specific to a given geometry and impacts the computational cost. In order to provide a precise 2D approximation, [109] proposed a novel solution to the non-linear optimisation problem of estimating the appropriate Fourier coefficients. Despite all these efforts there is no single method that guarantees the selection of the best wavenumbers for the underlying problem.

1.3 Thesis Objective and Layout

The present thesis aims to develop a novel 2D DC resistivity modeling algorithm that can handle complex topography and anisotropic conductivity with an arbitrarily tilted symmetry axis. Based on the literature survey, the MFDM is found to be suitable to be employed as the numerical analysis. We have extensively studied the issue of modeling large domain sizes, which is essential in the case of mineral exploration as it needs to be probed deeper. In the energy transition junctures, many scientific and economic societies and institutions have raised concerns about exploring and exploiting more mineral resources to make this transition sustainable and achievable. Therefore, a relook at the classical geophysical methods and their advancement that can aid in mineral investigation is the need of the hour.

The thesis structure is arranged as follows: Chapter 1 introduces the DC resistivity method with a brief history and theory of the DC resistivity method, including fundamental mathematical relations of the DC resistivity equation. The main emphasis of the discussion is on the numerical modeling of DC resistivity data, including the challenges that arise in numerical modeling.

Chapter 2 presents the development of a 2D DC resistivity modeling algorithm based on MFDM. This chapter discusses the basic principles of mimetic methods and the derivation of the numerical scheme using underlying principles. Several benchmarking experiments are included in this study to demonstrate the accuracy of the developed algorithm, including a comparison with published results for a variable topography case

for which an analytical response is unavailable. Lastly, the stability of the developed numerical scheme involving grid distortion is examined.

Chapter 3 presents the development of a novel space-domain algorithm for 2D DC resistivity modeling. It includes motivation for this work by comparing responses simulated using various wavenumber choices to the analytical response of a uniform half-space for long offsets data. Subsequently, the concepts of space domain modeling are discussed, including a new boundary condition at a vertical plane perpendicular to the strike direction that passes through the source position. Finally, several numerical experiments are presented to show the versatility of the developed algorithm for large spacing of current and potential electrodes.

Chapter 4 is based on the insights derived from the developed algorithm concerning the sensitivity of anisotropy to DC resistivity data to anisotropic subsurface. By comparing isotropic, tri-axial, and TTI models, we perform simulations to investigate how different anisotropy elements are scenes by the surface DC resistivity data. Chapter 5 presents the thesis summary, and possible future extensions of the research carried out during this thesis.

Chapter 2

A mimetic finite-difference method for 2D DC resistivity modeling

2.1 Abstract

Nondestructive imaging and monitoring of the earth's subsurface using the geoelectric method require reliable and versatile numerical techniques for solving the governing differential equation. This work presents the first development of an algorithm for modeling two-dimensional direct current resistivity data based on the mimetic finite difference method. The mimetic finite difference method operator encompasses fundamental properties of the original continuum model and differential operator for a robust numerical algorithm. The proposed numerical scheme can simulate the response for an anisotropic model with irregular geometry having discontinuous physical properties. The developed algorithm's accuracy is benchmarked using the analytical responses of dyke models and a two-layer anisotropic model. The simulation result is compared with a published response for the variable topography case. The stability of the developed algorithm involving non-orthogonal grids is analyzed using a three-layer model. Non-orthogonal grids are generated by randomly perturbing the nodal coordinate of orthogonal grids. For these examinations, the maximum error in surface potential remains below 1.1% compared to the orthogonal grid simulation. Hence, the algorithm can simulate an accurate response of complex models such as rugged topography and anisotropic subsurface, and it is very stable concerning grid distortion.

Keywords:Two-dimensional DC modeling, Mimetic finite difference method, Distorted grids, Topography, Robin boundary conditions

2.2 Introduction

The direct current (DC) resistivity method is a classical geophysical technique used to estimate subsurface conductivity. The measurements can be done on the surface or inside the borehole. Since DC measurements have a minimal impact on the environment and are cost-effective, these techniques have been applied to various applications such as mineral exploration [105, 163], underground archaeological studies, groundwater mapping [10, 80] and engineering studies [55]. Generally, the acquired DC data is analyzed using inverse modeling. Apart from ill-posedness, inverse modeling depends heavily on the accuracy and versatility of the forward modeling algorithm. The inverse operator maps the misfit between the observed and simulated data to model space. Consequently, the forward modeling inaccuracy will also be mapped onto the model space by the inversion operator, where the numerical error may get enhanced considerably due to the singular nature of the inverse operator. Therefore, considerable efforts have been directed toward developing forward modeling algorithms that accurately model the response of the subsurface.

The analytical solution of governing equation of the DC problem is only possible for some elementary models. For arbitrary conductivity distribution, numerical methods are utilized. The most commonly applied numerical schemes are the finite difference methods (FDMs), [37, 135], finite element methods (FEMs) [120], surface integral methods [16, 158], and volume integral methods [169]. The FDM works well for a relatively flat topography, while the FEM has no such limitations. However, the FDM is effortlessly extendable to inverse modeling schemes. Generally, the inversion algorithms based on the FEM require distinct meshes for modeling and inversion to optimize the degree of freedom in inversion (e.g., [51]). Consequently, the modeling mesh's nodal field needs to be interpolated at the inversion mesh for gradient/Hessian computation. The Mimetic Finite Difference Method (MFDM) is a suitable alternative to both of these modeling algorithms as it can simulate response for variable topography models and yet does not require different discretization for inverse modeling.

The MFDM schemes are designed by enforcing properties on discrete operators so that the numerical operator possesses properties of the continuum operator. [64] showed that the difference operators obtained using MFDM stand robust for non-orthogonal, unstructured, and nonsmooth meshes. Besides this, MFDM operators satisfy the conservation laws, symmetry properties, and fundamental theorems of the differential and integral operators [128]. Another advantage of MFDM is its suitability to use in trans-dimensional Bayesian inversion workflow. Because in the trans-dimensional Bayesian scheme, the cell nodes' positions are randomly perturbed in space, which is problematic with the FDM [43]. In contrast, the FEM is flexible regarding node position; however, it is more sensitive

to grid refinement than the finite-difference (FD) technique [86]. The trans-dimensional Bayesian scheme requires hundreds of thousands of times to calculate responses of randomly perturbed models (both conductivity and shape of the cells). Consequently, the FEMs' sensitivity of grid refinement may require regenerating the mesh, which is not a trivial step. Therefore, the ability of the MFDM to accommodate the non-orthogonal grids and to be relatively less sensitive to grid refinement makes the MFDM a potential candidate for use in trans-dimensional Bayesian inversion.

MFDM schemes have been applied to various geophysical problems, including seismic [34, 124], electromagnetic [155], gravity [71], and shear rupture modeling [118]. For electromagnetic data modeling, [70], observed that the MFDM is more suitable than the traditional finite element (FE) or finite volume methods. Therefore, MFDM has a huge scope of implementation to DC resisitivity modeling, as the DC resistivity technique is used extensively in investigating near-surface complexities. For example, the critical zone study has emerged as a new area where more near-surface geophysical methods are being applied for applications such as imaging the tree root system [111], soil moisture studies, and so on [72]. Many investigation sites of critical zone study have variable topography. The irregular topography and the near-surface processes may lead to anisotropic subsurface, and anisotropy can be used as a proxy for understanding such processes. Since a lot of data, especially in the research domain, is acquired along straight lines, 2D data analysis is done routinely. Even if 3D data is observed, it is reasonable to perform a 2D inversion. The 2D inverted models can also be used for creating an initial model for 3D inversion.Hence, developing a robust and versatile 2D DC modeling algorithm is still an active research area.

In this study, we develop a 2D DC resistivity modeling algorithm employing an MFDM scheme that can handle irregular topography and anisotropic subsurface. The paper's outline is as follows: In Section 2, the basic theory of DC resistivity modeling and a detailed discussion of the MFDM scheme suitable for the DC resistivity problem is discussed. Subsequently in section 3, the accuracy of the developed algorithm is verified by comparing the numerical solutions against the analytical results. Finally, the stability of the developed algorithm involving non-orthogonal grids is analyzed using a three-layer model. The cells where the angle between cell arms is either less than 25 degrees or more than 155 degrees, are denoted as highly distorted. The numerical tests are conducted by varying extents of grid distortion. The highly distorted cells could be as high as 10% of the total cells. For these tests, the error bar remains below 1.1%, thereby confirming the algorithm's stability on distorted, non-orthogonal grids. Section 4 highlights the conclusions derived from this

study. This study presents the first implementation of MFDM to perform the DC resistivity modeling.

2.3 DC Resistivity Modeling

The DC resistivity modeling problem in 3D is expressed as,

$$\nabla_{3D} \cdot [T_{3D}(x, y, z)\nabla_{3D} u(x, y, z)] = -I\delta(x - x_\circ)\delta(y - y_\circ)\delta(z - z_\circ), \tag{2.1}$$

on V, where V is the computational domain. $\nabla_{3D}\cdot$ and ∇_{3D} are the divergence and gradient operators, respectively in the 3D space. $T_{3D}(x, y, z)$ is the conductivity tensor. The right hand side term denotes the source term, where I is the current intensity, $\delta()$ is the Dirac delta function, and $(x_\circ, y_\circ, z_\circ)$ represents the coordinates of the source. The aim is to solve Eq. (2.1) for the unknown potential $u(x, y, z)$ under the appropriate boundary conditions for a given conductivity distribution. The general form of boundary conditions is referred to as Robin boundary condition [52] and it can be expressed as,

$$\lambda(\vec{n}.T_{3D}\nabla_{3D} u) + \eta u = \mu \text{ on the boundary } \partial V, \tag{2.2}$$

where λ, η and μ are the coefficients which determine different types of boundary conditions, and $\vec{n}$ represents the normal component. For the DC problem, the homogeneous Neumann boundary condition is applicable on the surface of the domain, i.e. ∂V_s, which can be achieved by setting the value of the coefficients in Eq. (2.2) as,

$$\lambda = 1, \eta = 0 \text{ and } \mu = 0, \tag{2.3}$$

to ensure that the normal component of the potential is zero. Consequently, the electric field component perpendicular to the terrain is zero at the surface; hence, the current at the surface flows along the topography. On the side boundaries, i.e. ∂V_∞, the Robin (mixed) boundary conditions given by [36], are applied, which is equivalent to the case,

$$\lambda = 1, \eta = \frac{cos\theta}{r} \text{ and } \mu = 0, \tag{2.4}$$

where r is the distance from the source location to the measuring location, and θ is the angle subtended between the radial vector from the source position to the measuring position and the normal at the measuring position.

For anisotropic medium, the conductivity tensor, $T_{3D}(x,y,z)$ is expressed as

$$T_{3D} = \begin{bmatrix} \sigma_{xx} & \sigma_{xy} & \sigma_{xz} \\ \sigma_{yx} & \sigma_{yy} & \sigma_{yz} \\ \sigma_{zx} & \sigma_{zy} & \sigma_{zz} \end{bmatrix}.$$

Let us assume a model where the axis of anisotropy and the coordinate axis in the y-direction coincide. Consequently, the current density in the y-direction gets decoupled from the electric field in the x- and z-direction. For example, DC data acquired along a profile perpendicular to the hinge (here, the hinge is in the y-direction) of an anticline would exhibit such anisotropy. Under this condition, T_{3D} transforms to,

$$\hat{T}_{3D} = \begin{bmatrix} \sigma_{xx} & 0 & \sigma_{xz} \\ 0 & \sigma_{yy} & 0 \\ \sigma_{zx} & 0 & \sigma_{zz} \end{bmatrix}.$$

For a two-dimensional model, the conductivity in the strike direction does not change. Therefore, σ_{yy} will be invariant in the y-direction considering the strike along the y-direction. Under these conditions, the solution for Eq. (2.1) can be simplified considerably by taking the Fourier transform with respect to the y-variable. It is also convenient to work with primary/secondary decomposition formulation [91] to address the problem of source singularity. Consequently, the governing equation for the 2D problem using primary/secondary decomposition can be expressed in the wavenumber domain as,

$$\begin{aligned} \nabla \cdot [T_{2D}(x,z)\, \nabla \tilde{u_a}(x,k,z)] - k^2\, \sigma_{yy}(x,z)\, \tilde{u_a}(x,k,z) = \\ -\nabla \cdot [T_{2Da}(x,z)\, \nabla \tilde{u_n}(x,k,z)] + k^2\, \sigma_{yya}(x,z)\, \tilde{u_n}(x,k,z), \end{aligned} \tag{2.5}$$

where σ_{yy} and σ_{yya} are the conductivity values in the y-direction for the model and the anomalous body, respectively. k represents the wavenumber, $\nabla\cdot$ and ∇ denotes the 2D divergence and gradient operator respectively. $\tilde{u_n}(x,k,z)$ and $\tilde{u_a}(x,k,z)$ are the potentials in the Fourier domain for the primary field and the anomalous field, respectively. $T_{2D}(x,z)$ and $T_{2Da}(x,z)$ are the conductivity tensors of the medium and the anomalous block, respectively. The conductivity of the anomalous body is simply given by the difference between the conductivity of the model and the primary/background medium. Here, T_{3D} transforms to $T_{2D}(x,z)$, which is given by,

$$T_{2D} = \begin{bmatrix} \sigma_{xx} & \sigma_{xz} \\ \sigma_{zx} & \sigma_{zz} \end{bmatrix}.$$

The construction of right hand side in the Eq. 2.5 requires a known primary potential, $\tilde{u_n}(x,k,z)$. Therefore, a simple background medium is used for the primary potential computation for which analytical expressions are available. The equation is then numerically solved for the unknown potential $\tilde{u_a}(x,k,z)$. The total potential is finally computed by adding the primary and the anomalous potential [30].

In the wavenumber domain, the Robin boundary conditions given in Eq. (2.2) can be expressed as,

$$\tilde{\lambda}(\vec{n}.T_{2D}\nabla\tilde{u_a}) + \tilde{\eta}\,\tilde{u_a} = \tilde{\mu} \text{ on the boundary } \partial V. \tag{2.6}$$

Eq. (2.5) is solved with the boundary condition given in Eq. (2.6), where for the top surface, ∂V_s,

$$\tilde{\lambda} = 1, \tilde{\eta} = 0, \text{ and } \tilde{\mu} = 0. \tag{2.7}$$

and for distant boundaries, i.e ∂V_∞,

$$\tilde{\lambda} = 1, \tilde{\eta} = \frac{k\,K_1(k\,r)}{K_0(k\,r)}\,cos\theta, \text{ and } \tilde{\mu} = 0, \tag{2.8}$$

where K_1 and K_0 are the modified Bessel functions of second kind, order one and zero, respectively.

Now, the application to the topography cases is emphasized further. The term $\tilde{u_n}(x,k,z)$ in the Eq. (2.5) is the background potential field of the model. This is easily available for half-space models as the analytical solution exists. But in the case of topography, there is no general analytical expression to compute the background field. Hence, the term $\tilde{u_n}(x,k,z)$ is unknown. This becomes a constraint to simulate the response for a model with topography. Researchers have adopted various methods [40, 120] to simulate the response for a variable topography. [112] proposed a scheme where primary potential due to halfspace is used, and only the surface boundary condition needs to be modified. The modified boundary condition in 3D is expressed by taking the following values of the constants

$$\lambda = 1, \eta = 0, \text{ and } \mu = -\frac{I}{2\pi}\frac{(x-x_0).\hat{n}}{r^3}, \tag{2.9}$$

where x_0 is the source location, x is a point on the profile, r is the radial distance from the source point to the measuring location, and $\hat{n}$ is the the unit normal to the radial vector from source to measuring point. Therefore, in the wave-number domain, the surface boundary condition for topography case can be expressed as

$$\tilde{\lambda} = 1, \tilde{\eta} = 0, \text{ and } \tilde{\mu} = -\frac{I\,k\,K_1(k\,r)\,cos\theta}{2\,\pi}. \tag{2.10}$$

Consequently, the 2D DC resistivity modeling for an anisotropic and variable topography model can be achieved by solving Eq. (2.5) under boundary conditions given in Eq. (2.8) and Eq. (2.10). Various algorithms have been developed so far to deal with the complicated cases of DC modeling. This novel approach first presented as support operators method by [128] and [129], is also known as the MFDM approach.

2.3.1 Mimetic Methods

We try to model various physical processes that reproduce natural phenomena as accurately as possible in computational sciences. There are multiple complexities such as non-linearity in the processes, discontinuity of the coefficients arising in the physical system, discontinuity in the solution, preservation of the conservation laws, and symmetry properties of the process that need to be addressed. In addition, complex geometries need to be incorporated into the modeling to simulate real-world problems. There are numerous techniques to handle simple structures. However, complex geometries, topographies, and embedded anomalous bodies are not so easy to handle.

Many numerical modeling techniques have been widely implemented and published in scientific literature. FDMs are relatively simple to implement. However, it is challenging to accommodate non-orthogonal grids via FDMs. So, implementing topography is non-trivial. A special class of FDMs called MFDM, has a remarkable ability to address these requirements. Hence, we work with MFDM and develop a C++ code to model the DC resistivity problem. There have been different names in the literature for MFDM like the support-operator method, reference operator, [64, 65, 101] etc. These methods have been translated from non-English literature and were given names to match the exact translation closely. The governing differential equation contains the continuous differential operators. The aim is to design discrete differential operators that are accurate and preserve the properties of original governing equations. To begin with the process of discretization, it is important to identify the properties of the governing equation. It has to be emphasized that the standard FDMs turn out to be the special cases of MFDM on orthogonal grids. The MFDM can be used in any coordinate system as they work on the coordinate invariant operators like gradient, divergence, and curl.

The objective is to solve the Eq. (2.5) using the boundary conditions given in Eq. (2.8) and Eq. (2.10). The terms in the left hand side and right hand side that contain k^2 are just scalar multiplications of wavenumber, conductivity values and the potentials, which is trivial to implement. Therefore, the emphasis is to design differential operators for the implementation of the $\nabla \cdot [T_{2D}(x,z)\nabla \tilde{u_a}(x,k,z)]$ and $-\nabla \cdot [T_{2Da}(x,z)\nabla \tilde{u_n}(x,k,z)]$ in the main equation, using the MFDMs. This study follows the mimetic approach given by [128].

In order to construct the above differential operators, we pose a simplified equation that contains the same differential operator as,

$$-\nabla \cdot T_{2D}(x,z)\,\nabla u = f,\ (x,z) \in V, \tag{2.11}$$

where V is a two-dimensional region. Here, $\nabla\cdot$ is the continuous 2D divergence operator, ∇ is the continuous 2D gradient operator, $T_{2D}(x,z)$ is a symmetric positive-definite (conductivity) tensor, $u(x,z)$ is the scalar potential and f is the source/sink function.

Consider the space of continuum scalar functions CS and continuum vector functions CV. Natural operators are defined taking into account Eq. (2.11). Let L_1, L_2 and L_3 be three different operators, described as,

$$\begin{aligned} L_1 &: CS \rightarrow CV, \\ \text{defined as } L_1(u) &= \vec{A}, \end{aligned} \tag{2.12}$$

where L_1 mimics the gradient operator and L_2 is another operator such that

$$\begin{aligned} L_2 &: CV \rightarrow CV, \\ \text{defined as } L_2(\vec{A}) &= -T_{2D}\,\vec{A}, \end{aligned} \tag{2.13}$$

where L_2 denotes the operation of second rank tensor (dyadic material parameters), T_{2D}, on the $\vec{A}$, giving back a vector entity to be acted upon by the divergence operator. It transforms the electric field to the current density. This physical process is expressed mathematically by the L_2 operator. The operator L_3, that mimics the divergence operator, follows as,

$$\begin{aligned} L_3 &: CV \rightarrow CS, \\ \text{defined as } L_3(-T_{2D}\,\vec{A}) &= f. \end{aligned} \tag{2.14}$$

The composition operator $L = L_3\,o\,L_2\,o\,L_1$, is framed as,

$$\begin{aligned} L &: CS \rightarrow CS, \\ L(u) &= L_3 o L_2 o L_1(u) = f. \end{aligned} \tag{2.15}$$

The boundary conditions to be imposed on the governing equations are the Robin boundary conditions. However, the operators involved in the boundary conditions are identical as defined above. The properties of these continuum operators are briefly discussed here.

For more details, reader can refer to [60, 62, 66, 68] and citations within. These properties form the basis of the mimetic formulation. The differential operators that are derived, are constructed in such a way that they inherit the same properties as that of continuum operators. The most important formulating property in this class of equations is the adjointness of the continuum operators.

2.3.2 Properties of the operators

Let us consider the Robin boundary conditions along with the Eq. (2.11)

$$\lambda(\vec{n}.T_{2D}\nabla u) + \eta\, u = \mu. \tag{2.16}$$

Along with this boundary conditions, the operator L can be given by,

$$\begin{aligned} L &: CS \rightarrow CS, \\ L\,u &= -\nabla \cdot T_{2D}\nabla u,\ (x,z) \in V, \\ L\,u &= T_{2D}\nabla u.\vec{n} + \eta u,\ (x,z) \in \partial V. \end{aligned} \tag{2.17}$$

Let us consider the operator R given by

$$\begin{aligned} R &= f,\ (x,z) \in V, \\ R &= \mu,\ \ (x,z) \in \partial V. \end{aligned} \tag{2.18}$$

The formulation can be finally given as, $L\,u = R$. The properties of the operator L are described briefly. It is important to describe the properties of the continuum operator L since these properties form the basis of MFDMs. At this stage, it would be necessary to state that these continuum properties are imbibed into the construction scheme of FD operators, so that they inherit the characteristics naturally and serve the general purpose that is desired from the MFDMs.
The inner product for the scalar potentials u and v is defined on the scalar space CS by,

$$\langle\, u, v \,\rangle_{CS} = \int_V u\, v\, dV + \oint_{\partial V} u\, v\, dS, \tag{2.19}$$

where dV and dS represent the area and length elements respectively, over which the integration is carried out. From the definition of the operators given in Eq. (2.17) and Eq. (2.18), and the inner product in Eq. (2.19), it can be proved that the operator L possess the

following three properties [29, 127].

$$\begin{aligned} \langle L\,v\,,\,u\rangle_{CS} &= \langle v\,,\,L\,u\rangle_{CS}, \\ \langle L\,v\,,\,v\rangle_{CS} &\geq 0, \\ \langle L\,v\,,\,v\rangle_{CS} &> 0,\ if\ \eta > 0. \end{aligned} \tag{2.20}$$

Moreover, using the composition form of the operators, i.e $L = L_1 o L_2 o L_3$, it can be proved that the operator L_1 is adjoint to the operator L_3, i.e

$$L_1 = L_3^*. \tag{2.21}$$

It was necessary to introduce the spaces of inner products, to highlight the adjointness property. The importance of mimetic methods lies in the fact that it takes into account the continuum properties of the problem. The conductivity tensor T_{2D} is allowed to be discontinuous and non-diagonal. The method works perfectly fine with the non-smooth computational grids.

In order to implement DC method numerically, the continuum operators that are present in the Eq. (2.11) need to be discretized. The process of discretization is described in the next subsection, which brings out the salient features of this method. The discretization is imposed on the operators in such a way that these properties are naturally inherited in the process 1) Conservation laws are preserved. 2) Discontinuous properties can be taken into account across interfaces. 3) Preserves the symmetry property. Looking at the Eq. (2.11), two different operators are taken into account i.e. 1) $\nabla\cdot$ and 2) $T_{2D}\nabla$. These are the continuous 2D differential operators present in the governing equation. The aim is to discretize these two operators and come up with a FD scheme, which can be used on non-orthogonal grids. All the steps involved are mentioned concisely.

To begin the discretization procedure, one must choose the scheme for defining vector and scalar entities on the defined grid. [127] discuss two schemes for solving elliptic equations using MFDM. In the first scheme, scalar quantities are discretized at the cell nodes, and vector functions are defined at cell centers; in the second, scalar quantities are discretized at the cell centers, and vector functions are defined at nodes. They presented a detailed comparison of both schemes and observed that the second scheme is more suitable for implementing boundary conditions on corner cells in the case of curvilinear mesh. Therefore, the scheme of cell-valued discretization of scalar functions and the nodal discretization of vector functions is implemented. To keep the notation consistent, a subscript $'d'$ is used to denote the discrete entities. Fig. 2.1 shows a quadrilateral cell (i, j) with the potential $u_{d(i,j)}$ at the center of the cell. The vector quantity $A_{\vec{d(i,j)}}$ is placed

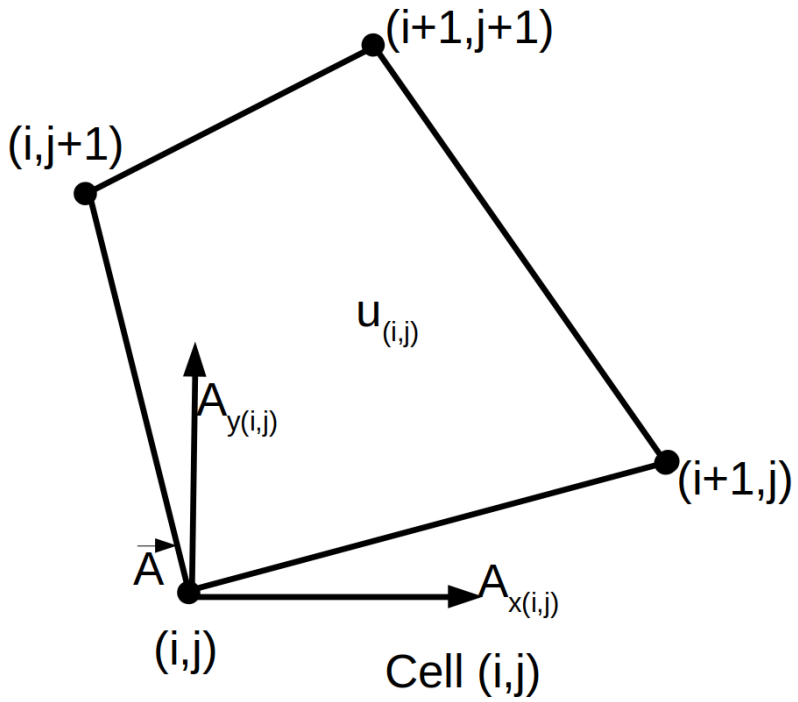

Fig. 2.1 Representation of the cell (i,j), showing the scalar potential at the cell center and the vector quantity at the cell nodes for a quadrilateral cell

at the nodes of the cell (i, j). The two projections along the coordinate axes $A_{dx(i,j)}$ and $A_{dz(i,j)}$ are shown to depict the components of the vector. The conductivity tensor T_{2d} is defined at the cell centers and coincide with the location of potential scalars $u_{d(i,j)}$. For any cell (i, j), the discretized conductivity tensor can be given as

$$T_{2d(i,j)} = \begin{bmatrix} \sigma_{xx}(i,j) & \sigma_{xz}(i,j) \\ \sigma_{zx}(i,j) & \sigma_{zz}(i,j) \end{bmatrix}. \tag{2.22}$$

The operators L_1, L_2 and L_3 used for the continuum case, need to be discretized. The approach is as follows: 1) First of all, the operator L_3 is taken and the coordinate invariant definition is followed to construct its discrete analog (L_{3d}). This can also be termed as the primary or the main operator that is derived from the definition itself; 2) Since the conductivity tensor is defined at the cell centers, it is easy to derive the operation of a tensor on discrete vector components; 3) The last step is to design the operator L_{1d}. It is important to mention here that the adjointness property is already highlighted in the Eq. (2.21). The same property has to be imposed on the discrete analogs. Hence, it is forced

that the adjointness property is also inherited by the discrete operators, using the relation,

$$L_{1d} = L_{3d}^{*}. \tag{2.23}$$

Using the coordinate invariant definition of the divergence operator, it can be written,

$$L_3(\vec{A}) = \lim_{V \to 0} \frac{\oint_{\partial V} (\vec{A}.\vec{n}) dS}{V}. \tag{2.24}$$

The aim is to express the above definition in the discrete form. It can be done by considering a cell element, $\Omega_{(i,j)}$, and the boundary of the cell as $\partial\Omega$. The continuum integral in the Eq. (2.24) can then be translated to a cell integral for a discrete case by,

$$\oint_{\partial\Omega} (\vec{A}.\vec{n}) dS = \int_1 (\vec{A}.\vec{n}) dS + \int_2 (\vec{A}.\vec{n}) dS + \int_3 (\vec{A}.\vec{n}) dS + \int_4 (\vec{A}.\vec{n}) dS, \tag{2.25}$$

where the subscripts, $1, 2, \cdots, 4$ denote the line integrals on the four different sides of the cell. Finally, this will give the approximation for L_{3d}. It is trivial to obtain the operation of L_{2d} on the discretized vector components $A_{dx(i,j)}$ and $A_{dy(i,j)}$. Following this, the Eq. (2.23), can be used to obtain the operator L_{1d} that satisfy Eq. (2.23) using algebraic manipulations.

2.3.3 Implementation in discrete space

This section briefly describes the code development and implementation strategy for the MFDM. The scheme works on a nine-point stencil. For the sake of completeness, it is necessary to define inner products on the space of discrete scalar potentials, as well as on the space of discrete vectors. Let DS be the space of discrete scalar functions and DV be the space of discrete vector functions. Then the inner products for DS are defined as,

$$\begin{aligned}(u_d, v_d)_{DS} = \sum_{i,j=1}^{M-1,N-1} u_{d(i,j)}\, v_{d(i,j)}\, \Omega_{i,j} + \sum_{i=1}^{M-1} u_{d(i,0)}\, v_{d(i,0)}\, lx_{i,1} + \\ \sum_{j=1}^{N-1} u_{d(M,j)}\, v_{d(M,j)}\, lz_{M,j} + \sum_{i=1}^{M-1} u_{d(i,N)}\, v_{d(i,N)}\, lx_{i,N} + \\ \sum_{j=1}^{N-1} u_{d(0,j)}\, v_{d(0,j)}\, lz_{1,j}.\end{aligned} \tag{2.26}$$

For space DV, it can be written

$$(\vec{A}_d, \vec{B}_d)_{DV} = \sum_{i,j=1}^{M,N} (AX_{d(i,j)}\, BX_{d(i,j)} + AZ_{d(i,j)}\, BZ_{d(i,j)})\, NV_{i,j}, \tag{2.27}$$

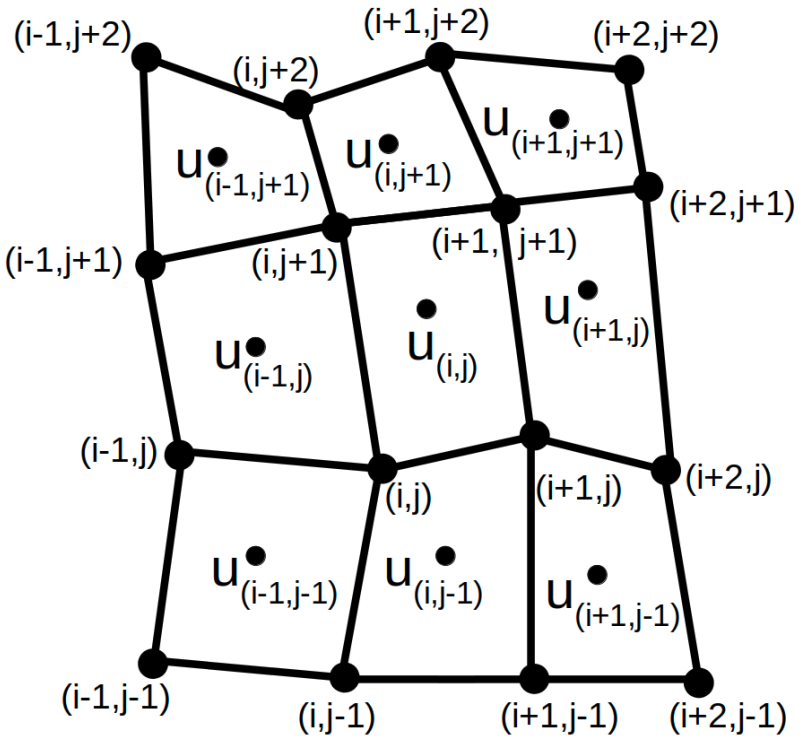

Fig. 2.2 Nine-point stencil scheme used in the MFDM

where $NV_{i,j}$ is the nodal volume for the cell (i, j). For a node, it is defined as the average area/volume of the four cells that share that particular node. For the cell (i, j), the equation to be written has contributions from the nine cells shown in Fig. 2.2. The unknown scalar potentials are defined at the cell centers and the vector components are on the cell nodes. On the boundary, fictitious cells are introduced, which makes writing the equations easier for a computer code. These fictitious cells, naturally take care of the potential field at the boundary, by placing them at the center of the edges. Finally by using discrete form of Eq. (2.25) as given in Eq. (2.26) and forming the gradient operator using adjoint relationship (Eq. (2.23)), one can formulate a linear set of equations as given in Appendix A. After framing the linear system of equations, the k^2 terms present in the Eq. (2.5) are then added to the diagonal of the resulting system. This completes the formulation of the linear system to be solved. Since the Robin boundary conditions are used, the system is structurally symmetric but not symmetric entry wise. Hence, preconditioned

BiCGSTAB iterative solver is used to solve the obtained system. Finally, inverse Fourier transformation is performed to transform the solution into the space domain. The five-point formulation [109] for converting the potential into the space domain is adopted as shown in Table 2.1. However, for large electrode spacing and complex models, one needs to use more wavenumber values for accurate computations. Therefore, the maximum electrode spacing in our numerical experiments is restricted to 200 m.

Table 2.1 Wavenumbers and corresponding weights used from [**?**]

Wavenumbers	**Weights**
$k1 = 0.0031677$	$g1 = 0.0067253$
$k2 = 0.0301330$	$g2 = 0.0314373$
$k3 = 0.1285886$	$g3 = 0.1090454$
$k4 = 0.4599185$	$g4 = 0.3609340$
$k5 = 1.5842125$	$g5 = 1.3039204$

2.4 Numerical Experiments

The numerical experiments carried out utilising the created algorithm are presented in this section. The following tests are performed to show how accurate and adaptable the code is. An isotropic dyke model is simulated under two different conditions: low contrast and high contrast. Both these tests show the accuracy of our code and its applicability to simulate high contrast models. An anisotropic model is simulated to show the applicability of the developed algorithm to anisotropic subsurface. The performance of the code is tested on a topographic model that shows the strength of the code for non-orthogonal grids. Finally, a stability test is performed using a layered model to illustrate the algorithm's robustness involving non-orthogonal grids. All the tests mentioned here are done for fine as well as coarse grids. Since, the grid spacing is nonuniform, these are expressed as $[x_{min}, x_{max}] \times [z_{min}, z_{max}]$, where x_{min} and x_{max} denote the minimum and maximum grid spacing in x-direction respectively, and z_{min} and z_{max} are the minimum and maximum grid spacing in the z-direction respectively. The fine grid spacing is doubled in both x and z-directions to construct coarse grid discretization for all the experiments. Nonuniform grids required to be implemented to facilitate arbitrary coarsening and refining of the grids to discretize the model optimally.

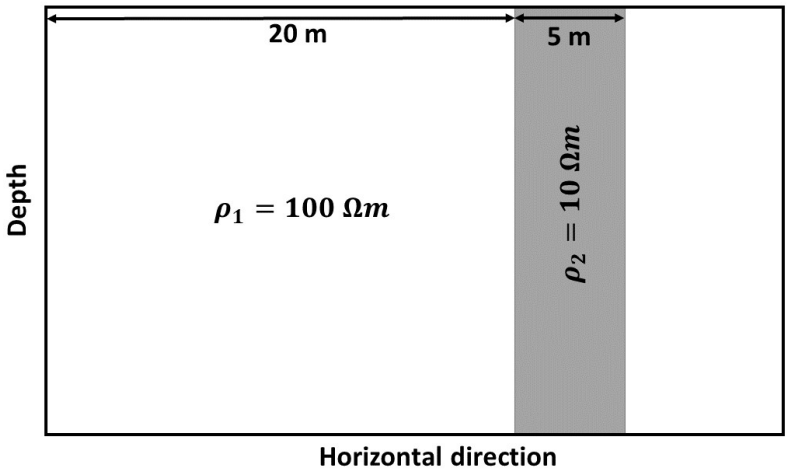

Fig. 2.3 Schematic diagram of a vertical dyke model. The resistivity of the dyke is $\rho_2 = 10\,\Omega\,m$ and the resistivity of the half space is $\rho_1 = 100\,\Omega\,m$. The dyke has a width of 5 m and is placed at a distance of 20 m from the origin

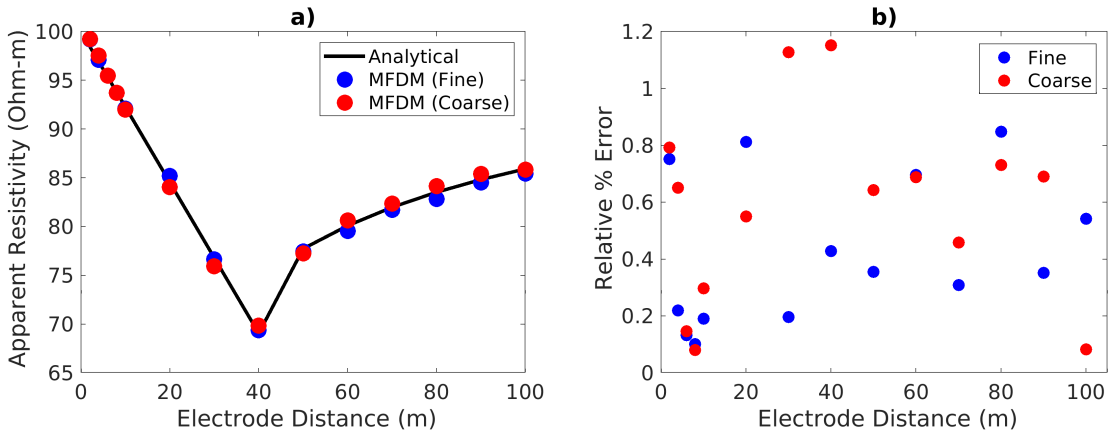

Fig. 2.4 Dyke model experiment results (a) apparent resistivity obtained from the MFDM for fine and coarse model, and the analytical solution and (b) plot shows the relative % error between the simulated responses and the analytical solution

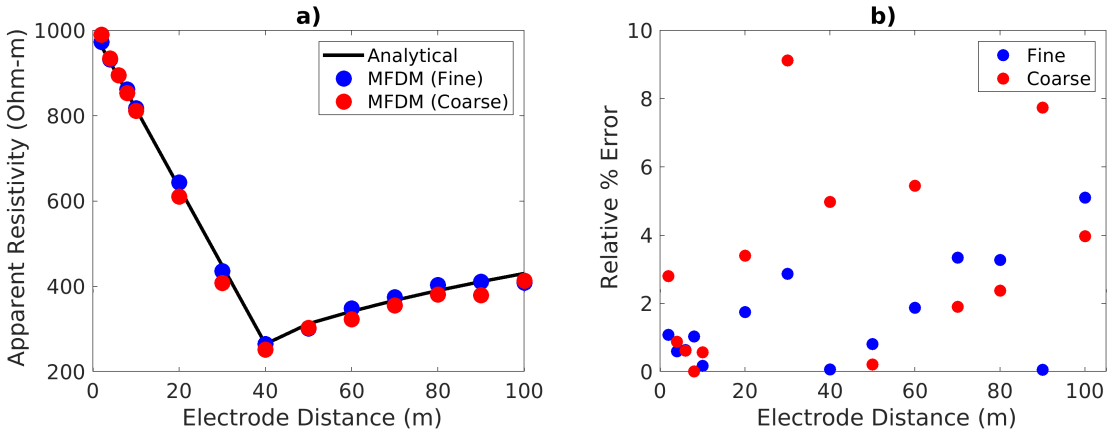

Fig. 2.5 High-contrast dyke experiment results (a) apparent resistivity obtained from the MFDM and the analytical solution for the high conductivity contrast dyke model and (b) shows the relative % misfit between the responses from MFDM and analytical solution

2.4.1 Dyke Model

To verify the accuracy of the developed algorithm, the first modeling experiment is carried out on a dyke model. This model is chosen as the analytical solution is available for dyke model [143]. The dyke model consists of a background with $\rho_1 = 100\ \Omega m$ in which a perfectly vertical dyke with $\rho_2 = 10\,\Omega m$ is present. The width of the dyke is 5 m, and is located at 20 m from the origin as shown in Fig. 2.3. A pole-pole array experiment is performed on this model. The test is carried out with fine and coarse grids. The grid parameters for the fine case are given by $([0.5,5] \times [0.5,5])$, and the coarse grid parameters are kept as $([1,10] \times [1,10])$. Apparent resistivity estimated from the simulated response and using the analytical formulation along a 100 m profile is shown in Fig. 2.4a. The relative misfit in percentage is computed between simulated and analytical response, the misfit plot is shown in Fig. 2.4b. The maximum error for fine model is less than 1%, whereas for the coarse model the error lies below 1.2%, indicating the accuracy of the modeled response. To further test the strength and accuracy of the algorithm, a test is performed for a high conductivity contrast dyke model. A similar model as shown in Fig. 2.3, is considered, except the resistivity of the half-space is increased by a factor of 10. Hence, $\rho_1 = 1000\,\Omega\,m$ and $\rho_2 = 10\,\Omega\,m$. The grid size is kept the same for fine and coarse case as that of low contrast case. The apparent resistivity curves for the high conductivity contrast model and the percentage error plots are shown in Fig 2.5a and Fig. 2.5b, respectively. The maximum misfit for the high contrast fine model is around 5%, which is within the acceptable numerical error limit. For coarse grid discretization, the maximum misfit is around twice the fine grid case. From both these experiments, it is

also observed that the impact of grid coarsening is more around dyke. That is because the dyke is very thin (5 m only), and fine horizontal discretization around dyke is required for accurate computation.

2.4.2 Anisotropy

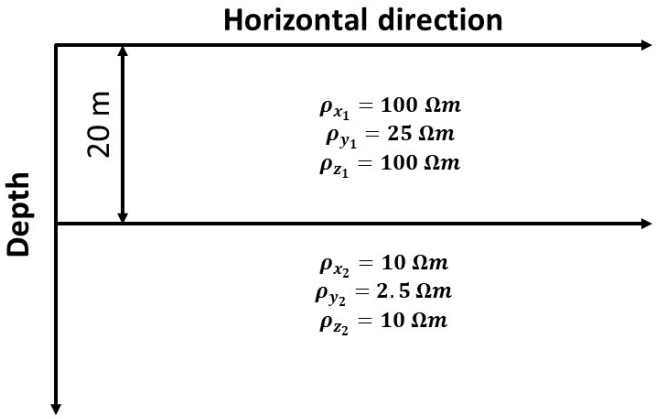

Fig. 2.6 Schematic diagram representing the anisotropic model

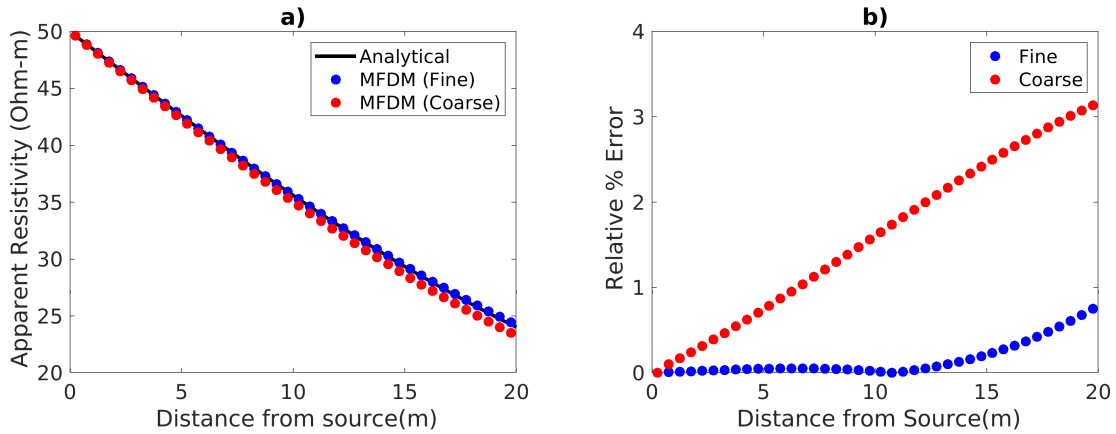

Fig. 2.7 Anisotropic-model experiment (a) apparent resistivity curves obtained from MFDM and analytical solution for the pole-pole configuration and (b) the misfit plot

For anisotropic case, a two-layered model as shown in the Fig. 2.6 is considered. In case of a tri-axial anisotropy, each layer can be explained by three resistivity values. The resistivity of the layers are, $\rho_{x1} = 100\,\Omega\,m$, $\rho_{y1} = 25\,\Omega\,m$, $\rho_{z1} = 100\,\Omega\,m$. and $\rho_{x2} = 10\,\Omega\,m$, $\rho_{y2} = 2.5\,\Omega\,m$, $\rho_{z2} = 10\,\Omega\,m$, where the subscripts 1 and 2 denote the first layer and the second layer respectively; the subscripts x, y and z represents the resistivities in

the direction of co-ordinate axes, x, y and z respectively; where y is the strike direction. The thickness of the first layer is 20 m and the thickness of the second layer is assumed to be infinite. The model is simulated for fine ($[0.5] \times [1,2]$) and coarse grids ($[1] \times [2,4]$).The apparent resistivity curves are calculated using pole-pole array for this model, and the percent relative error is calculated by comparing it with the analytical solution [150]. The apparent resistivity curves for fine and coarse grids and the misfit plots are shown in Fig. 2.7. The maximum error is below 0.8% for the fine grids. The error shows an increasing trend for both the fine as well as coarse grids as the offset increases, which is generally expected for anisotropic cases [159]. The grid coarsening increases the misfit considerably in this case. Through tests it is observed that, the error arises due to the grid coarsening in the z-direction. Generally the choice of optimum grids is considered based on array configuration, the desired resolution and the available computational resources. However, this point is not explored further in this study as it requires inverse modeling. In nutshell, this experiment illustrates the strength of the MFDM scheme to simulate the response for anisotropic models.

2.4.3 Topography

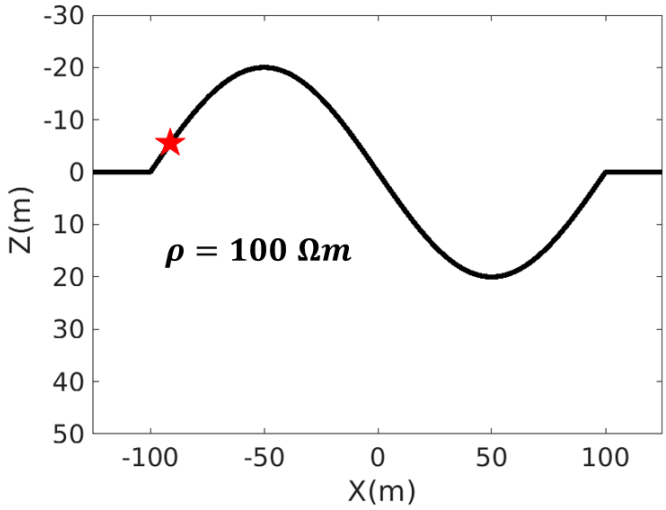

Fig. 2.8 Mountain-valley topography model. The red star indicates the source location at -90 m. Potential electrodes are placed on the surface, starting from -80 m, with a spacing of 10 m between consecutive electrodes

In this experiment a mountain-valley topography model is considered as shown in Fig. 2.8. The model is simulated for fine ($[0.5,5] \times [0.5,5.6]$) and coarse grids ($[1,10] \times [1,10]$). This test is done to check the performance of the MFDM on the topographic models,

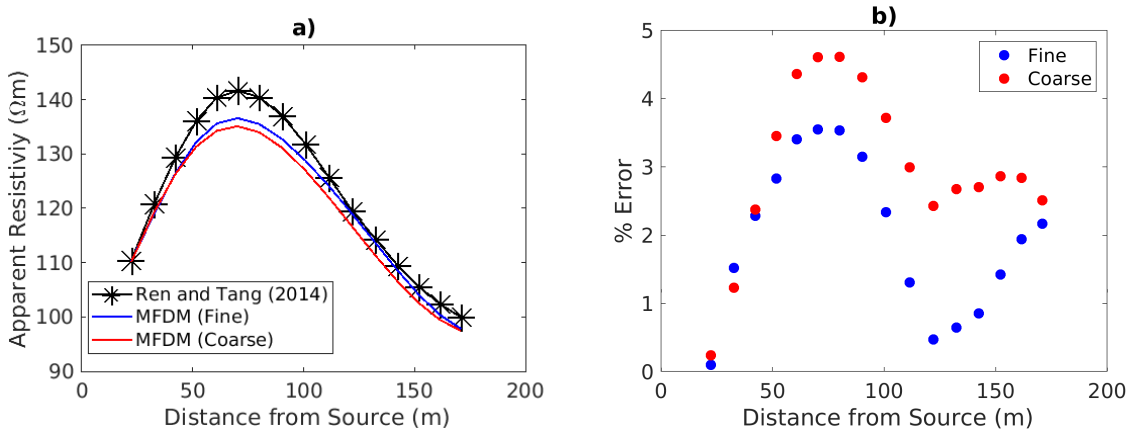

Fig. 2.9 Topography model simulation (a) the apparent resistivity plot obtained for the mountain-valley model using the MFDM approach and the discretized solution from the [117]. (b) misfit between the apparent resistivity values

implementing the secondary potential approach by [112]. The model has a sinusoidal topography, with an amplitude of 20 meters. The background resistivity of the model is taken as 100 $\Omega\,m$. A sinusoidal function of wavelength 200 m is considered to simulate this topography. The source is placed at -90 m on the surface of topography. From the source location, a total of 17 electrodes are placed and the spacing is kept as 10 meters between consecutive electrodes. The potential values are computed at the potential electrode positions and the apparent resistivity is calculated using pole-pole configuration.

There is no analytical solution available to verify the results. Hence the apparent resistivity results published by [117], are discretized and interpolated at the modelled response positions to compare with the solutions. The plot for the apparent resistivity obtained from the MFDM approach for fine and coarse models and [117], are shown in the Fig. 2.9a, and the misfit is illustrated in Fig. 2.9b. It is observed that the maximum relative percent error is around 3.5% for the fine case and 4.7% for the coarse case. The misfit around the top of the mountain is relatively more than near the bottom of the valley region. It needs to emphasis that here the benchmarking is done using numerically simulated results, which itself contains some amount of error. Furthermore, the error has contributions from three sources, 1) the discretization error of the apparent resistivity plot, 2) interpolation error, and 3) the misfit between two responses. However, the numerical error is within the acceptable level of numerical error as it is less than the typical noise present in the observed data. The results of all these experiments demonstrate the accuracy and robustness of the developed algorithm for various models. Modeling complex shaped body or very rugged topography requires the cells to deviate considerably from the orthogonal grids. In the

next subsection, the stability test for the developed algorithm with respect to distorted grids is presented.

2.4.4 Stability analysis

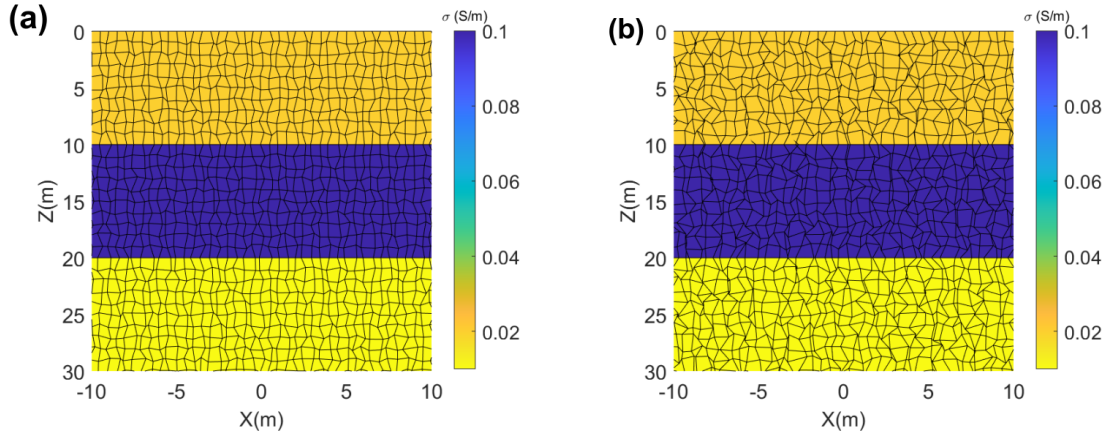

Fig. 2.10 Three-layer model overlaid with grid structure used for stability test. This shows the magnified view for better visualization, (a) low levels of distortion and (b) highly distorted random grids

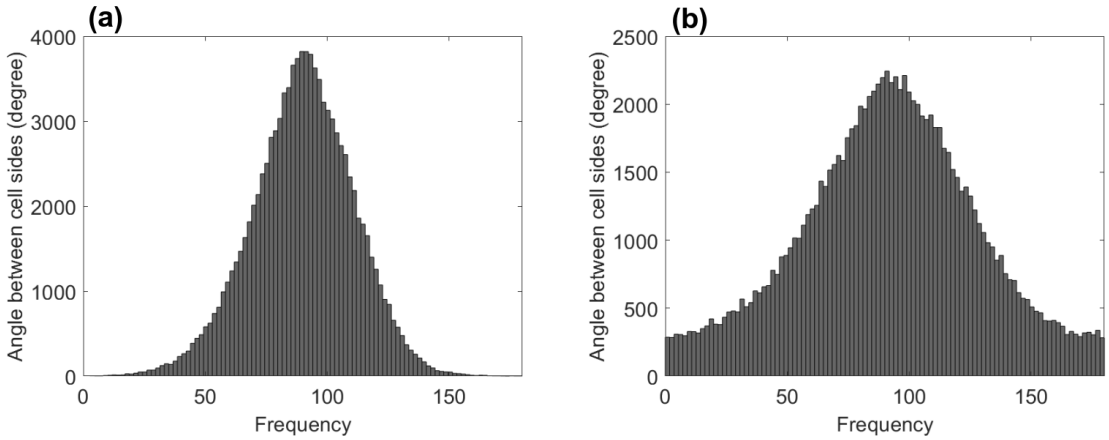

Fig. 2.11 Histogram analysis for the vertex angles for (a) low levels of distorted grids and (b) highly distorted grids

The ability of a modeling algorithm to simulate the response of complex geometrical shapes is crucial for practical applications across a whole spectrum of geological scenarios. To accommodate the complex structures, the discretization needs to be adapted to make the cell side conformal to the interface of physical property contrasts. Therefore, the sharply varying interface necessitates a considerable distortion of cells. Here distortion

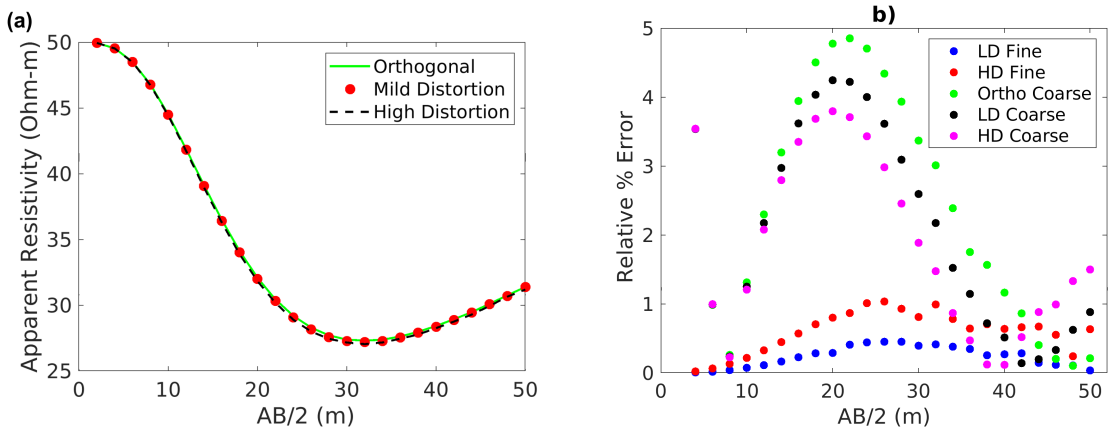

Fig. 2.12 Stability test results (a) apparent resistivity plots for three different cases of fine grids 1) solid green line corresponds to the orthogonal grids, 2) red dots corresponds to mild or low levels of distortion, 3) dashed line corresponds to the high levels of distortion and (b) the relative % error with orthogonal fine grid response 1) blue dot corresponds to LD (low distortion) fine grids, 2) red dot corresponds to HD (high distortion) fine grids, 3) green dot corresponds to Ortho (orthogonal) coarse grids, 4) black dot corresponds to LD (low distortion) coarse grids, 5) magenta dot corresponds to HD (high distortion) coarse grids.

means the degree of deviation of a cell from a rectangle shape. The angles between adjacent cell sides that meet at a vertex can be used to quantify the degree of distortion. The cells with angles less than 25 degrees and greater than 155 degrees are defined as highly distorted cells.

To test the stability of the developed algorithm, a three-layered model having the top two layers of 10 m laying over 100 Ωm half-space is considered. The resistivity of the first and second layers are 50 Ωm and 10 Ωm, respectively. The model is discretized in three different ways. In the first case, orthogonal grids are used and the other two cases utilized distorted grids. The distorted grids are generated by randomly perturbing the orthogonal grids. The model, along with distorted girds for both the cases, is shown in Fig. 2.10. The angles formed at all vertexes are computed to ascertain the degree of distortion. The Fig. 2.11 illustrates these angles by histogram representation. The histogram shown in Fig. 2.11a corresponds to very few ($< 0.5\%$) highly distorted cells, whereas Fig. 2.11b corresponds to the large number ($> 10\%$) of highly distorted cells. The gird spacing for fine and the coarse cases are given by $[0.5] \times [1,2]$ and $[1] \times [2,4]$ respectively. The response was simulated using Schlumberger arrays at 25 points for both the distorted discretizations and compared with the orthogonal grids. The apparent resistivity plots for the fine models are shown in Fig. 2.12a. The misfit curves for fine and coarse grids are shown in Fig. 2.12b. The error plots show less than 1.1% error even for the highly distorted case for fine grids. For

coarse grids, it is seen that the error increases and it is observed that the coarsening in the z-direction leads to such misfit trends. It was observed that if the coarsening is performed only in x-direction and not in the z-direction, the error trend does not change significantly when comapred with the fine model. Interestingly, the misfit of the coarse-orthogonal case is a little more than the coarse-distorted grid's response. It is due to a special characteristic of the MFDM operator, which turns to 9-point stencil formula for a distorted grid; however, it is a 5-point stencil operator for a square grid. These experiments demonstrates the versatility and robustness of the developed algorithm in modeling complex geological scenarios. The stability experiment exhibits that the proposed algorithm is suitable for 2D trans-dimensional Bayesian inversion workflow, as explained in the introduction, which is considered a state-of-the-art data analysis scheme in the present times.

2.4.5 Computational Aspects of Modeling

This subsection presents the computational aspects of the simulations done in this study. Table 2.2 shows the grid spacing information, condition number of system matrices, and the number of BICGSTAB iterations for convergence to a tolerance of 10^{-8}, for all the experiments and at all five wavenumbers. From this data, it is observed that the iteration count decreases with an increase in wavenumber. It is on the expected line because the wavenumber dependent terms are added to the diagonal, thus, making the matrix relatively diagonally dominant. On the contrary, the condition number shows an increasing trend with wavenumber. It can be attributed to the absence of the wavenumber term in the surface boundary condition equation, which influences the smaller eigenvalues. Consequently, the smallest eigenvalues remain comparable with different wavenumbers. However, the larger eigenvalues increase with wavenumber to account for the raise in trace of the system matrices. Therefore, it leads to the increase in condition number with wavenumber. To examine this behavior, the eigenvalue analysis of all the system matrices is studied. The eigenvalue plots for the low-contrast dyke model for all five wavenumbers are illustrated in Fig. 2.13. An eigenvalues clustering is observed with the increase in wavenumber value. The convergence of a Krylov subspace-based method depends on the clustering of eigenvalues which explains the faster convergence for higher wavenumbers. To show the convergence of the iterative solver, Fig. 2.14 displays the residual versus iteration number plots for the three-layer model used in the stability analysis test for wavenumber $k1$ and $k3$. As expected, the coarsening of the grid reduces the number of iterations. Furthermore, the number of iterations reduces to approximately half by doubling the grid spacing. It is observed that the convergence for highly distorted grids shows a non-smooth behavior, whereas the convergence in the case of orthogonal grids is

relatively smooth. However, both take roughly the same number of iterations. Therefore, the MFDM method is both stable and efficient with regard to grid distortions. The same analysis is carried out for other models and the trends are found to be similar.

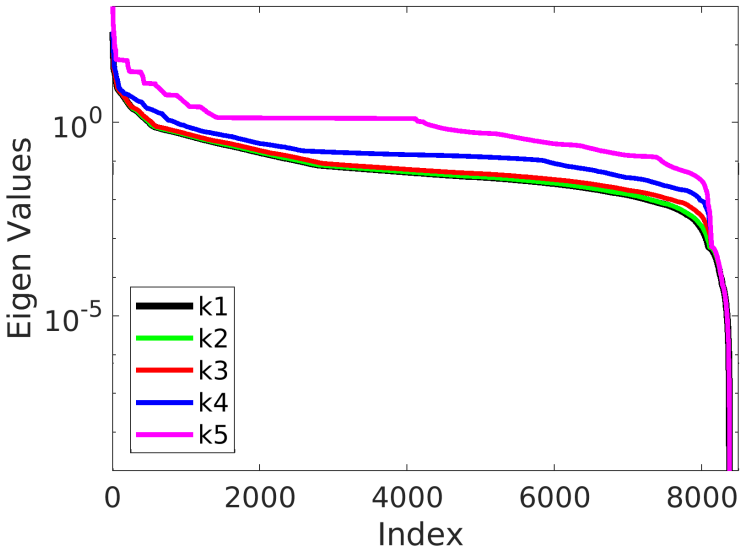

Fig. 2.13 Eigen value plot for low contrast fine dyke for all the wavenumbers

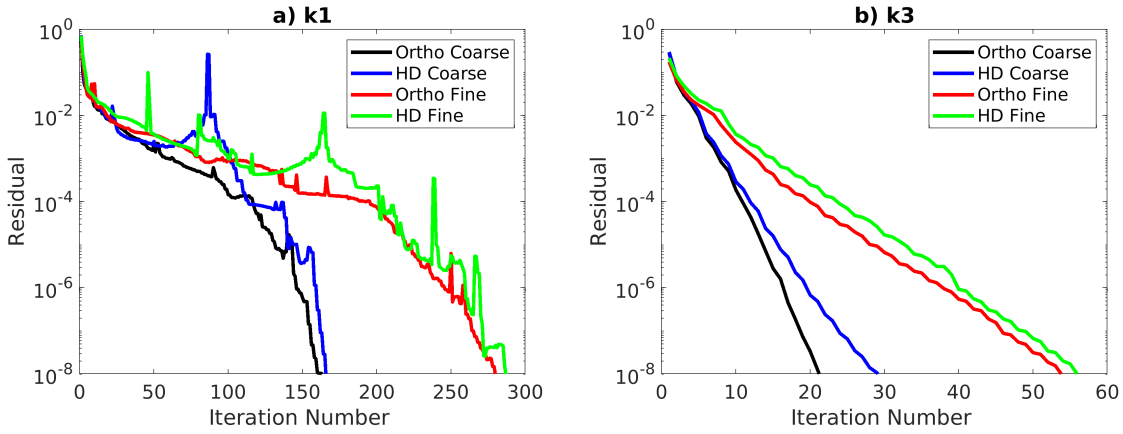

Fig. 2.14 Residual plots for two different wavenumbers k1 and k3 with respect to iteration numbers for the stability analysis model (a) residual plots for four different cases for wavenumber k1 1) solid black line corresponds to the orthogonal coarse grids, 2) solid blue line corresponds to high levels of distorted coarse grids, 3) solid red line corresponds to the orthogonal fine grids and (4) solid green line corresponds to high distortion tests for fine grids (b) the same analysis is repeated for wavenumber k3

Models & Cell Size (m) Type : $[x_{min} - x_{max}]$ $\times [z_{min} - z_{max}]$ meters	Wavenumber	Fine		Coarse	
		Iter	Cond No.	Iter	Cond No.
Dyke (low contrast)	k1	180	2.8344e+11	83	1.7789e+10
Fine:$[0.5-5] \times [0.5-5]$	k2	69	2.8345e+11	39	1.7793e+10
Coarse:$[1-10] \times [1-10]$	k3	33	2.8376e+11	15	1.7873e+10
	k4	12	2.8763e+11	7	1.8875e+10
	k5	5	1.6533e+12	3	2.1768e+11
Dyke (high contrast)	k1	159	2.8334e+12	92	1.6111e+11
Fine:$[0.5-5] \times [0.5-5]$	k2	70	2.8336e+12	35	1.6116e+11
Coarse:$[1-10] \times [1-10]$	k3	29	2.8366e+12	15	1.6191e+11
	k4	12	2.8753e+12	7	1.7131e+11
	k5	5	3.3326e+12	4	2.8361e+11
Anisotropy	k1	125	9.8139e+11	70	8.4058e+10
Fine:$[0.5] \times [1-2]$	k2	49	9.8236e+11	27	8.4408e+10
Coarse:$[1] \times [2-4]$	k3	11	9.9937e+11	6	9.0516e+10
	k4	3	2.4879e+12	2	8.5188e+11
	k5	2	2.9014e+13	1	1.0062e+13
Topography	k1	377	8.2712e+12	203	6.5615e+11
Fine:$[0.5-5] \times [0.5-5.6]$	k2	234	8.2716e+12	121	6.5628e+11
Coarse:$[1-10] \times [1-5.6]$	k3	62	8.2786e+12	31	6.5852e+11
	k4	18	1.7569e+13	9	2.7875e+12
	k5	6	2.0805e+14	5	3.3009e+13
Ortho Three Layer	k1	140	9.2201e+11	81	7.9814e+10
Fine:$[0.5] \times [1-2]$	k2	84	9.2224e+11	42	7.9896e+10
Coarse:$[1] \times [2-4]$	k3	29	9.2622e+11	11	8.1316e+10
	k4	6	9.7598e+11	4	9.9242e+10
	k5	2	1.5709e+12	2	3.6124e+11
HD Three Layer	k1	145	9.2201e+11	82	7.9814e+10
Fine:$[0.5] \times [1-2]$	k2	82	9.2224e+11	41	7.9896e+10
Coarse:$[1] \times [2-4]$	k3	30	9.2622e+11	15	8.1316e+10
	k4	9	9.7598e+11	6	9.9242e+10
	k5	4	1.5709e+12	2	3.6124e+11

Table 2.2 Table shows the discretization parameters for fine and coarse grids for all the models. The iteration count (Iter) for the convergence of the BICGSTAB (precondition with incomplete LU with zero filling) to a tolerance of 10^{-8} is shown for all the wavenumbers for fine and coarse grids. The corresponding condition numbers (Cond No.) are also mentioned in the table.

2.5 Conclusions

A robust and versatile algorithm to model the 2D DC resistivity data is developed. The underlying discretization scheme is derived from the MFDMs (also known in literature as support-operator methods, reference operator methods). The developed algorithm is first tested with dyke models and anisotropic model, where the analytical solution guarantees the accuracy of the developed work. The analysis of the resulting misfit shows that the maximum error is less than 1% for the low contrast, finely discretized dyke model, however, for a high contrast model, the maximum error is around 5% for the fine discretization for large offset. We also show the applicability of our work for modeling DC resistivity response for a sinusoidal topography (mountain-valley model). Finally, the stability of the developed algorithm is analysed for non-orthogonal grids. The numerical tests are conducted with varying degrees of distortions. The cells with vertex angle less than 25 degrees and greater than 155 degrees are referred to as highly distorted cells. The numerical error caused by distortion remains below 1.1% for fine discretization even for the case where 10% of cells are highly distorted. It is also noted that while convergence for orthogonal grids is generally smooth, it exhibits a non-smooth behaviour for highly distorted grids. Both require about the same amount of iterations, though. As a result, in terms of grid distortions, the MFDM approach is both efficient and stable. For other models, the same analysis is performed, and comparable trends are discovered. This verifies that the developed algorithm can be implemented to model complicated geological scenarios where the orthogonality of the grids needs to be violated to accommodate the complex structures.

Chapter 3

A versatile 2D DC Resistivity modeling algorithm in the space domain

3.1 Abstract

2D direct-current resistivity modeling is generally done in the wavenumber domain to efficiently accommodate the 3D character of the source. For faster computation, the wavenumber domain solutions are calculated at around half a dozen wavenumbers. However, the collection of wavenumbers and associated weights that are selected has a significant impact on the accuracy of the solution that is thus obtained in the space domain. It has been shown in numerous forward modeling studies that selecting effective wavenumbers is difficult, particularly for complex models, including topography, anisotropy, and high resistivity contrasts. In this study, we develop an optimized strategy to omit the dependency of the 2D modeling problem on the wavenumbers. Instead of using the wavenumbers domain approach, the problem is solved in the space domain using a new boundary condition derived in this study. It requires only a few grids in the direction perpendicular to the profile. Several numerical experiments are conducted to conclusively demonstrate that the developed algorithm is robust and versatile concerning subsurface and survey parameters.

Keywords:Numerical methods, Algorithms, 2D DC resistivity modeling, Mimetic methods, Boundary conditions

3.2 Introduction

The 3D nature of the source in Direct-Current (DC) resistivity modeling prevents us from representing the governing equation using two-space variables only. Consequently, DC modeling for 2D models is also referred to as 2.5D modeling, and generally, the 2D DC problem is solved in the wavenumber domain. Several studies have been done to select the best possible wavenumbers needed for efficiently transforming the response in the space domain. [115] discuss a scheme for choosing the best collection of equispaced wavenumbers in logarithmic scale. [157] presented an optimization approach to calculate wavenumbers for different modeling experiments. [113] describes a modified method built upon Xu's approach for choosing the wavenumbers more optimally. The most advantageous coefficients are obtained by the optimization strategy using a gradient-based search. However, this affects the computational cost and is specific to a particular geometry. [109] offered a new approach to handle the non-linear optimization problem for estimating the suitable Fourier coefficients to provide a precise 2D approximation. While [146] and [40] use eight wavenumbers, [74] uses two different sets of wavenumbers for the forward modeling. Despite these efforts, there is no universal best choice for the wavenumbers to be applied for space-domain transform.

Studies have reported that complex models require large wavenumbers to simulate the response for forward modeling. According to [166], when five wavenumbers are employed for forward modeling, the traditional FEM crosses an inaccuracy of 30 % for a 2-layer model at an offset of 100 m. [25] uses ten wavenumbers to simulate response for a four-layered model. They also highlighted that the effectiveness of wavenumbers can also get affected by electrode spacing, which makes it non trivial to perform an optimal selection. For efficient computations, the modeling algorithms frequently use small wavenumbers [170]. However, determining the total number and distribution of wavenumber are vital in selecting the optimum wavenumbers. Theoretically, the answer is more accurate when more wavenumbers are utilized. So far, there is no method for selecting the wavenumbers for a generic inhomogeneous model; all of these approaches rely on analytical answers of basic models. As a result, the employment of a small number of wavenumbers, the discretization of the model, and the applicability of the artificial mixed boundary condition all contribute significantly to the computation errors for 2D modeling.

[159] emphasize the need to use many wavenumbers for accuracy at higher offset and for anisotropic models. It was shown that simple isotropic models could be dealt with roughly around ten wavenumber values, whereas the anisotropic model requires 92 wavenumbers. [140] emphasize using enhanced wavenumbers and weights as the

model gets more complicated. Having dealt with different studies highly dependent on wavenumbers; we seek to design a strategy where the 2D DC forward modeling can be done without the wavenumbers.

In this paper, a space domain DC modeling technique for 2D models is developed to overcome the challenges posed by the wavenumbers' selection for 2D modeling. Firstly, the motivation is presented, and the need to develop the algorithm is highlighted. Next, a boundary condition is developed for the plane where the source is placed. Then, the numerical experiments used for bench-marking are presented, along with applications of the algorithm to complex models with embedded block and topography. Finally, the discussion and conclusion are presented where the novelty of the algorithm is also presented.

3.3 Motivation

In this section, we examine the performance of various wavenumbers reported in the literature using a half-space model of resistivity 10 Ωm. First, the analytical formula calculates potential values [36] in the wavenumber domain up to 1 km from the current electrode. Subsequently, the responses are transformed in the space domain employing wavenumbers and corresponding weights reported in different studies [40, 74, 109, 140, 157].

The space-domain transformation is also performed by the Gauss-quadrature method to explore the minimum wavenumbers required for accurate estimation for the 1 km offset range. To obtain accurate responses in both near and far offset, it is observed that the integration needs to be performed at least over two intervals. We carried out the integral over 0 to 0.1 and 0.1 to 5 intervals using 64 points abscissas for each interval. The simulation results, along with the analytical solution, are shown in Fig. 3.1.

The analysis of the obtained response reveals that all methods provide a reasonably accurate response in the near offset range, almost up to 80 m. None of the methods is accurate beyond 400 m offset, except the Gauss-quadrature scheme. However, the Gauss quadrature necessitates calculating response at 128 wavenumbers for accurate results. We tested the Gauss quadrature with various n-points abscissas and observed that at least 40-points abscissas Gauss-quadrature integral over two intervals is essential for good accuracy up to 1 km offset. Therefore, obtaining accurate solutions at long offset is computationally expensive, even while dealing with a simple case of a half-space model. Thus, for a reasonably accurate evaluation of the space-domain response for

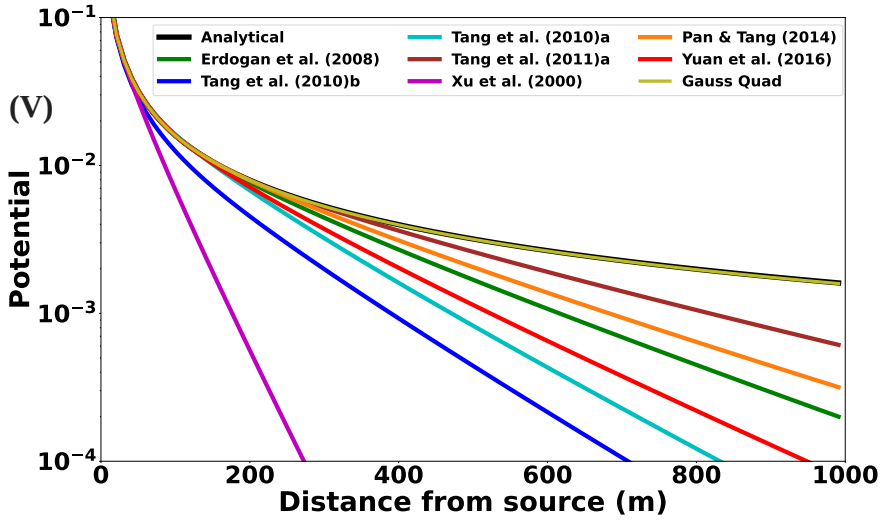

Fig. 3.1 The electric potential in Volts (log scale) versus the distance plots for a 10 Ωm halfspace obtained using different sets of wavenumbers and weights reported in the literature and computed employing Gauss-quadrature method, along with the analytical solution.

complex subsurfaces such as variable topography, anisotropic resistivity would increase the computation cost.

There have been other studies reported in the literature that have applied correction methods to improve the accuracy of the wavenumber domain simulations. [113] presented a source singularity correction and optimization technique to obtain accurate results in the space domain. The study also mentions that the correction technique may not hold for large conductivity contrasts. [40] & [35] use correction measures for obtaining accurate results, where they employ a normalization technique using a 1 Ωm halfspace responses. There may be other such techniques that could improve the space-domain results' accuracy. The above list is not exhaustive but an indicator of improvement techniques that could be used in modeling studies. This paper presents a versatile unconventional method that performs 2D DC resistivity modeling directly in the space domain. This method works on an additional boundary condition derived in this study. Furthermore, the electrodes need not be perfectly aligned along a straight line as may be required for many wavenumber-domain schemes; this method can easily handle the resulting deviations.

3.4 Method

The governing equation for 3D DC resistivity modeling can be written as,

$$\nabla_{3D} \cdot [T_{3D}(x, y, z)\nabla_{3D} u(x, y, z)] = -I\delta(x - x_\circ)\delta(y - y_\circ)\delta(z - z_\circ) \tag{3.1}$$

on V, where V is the computational domain. $\nabla_{3D}\cdot$ and ∇_{3D} are the divergence and gradient operators, respectively in the 3D space. $T_{3D}(x, y, z)$ is the conductivity tensor. The R.H.S term denotes the source term, where I is the current intensity, $\delta()$ is the delta function, and $(x_\circ, y_\circ, z_\circ)$ represents the coordinates of the source. The equation (3.1) is solved under the following boundary condition,

$$\frac{\partial u(x, y, z)}{\partial n} = 0 \tag{3.2}$$

at the surface where n denotes the outward normal to the surface. At other boundaries, the boundary conditions try to make the domain unbounded and generally a mixed boundary condition given by [36] provides good results. For general anisotropic media, all nine elements of the conductivity tensor could be non-zero. However, for 2D medium with a strike direction in the y-direction, the conductivity tensor for anisotropic subsurface can be expressed as,

$$\hat{T}_{2D} = \begin{bmatrix} \sigma_{xx} & 0 & \sigma_{xz} \\ 0 & \sigma_{yy} & 0 \\ \sigma_{zx} & 0 & \sigma_{zz} \end{bmatrix}. \tag{3.3}$$

For the above definition of conductivity tensor, equation (3.1) can be written using 2D differential operator as,

$$\nabla_{2D} \cdot [T_{2D}(x, z)\nabla_{2D} u(x, y, z)] + \sigma_{yy}\frac{\partial^2 u(x, y, z)}{\partial y^2} = -I\delta(x - x_\circ)\delta(y - y_\circ)\delta(z - z_\circ), \tag{3.4}$$

where subscript $_{2D}$ denotes the operator in the 2D space and conductivity tensor for 2D medium can be given as,

$$T_{2D} = \begin{bmatrix} \sigma_{xx} & \sigma_{xz} \\ \sigma_{zx} & \sigma_{zz} \end{bmatrix}. \tag{3.5}$$

In case of a 2D model, the DC problem can be solved in wavenumber domain, therefore, using the Fourier transform, equation (3.4) in wavenumber domain can be written as,

$$\nabla_{2D} \cdot [T_{2D}(x, z)\nabla_{2D}\hat{u}(x, k_y, z)] - k_y^2 \sigma_{yy}\hat{u}(x, k_y, z)] = -Ie^{\iota k_y y_\circ}\delta(x - x_\circ)\delta(z - z_\circ). \tag{3.6}$$

If we consider that the origin of coordinate system lies on the plane $y_\circ = 0$, the R.H.S of equation (3.6) will not depend on the wavenumber, k_y. Under this condition, the solution, $\hat{u}(x, k_y, z)$, obtained by solving equation (3.6) will be an even function of k_y and it is also real valued. Therefore, using the property that the Fourier transform of a real-even function will also be a real-even function ensures that the potential in space domain for 2D model will also be a real valued even function with the symmetry about $y = y_\circ$ plane. Because the first order derivative of even function at the plane of symmetry vanishes, mathematically, it can be expressed as boundary condition at a plane $y = y_\circ$ for equation (3.4) as,

$$\frac{\partial u(x, y, z)}{\partial y}|_{y=y_\circ} = 0 \tag{3.7}$$

Therefore, we propose a scheme to solve the 2D resistivity problem in space domain using equation (3.4) under the boundary conditions given in equation (3.2) at surface, equation (3.7) on $y = y_\circ$ plane and the mixed boundary condition on rest of the boundaries. Even though the problem can be solved using various numerical methods, like finite element method (FEM) [167, 171], finite-difference method (FDM) [40], we choose to work with mimetic finite difference method (MFDM). The MFDM can work with non-orthogonal grids and is very stable with respect to the aspect ratio of cells. The details of MFDM can be found in [128] and [129]. However, for completeness, a brief discussion on the MFDM is provided in this paper.

The support-operator approach, reference operator, etc. are some of the terms for MFDM that have been used in the literature [64, 65, 101]. MFDM are a special class of finite-difference methods which mimics the properties of the original continuum differential operators. Their ability to work with non-orthogonal, highly distorted rough grids has proved remarkable to work with complex topography [88]. It is well-suited to work with models incorporating highly variable discontinuous physical properties. Since the MFDM uses coordinate invariant operators like gradient, divergence, and curl, it can be applied to any system of coordinates. Using the coordinate invariant definition of the

divergence operator, for any vector $\vec{A}$ defined over the edges of a cell, we can write,

$$\nabla \cdot \vec{A} = \lim_{V \to 0} \frac{\oint_{\partial V} (\vec{A}.\vec{n}) dS}{V}. \tag{3.8}$$

The above definition is then translated to an equivalent expression for a discrete case. This can be done by taking a cell $\Omega_{(i,j)}$ with the boundary given by $\partial\Omega$. The expression for the integral in equation (3.8) can be given in the form of a cell integral for a particular cell by,

$$\begin{aligned} \oint_{\partial\Omega} (\vec{A}.\vec{n}) dS = &\int_1 (\vec{A}.\vec{n}) dS + \int_2 (\vec{A}.\vec{n}) dS \\ &+ \int_3 (\vec{A}.\vec{n}) dS + \int_4 (\vec{A}.\vec{n}) dS \end{aligned} \tag{3.9}$$

where the subscripts, $1, 2, \cdots, 4$ denote the line integrals on the four different sides of the cell. The normal vector ($\vec{n}$) for any of these lines can be obtained by using the x and y-coordinates of the cell nodes. The line integrals in the equation (3.9) can be then converted into a summation formula for the discrete case. This gives us the discrete divergence operator for a given cell (i,j). Once the discrete divergence operator is in place, it is easy to construct the discrete gradient operator by following the adjointness property between the gradient and the divergence operators [29, 60]. The discrete divergence opertaor, gradient operator and the conductivity/resistivity tensor can then be utilized to obtain the discrete formulation for the DC resistivity problem (equation (3.4) or (3.6)). For more details, readers can refer to our previously developed wavenumber-domain 2D DC modeling algorithm based on MFDM approach [139]. Here, the equation (3.4) is solved using the proposed scheme, involving the boundary condition at the plane $y = y_o$. By writing the discrete equation for each cell, we can obtain the linear system of equations for the entire system. This finishes the short discussion on the implementation part of the MFDM. The code developed here using the MFDM approach and the boundary condition discussed above will be termed as $Mim2.5D$ in the subsequent sections. The following section presents the numerical experiments and results to show the accuracy and efficiency of the proposed algorithm.

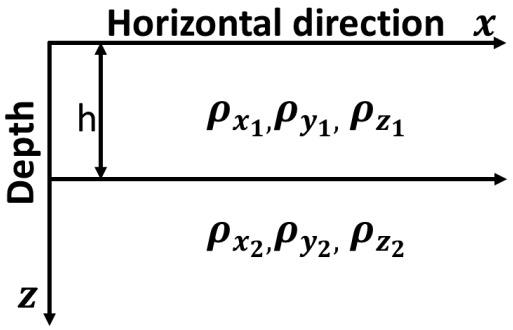

Fig. 3.2 General representation of the two-layer model used for numerical experiments. h represents the thickness of the first layer. Subscript $_1$ and $_2$ represent 1^{st} and 2^{nd} layer, respectively while ρ_x, ρ_y and ρ_z denote the resistivities in the x, y, and z-direction respectively.

3.5 Numerical Experiments

3.5.1 Algorithm benchmarking

Extensive simulations were carried out to check the proposed algorithm's accuracy and efficiency. This section presents simulation results performed over two-layer models guided by the availability of an analytical expression for anisotropic two-layered models [150]. For comparison, responses are also calculated using a wavenumber-domain approach using the algorithm developed by [139]. In this experiment, the first set of simulations is done for the isotropic two-layered model, and the second is carried out for the anisotropic case. The results presented here are for 2D DC simulations using different sets of wavenumbers available in the literature and the proposed $Mim2.5D$ scheme. We compare the apparent resistivity obtained against the analytical results.

A schematic diagram of a two-layered model is shown in Fig. 3.2, where the subscripts $_1$ and $_2$ denote the first and second layers, respectively. The thickness of the first layer is denoted by h meters. The subscripts x, y, and z, denote the horizontal x-direction, perpendicular to the profile (y-direction) and the depth, respectively. The grid size is kept at 5 meters in the x-direction. In the z-direction, the grid size is 2 meters for the first 50 meters, and 5 m is kept till 100 m and 20 m further. The seven extra grids are padded to the model boundaries, where the grid spacing increase by a factor of 1.75 in the outward directions. For $Mim2.5D$, 12 grids having spacing 5 m at the plane where the current electrode is kept, and increasing grid spacing away from this plane is used for discretization in the y-direction. It is to be noted that we only need discretization on one side of the plane. Using the same discretization, simulations are performed for all three

Table 3.1 Model parameters for the different two-layer tests performed.

Tests	Model / Thickness (1^{st} Layer)	1^{st} Layer	2^{nd} Layer
Test 1	Low Contrast Isotropic / 30 m	$\rho_{x1} = \rho_{y1} = 100\,\Omega m$ $\rho_{z1} = 100\,\Omega m$	$\rho_{x2} = \rho_{y2} = 10\,\Omega m$ $\rho_{z2} = 10\,\Omega m$
Test 2	High Contrast Isotropic / 30 m	$\rho_{x1} = \rho_{y1} = 1000\,\Omega m$ $\rho_{z1} = 1000\,\Omega m$	$\rho_{x2} = \rho_{y2} = 10\,\Omega m$ $\rho_{z2} = 10\,\Omega m$
Test 3	High Contrast Anisotropic / 30 m	$\rho_{x1} = \rho_{z1} = 1000\,\Omega m$ $\rho_{y1} = 100\,\Omega m$	$\rho_{x2} = \rho_{z2} = 10\,\Omega m$ $\rho_{y2} = 1\,\Omega m$
Test 4	Low Contrast Isotropic / 20 m	$\rho_{x1} = \rho_{z1} = 100\,\Omega m$ $\rho_{y1} = 100\,\Omega m$	$\rho_{x2} = \rho_{z2} = 10\,\Omega m$ $\rho_{y2} = 10\,\Omega m$

models for a pole-pole array. The minimum and maximum electrode spacings are 2.5 m and 400 m, respectively, with an increment of 5 m. Table 3.1 shows resistivity values for all four models considered for benchmarking tests. The thickness of the first layer is fixed at h = 30 m for all Tests 1, 2, and 3, and h = 20 m for Test 4.

For Test 1 (Low Contrast Isotropic, refer to Test 1, Table 3.1), Fig. 3.3(a) shows the apparent resistivity curves vs. the electrode distance from the source. It is observed that the response from the 2D code for various wavenumbers from the literature tends to deviate from the analytical response. The electrode distance at which the curves deviate from the analytical response depends on the weights and the chosen wavenumber. However, all methods work well in the near offset up to 40 m electrode distance. On the other hand, the $Mim2.5D$ response is in good agreement with the analytical solution and shows a good match at all offset values. For Test 2 (High Contrast Isotropic, refer to Test 2, Table 3.1), Fig. 3.3(b) shows that all the simulations using different wavenumbers agree up to an initial 30 m. Again, the maximum electrode distance up to which the responses are reasonably accurate varies with wavenumber's schemes; however, the $Mim2.5D$ solution follows the analytical apparent resistivity curves even for large offsets. For Test 3 (High Contrast Anisotropic two-layer model, refer to Test 3, Table 3.1), Fig. 3.3(c) shows the apparent resistivity curves. The offset range for which all the wavenumber solutions agree with the analytical solution is not well defined because the solution [157] deviates from a very close range. [140] see the maximum agreement by wavenumber solutions. Again, in this test, the $Mim2.5D$ solution agrees well with the analytical solution, even for large

offsets. To test the effect of the thickness of the first layer, a model (Low Contrast Isotropic, refer to Test 4, Table 3.1) with 20 m thickness of the first layer is experimented with, and the apparent resistivity curves are shown in Fig. 3.4. It is easy to conclude that the $Mim2.5D$ solution agrees well with the analytical solution till a large offset. To illustrate the impact of first-layer thickness, the absolute error with the analytical result is calculated for all the simulations done in Test 1 and Test 4. For both the experiments, the misfit plots are shown in Fig. 3.5(a) and (b). It is observed from these plots that the varying depths do not have a bearing on the accuracy of the solution, indicating the algorithm's stability.

3.5.2 2D block model

The previous section concludes the benchmarking exercise. This section simulates the DC response for an embedded block of $10\,\Omega m$ in a homogeneous background of $100\,\Omega m$. Fig. 3.6 shows the schematic of the model setup. The depth of the inserted block is kept at 30 m. The dimensions of the inserted block are given by the parameters a, b, and d. Source (S) is placed at -200 meters. The potentials are calculated on the surface using a minimum and maximum electrode spacing of 2.5 to 400 m. The minimum x-grid and z-grid sizes are kept at 5 meters and 2 meters, respectively. Three different experiments are done to simulate the response by varying the size of the embedded block inside the homogeneous medium. All simulations are performed using a pole-pole array. Test 1: a = 0, b = 30 m, d = 30 m. This is equivalent to a $30\,m \times 30\,m$ block inserted exactly below the origin, 200 m away from the source. Test 2: a = 150 m, b = 150 m, and d = 30 m. Test 3: a = 150 m, b = 150 m, and d = ∞ (the block runs across the entire depth of the model).

Fig. 3.7 shows the apparent resistivity profiles for all three tests performed. The solid line corresponds to the apparent resistivity profiles of the developed algorithm in the space domain, and the dashed line corresponds to the apparent resistivity profiles obtained from the wavenumber domain simulation. It is observed that the results from the wavenumber and space domain agree with each other for Test 1 and Test 2, but there is a deviation in the case of Test 3. It should be emphasized that our algorithm works on primary and secondary field decomposition where the primary field is known in the space domain. Hence, a 2D block results in a secondary field around the block which is transformed into a space domain in the case of the wavenumber-domain algorithm. The horizontal dimension of models for Test 2 and Test 3 are the same. However, the wavenumber-domain response for Test 3 shows a significant deviation from the space-domain response compared to the Test 2 case. The secondary field at large offsets comes from the deeper parts. Because the response of Test 2 at large offsets is dominated by the primary response, therefore, it has a good match at all offset values. However, this is not the case for the

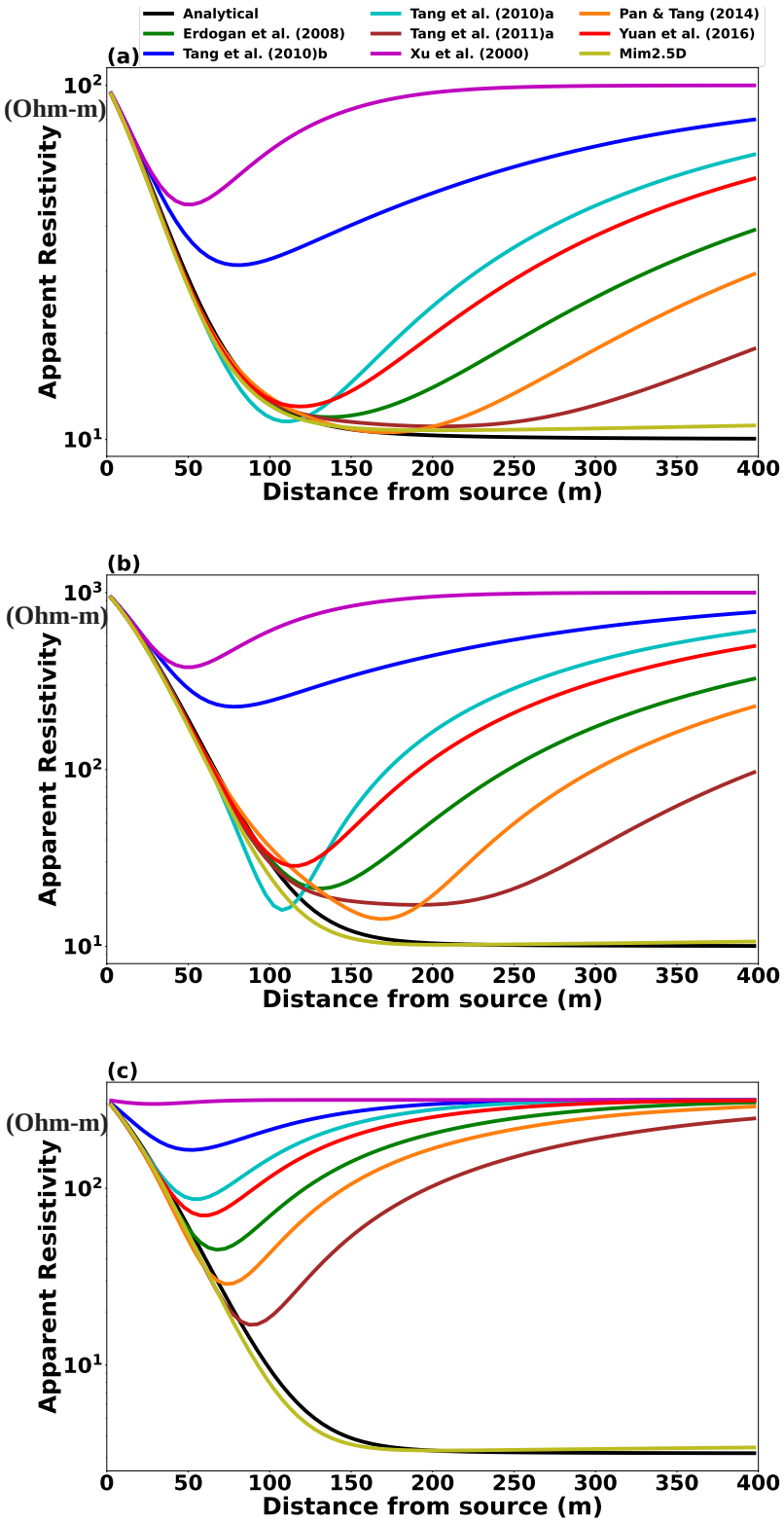

Fig. 3.3 Apparent resistivity curves (log scale) obtained from various wavenumber techniques, reported in the literature and calculated using the proposed scheme along with the analytical response [150]; (a) Test 1 (Low Contrast Isotropic model); (b) Test 2 (High Contrast Isotropic model); (c) Test 3 (High Contrast Anisotropic model).

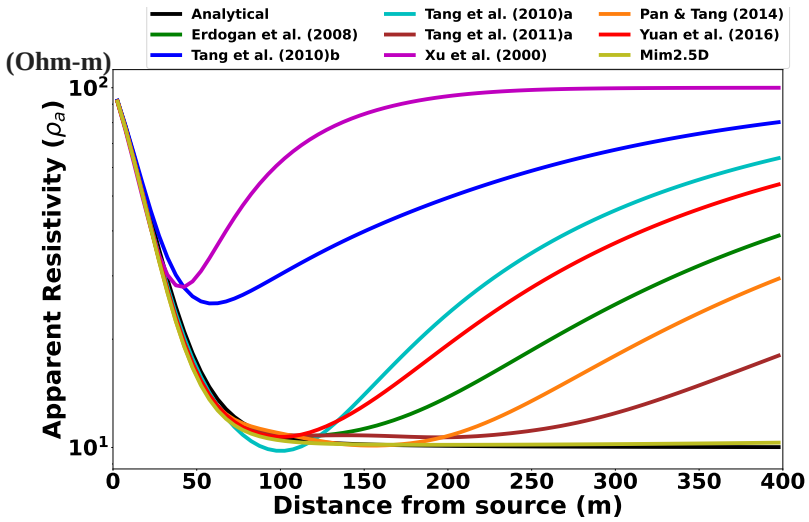

Fig. 3.4 Apparent resistivity curves (log scale) obtained from various wavenumber techniques, reported in the literature and calculated using the proposed scheme along with the analytical response [150] for Test 4 (Low Contrast Isotropic model). The depth of the first layer is kept at 20 meters.

model used for Test 3. Consequently, in the case of primary/secondary decomposition, the wavenumber-domain schemes would work well for a subsurface where anomalous bodies are buried in a homogeneous host rock.

3.5.3 Three Layer topography simulations

This section discusses the three-layer variable topography model. The maximum amplitude of the sinusoidal topography is kept as 20 meters, and the thickness of the first and second layers are fixed at 30 meters. The third layer extends to infinity or the entire depth of the model. The simulations are performed on isotropic, vertically transverse isotropic (VTI) and tilted transverse isotropic (TTI) models. Table 3.2 shows the different parameters for the three-layer topography tests. Fig. 3.8 shows the resistivity map for the TTI topography model where the mesh used for model discretization is overlaid on the images. The same mesh is used for all the tests done for the topography models. The position of the current electrode is shown with a red star, and the inverted black triangles denote the position of potential electrodes. The potential-electrode spacing is 20 m in the horizontal direction, and they are placed on the surface of the model. The resistivity tensor for the TTI case is obtained by applying a rotational transform on the VTI tensor as $T_{2D_{TTI}} = R(\theta) \times T_{2D_{VTI}} \times R(\theta)^T$, where $R(\theta)$ is the rotational matrix, $T_{2D_{VTI}}$ is VTI tensor and ^{T} denote matrix transpose. The angle θ used here follows the slope of the topography.

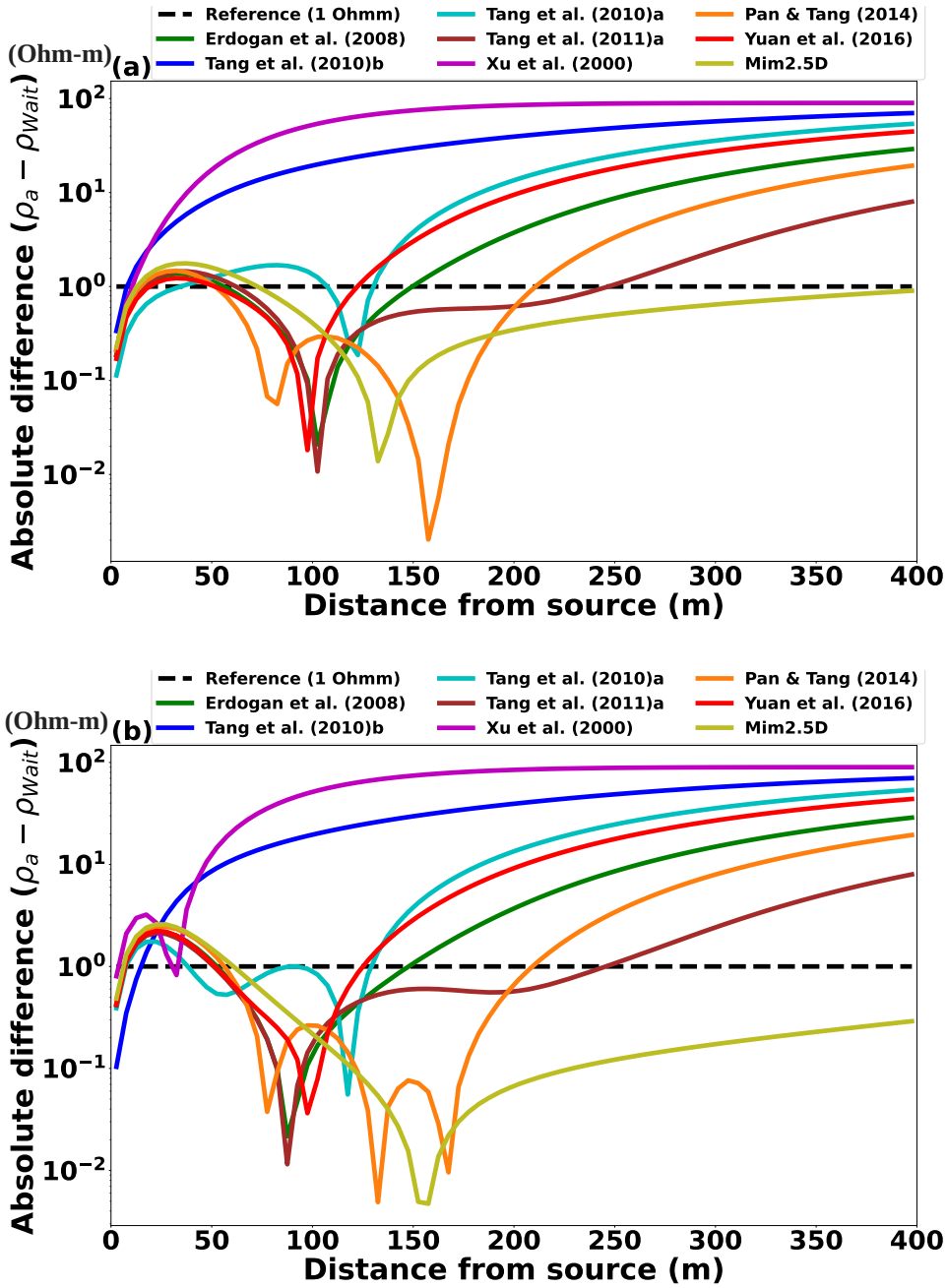

Fig. 3.5 Plots of absolute errors obtained for a) Test 1 - Low contrast isotropic (thickness of 1st layer = 30 meters); b) Test 4 - Low contrast isotropic (thickness of 1st layer = 20 meters).

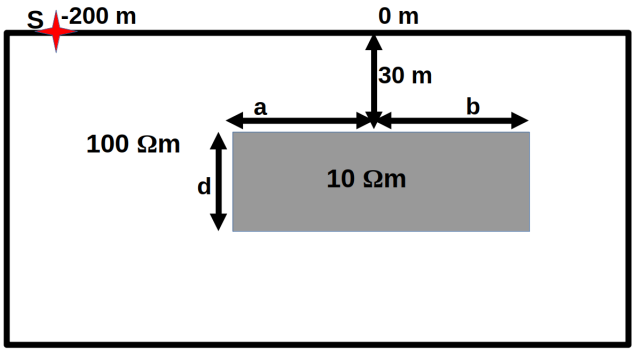

Fig. 3.6 2D Block of $10\,\Omega m$ inserted in homogeneous subsurface of $100\,\Omega m$ at a depth of 30 m. The source location, denoted by S, is fixed at -200 m. The dimensions of the inserted body are given by the parameters a, b, and d. Three tests are performed by varying the parameters a, b, and d.

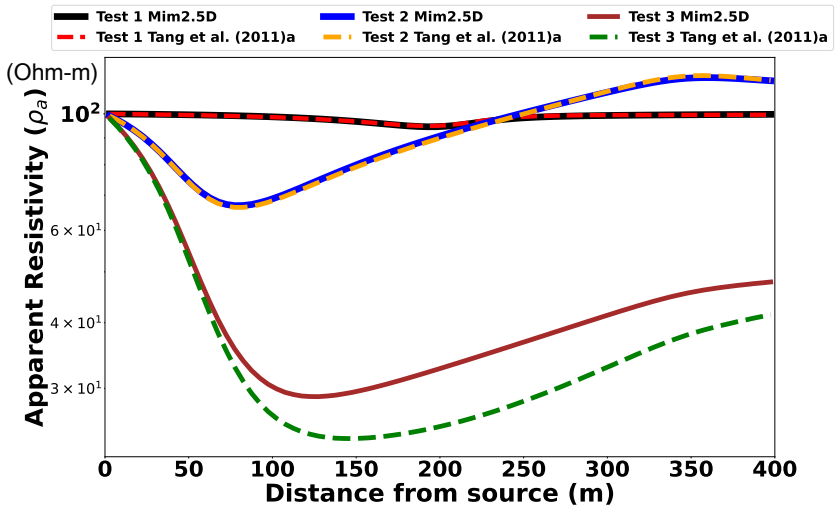

Fig. 3.7 Apparent resistivity curves obtained for the three tests performed on inserted 2D Block of $10\,\Omega m$ in homogeneous subsurface of $100\,\Omega m$ at a depth of 30 m. The solid line denotes the solutions obtained from the proposed algorithm (Mim2.5D), and dashed lines are the solutions obtained from the wavenumber domain simulations.

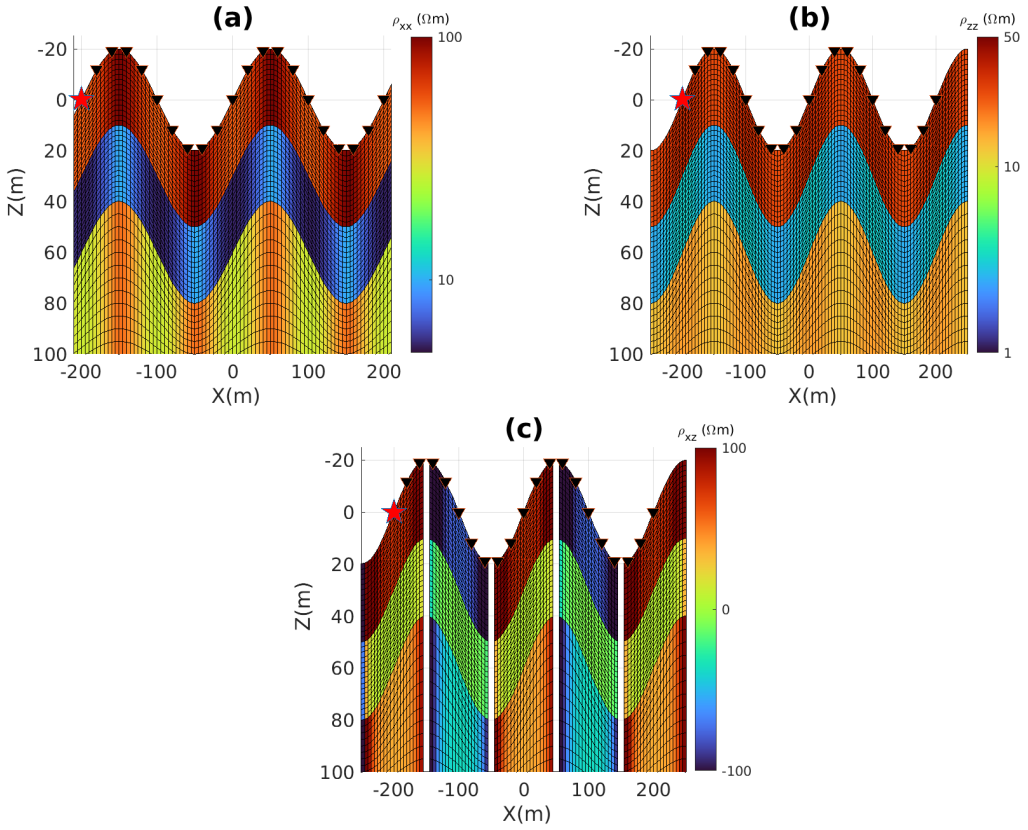

Fig. 3.8 Resistivity maps for the topography models for tilted transversely isotropic (TTI) experiments. a) shows the xx component of the resistivity tensor, b) shows the zz component of the resistivity tensor, and c) shows the xz component of the resistivity tensor.

Therefore the TTI case follows topography (one component parallel to the topography and the other perpendicular to it). In Fig. 3.8c, a few white strips in the color map denotes the infinity resistivity (zero conductivity) values where the angle is zero pertaining to flat topography.

Fig. 3.9 shows the apparent resistivity curves for all the topography-model experiments viz. Isotropic, VTI, and TTI models. For comparison, the wavenumber-domain response for the isotropic case is also shown in this figure, as the accuracy of the algorithm used for the simulation of the topography model is already established [139]. As expected for layered models, there is some mismatch between wavenumber and space-domain responses. However, wavenumber and space-domain algorithms produce comparable results for the half-space model with topography from [117]. It can be seen from the apparent resistivity curves (Fig. 3.9) that the red line (TTI) follows topography because of the channeling of the current along the topography. The anisotropy in the TTI follows the topography; hence, the effect can be seen in the TTI curve.

Table 3.2 Model parameters for the three different tests performed on a three-layer variable topography model. Test 1, Test 2, and Test 3 correspond to the isotropic, vertically transverse isotropic (VTI), and tilted transverse isotropic (TTI) models, respectively.

Tests	Model	1^{st} Layer	2^{nd} Layer	3^{rd} Layer
Test 1	Isotropic	$\rho_{x1} = \rho_{y1} = 100\,\Omega m$	$\rho_{x2} = \rho_{y2} = 10\,\Omega m$	$\rho_{x3} = \rho_{y3} = 50\,\Omega m$
		$\rho_{z1} = 100\,\Omega m$	$\rho_{z2} = 10\,\Omega m$	$\rho_{z3} = 50\,\Omega m$
Test 2	VTI	$\rho_{x1} = \rho_{y1} = 100\,\Omega m$	$\rho_{x2} = \rho_{y2} = 10\,\Omega m$	$\rho_{x3} = \rho_{y3} = 50\,\Omega m$
		$\rho_{z1} = 25\,\Omega m$	$\rho_{z2} = 2.5\,\Omega m$	$\rho_{z3} = 12.5\,\Omega m$
Test 3	TTI	Resistivity depends on	the topography (for all	three layers)

Table 3.3 Computation time for Test 1 (Low Contrast Isotropic Model). * denotes the cumulative iterations and the cumulative time taken by the iterative solver for a five wavenumber approach [109].

Algorithm	BICGSTAB*	Direct Solver
	Iter/Time (s)	Time (s)
Wavenumber	152 / 0.115363	0.119097
Mim2.5D	256 / 1.901381	6.237999

3.6 Discussion

The numerical simulations presented in section 3.5.1 unambiguously highlighted the advantage of the developed algorithm, $Mim2.5D$, and the limitations of working with few wavenumbers. It was evident from the half-space experiment that we need several wavenumber domain simulations (of the order of a hundred) for accurate response at large electrode spacing. The calculations for the two-layered model indicate the fact that as we increase the conductivity contrast, the maximum workable electrode distance reduces for all the schemes. Furthermore, for an anisotropic model, the maximum electrode distance up to which the response could be accurate decreases. In fact, the best-case scenario starts deviating around 65 m. We also repeated these experiments by reducing the thickness of the first layer. It was observed that the maximum workable electrode distance does not show significant dependency on the thickness of the first layer for all the schemes. It is happening because the thickness of the first layer in the experiments presented in this study is smaller compared to the offset at which the wavenumber-domain response deviates from analytical solutions. Overall, this analysis shows that every scheme starts to fail beyond a particular electrode distance. Unfortunately, the maximum electrode distance depends on the subsurface model itself, which is known before inversion. However, inversion depends on the accuracy of the forward modeling algorithm itself. Inaccurate modeling shall impose a fictitious constraint on the model parameter estimation. This limitation of modeling can be overcome by employing more wavenumbers but comes with more computation cost.

The preceding experiment also illustrates that the proposed algorithm, $Mim2.5D$, provides a numerically accurate response for all the models and is versatile with subsurface geology and electrode spacing. However, the said robustness comes with some extra computation costs. For the computation time estimation, we demonstrate the proposed algorithm's performance compared to a five-wavenumber scheme [109] for the low contrast model (Test 1). The computation time for a preconditioned BICGSTAB and a direct solver is shown in Table 2. It is observed that the proposed scheme is approximately 16 times more expensive than a five-wavenumber scheme in the case of an iterative solver. For direct solver, the proposed scheme requires 55 times more time. However, it would turn out to be efficient, if one has to use wavenumbers of the order of hundred, in the case of complex models. Section 3.5.2 shows that the apparent resistivity curves for Test 1 and Test 2 are in agreement with each other. However, for Test 3, where the embedded block runs across the model's depth, the contribution of the secondary field dominates at large electrode separation. As a result, the apparent resistivity curves obtained for Test 3 from

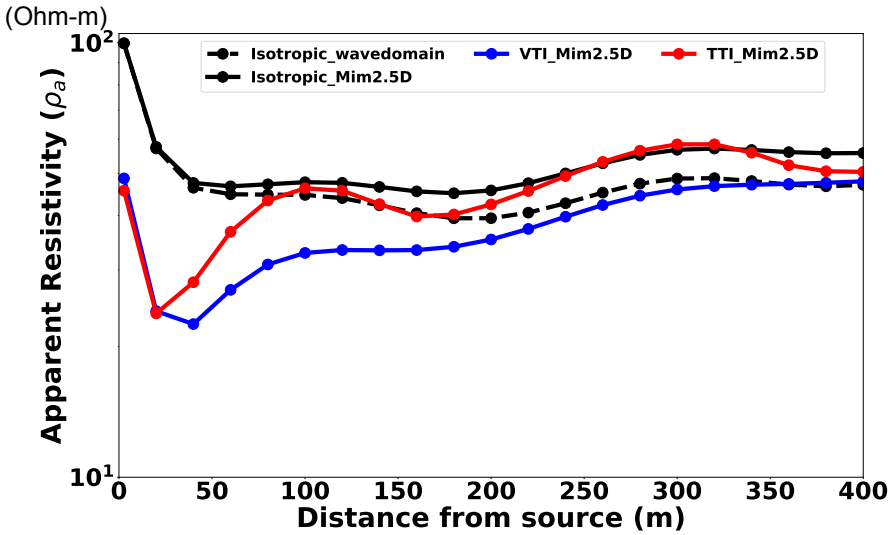

Fig. 3.9 Apparent resistivity curves obtained for the three tests performed on the variable topography model. The solid black line corresponds to the results from the developed Mim2.5D algorithm, the dashed black line corresponds to the wave domain solution for isotropic topography model, the blue line corresponds to the VTI, and the red line corresponds to the TTI topography model.

wavenumber domain and the Mim2.5D simulations deviate from each other after some distance.

Section 3.5.3 deals with three-layer topography simulations. The response obtained for this model shows that the apparent resistivity curve for TTI tries to mimic the topography relatively more than isotropic and VTI cases. It is primarily due to the channeling of the current along the topography for the TTI case, as the resistivity of the model follows the topography. Therefore, the proposed scheme can be utilized for studying the effect of topography and the anisotropy of the subsurface.

This paper presents an unconventional method for finding the solution in the space domain. The developed algorithm can be used to obtain results for large offsets. The applicability of the algorithm to complex geological structures, including topography, embedded block, and conductivity contrasts, is depicted using numerical experiments. A similar concept can be extended to other modeling studies, where the source exhibits 3D nature, and the modeling is to be conducted in a 2D model. It is important to note that all the wavenumber schemes discussed in the study assume all the electrodes in a straight profile. However, the proposed scheme can simulate the response for electrodes deviating from the profile. Therefore, we draw the conclusion that the proposed algorithm is a versatile and robust DC modeling scheme for 2D subsurface.

3.7 Conclusion

We developed a new scheme for modeling DC response for a 2D model. The proposed scheme computes the response in the space domain using a new boundary condition enforced on the plane where the current electrode is placed. An extensive benchmarking analysis is presented for comparison of the developed algorithm. The developed algorithm is also used to simulate response on a 2D block model of varying dimensions of the embedded block. The experiments of the rugged-topography model with isotropic, VTI, and TTI resistivity models further illustrate the robustness of the developed algorithm. We compare the proposed algorithm's computation time estimation performance to a five-wavenumber scheme for the low contrast model (Test 1). Comparison is made between the computation times of a direct solver and a preconditioned BICGSTAB. When considering an iterative solver, it is found that the suggested scheme costs roughly sixteen times as much as a five-wavenumber scheme. The suggested scheme takes fifty-five times longer for a direct solver. If wavenumbers on the order of hundreds are required for complex models, it would prove to be effective nonetheless. The numerical experiments clearly illustrate the versatility of the developed algorithm for various complex geological models.

Chapter 4

DC Resistivity data sensitivity to subsurface anisotropic parameters

4.1 Abstract

This study investigates the sensitivity of DC resistivity data to the anisotropic parameters of the subsurface. For the analysis, the azimuthal apparent resistivity curves are simulated and analyzed for various anisotropic models. For sensitivity experiments, numerical derivatives of apparent resistivity data with respect to parameters determining anisotropy for the 2D cases are calculated for data simulated along a profile. The outcomes show that the data is commonly sensitive to all four parameters except for the model with circular azimuthal apparent resistivity, where the sensitivity to principal resistivity along the profile direction vanishes.

4.2 Introduction

The direct current (DC) approach is an economically viable method for near subsurface mapping. However, successfully applying the DC resistivity technique requires data analysis to consider the complete physics of the DC resistivity modeling. One crucial characteristic of the resistivity of subsurface rock is the electrical anisotropy. It depicts a phenomenon of directional dependency of current flow in a piece of homogeneous rock. Materials with a characteristic lineation or platey fabric, such as clay, slate, and shale, frequently exhibit this directional dependence. It leads to the property known as intrinsic anisotropy or micro anisotropy and is contingent upon the material's texture or crystal symmetry [45]. The origin of anisotropy can be attributed to many factors, like

preferentially oriented fracture systems [22]. Studies suggest that limestone structures can develop anisotropy up to a factor of 4.5 [103]. If these anisotropic structures are considered isotropic, it can lead to inaccurate interpretation [6, 165]. To examine the subsurface's anisotropic characteristics, the utilization of several azimuthal electrode arrays were suggested [142, 153]. For accuracy benchmarking, [82] provided analytical solutions for several straightforward anisotropic models. [83, 150] investigated anisotropy's impact on multilayer structures.

The anisotropy paradox is a widely studied phenomenon as it provide an insight into behavior of DC resistivity data in the presence of anisotropic subsurface. Numerical simulations have also confirmed it [152]. [92] used Coulomb's law in anisotropic media to demonstrate the presence of this phenomenon and used surface surveys and electric logging to explain this seemingly paradoxical behavior. The anisotropy paradox stands true for borehole measurements as well, and [94] demonstrated that any vertically aligned electric measurement in a horizontally oriented lamination would only be sensitive to the horizontal conductivity and totally blind to the vertical conductivity. A surface survey does not measure the horizontal conductivity on its own; it will only gauge the geometric mean of the horizontal and vertical conductivity [92]. The polar representation [165] of apparent resistivity is often used to illustrate the anisotropy paradox. [87, 116] analyzed the polar diagrams by interpreting the anisotropy paradox for horizontal transverse isotropic (HTI) media. The apparent resistivity polar plots suggest that the case where circular plots are obtained, cannot resolve the vertical resistivity component. [161] examined anisotropy employing polar diagrams for generalized anisotropy. Most of these studies have commented on the insensitivity of DC resistivity data to anisotropic subsurface parameters. However, they did not investigate the sensitivity plots in their studies. Therefore, a more rigorous analysis of the sensitivity of DC resistivity data to subsurface anisotropic parameters is required. Thus, the present study examines it in detail.

In this chapter, we present an exhaustive analysis of the polar diagram for various cases of subsurface anisotropy using the 2D models. Subsequently, the sensitivity of DC resistivity data to the anisotropic parameters is discussed utilizing the knowledge gained from polar diagram analysis.

4.3 Subsurface anisotropy and DC resistivity data

This section examines the azimuthal characteristics of DC resistivity data for the anisotropic subsurface. It must be stressed that the analysis in this study is limited to 2D TTI media where the subsurface conductivity maximally depends on four parameters, namely three

principal conductivities and an angle of symmetry axis. The subsurface model used for this experiment consists of an isotropic layer of 5 m thickness having a resistivity of $10\,\Omega m$ overlaying on an anisotropic half-space. For various scenarios of the second layer resistivity, the apparent resistivity curves at radial distances of 5 m, 10 m, 25 m, 50 m, 75 m, 100 m, 140 m, and 160 m from the source (for brevity, referred as radial distances hereafter) for 360 degrees of azimuthal angles are computed and analyzed. For conciseness, these plots are referred to as azimuthal curves henceforth. We have used the space domain DC resistivity algorithm discussed in the previous chapter to calculate the response of all the experiments. For the first model, the lower half-space is taken isotropic media of resistivity $100\,\Omega m$ as shown in Fig. 4.1 and the azimuthal curves are shown in Fig. 4.2. The azimuthal curves are concentric circles with increasing radii with radial distance. It happens because both the layers are isotropic, and the resistivity of the lower layer is higher. The radius of azimuthal curves shows very little change beyond radial distances of 140 m, which indicates that beyond this distance, we can assume that the response of the lower half-space media dominates over the first layer. Therefore, the maximum distance is considered as 160 m, for this experiment, so that the response is overwhelmed by the lower half-space. However, it needs to be stressed that the distance beyond which the lower half-space dominates the response also depends on the conductivity of the upper and lower layers. These results are expected; nevertheless, this experiment's results serve the purpose of a reference that we will use for comparing the anisotropic cases.

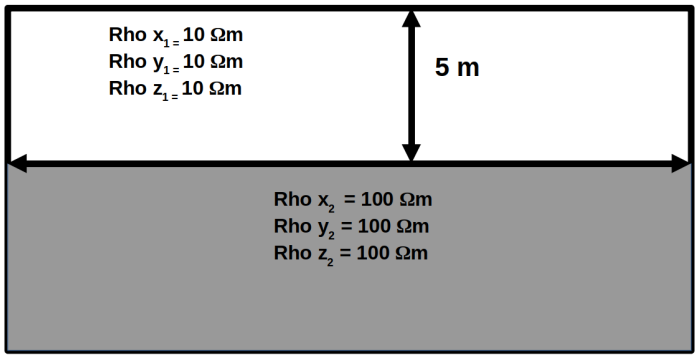

Fig. 4.1 Two layer isotropic model with resistivity of first layer as $10\,\Omega m$ and resistivity of second layer as $100\,\Omega m$. The thickness of first layer is 5 m. Rho x, Rho y and Rho z in the figure denote the values of resistivity in the principal directions x, y and z respectively.

In the second experiment, the top layer is an isotropic layer with resistivity of $10\,\Omega m$, whereas the lower half-space is taken as triaxial anisotropic media with resistivities in x-, y- and z-directions as 100 Ωm, 50 Ωm, and 25 Ωm, respectively, and the model is illustrated in Fig. 4.3. The associated azimuthal curves are shown in Fig. 4.4. For smaller

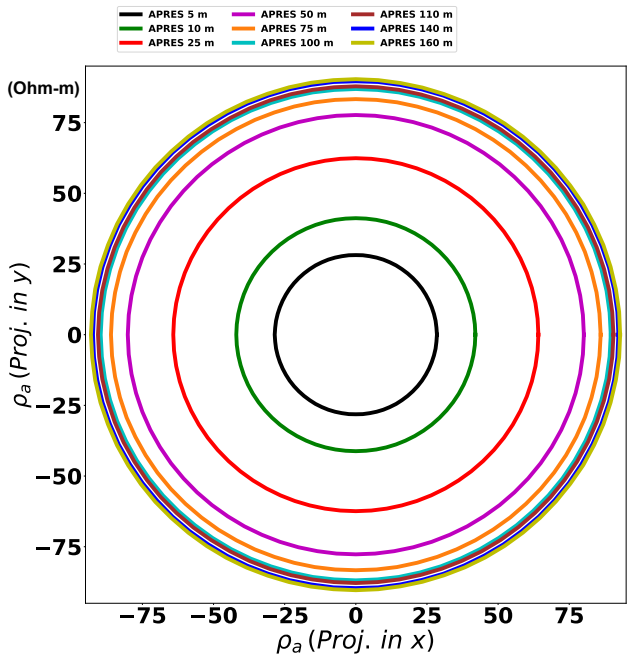

Fig. 4.2 Azimuthal apparent resistivity curves obtained at varying radial distances from the source for the isotropic model shown in Fig. 4.1. The 'APRES' in the plot is used to denote apparent resistivity curves at the given radial distances.

radial distances, the curves are concentric circles of increasing radius with radial distance; however, for large radial distances, the circles are deformed to ellipses with the minor and major axes in the x- and y-direction, respectively. The behavior of having a large apparent resistivity value along the direction of the principal axis of lower resistivity is known and is referred to as the so-called anisotropy paradox [92, 141]. The apparent resistivity at 5 m and 160 m radial distances are around 20 Ωm and 45 Ωm, respectively. Since the resistivity of the first layer is 10 Ωm, the response at 5 m is also influenced by the second layer. However, the azimuthal curve for 5 m is circular. To examine it further, the variations in the aspect ratio (resistivity in the y-direction/resistivity in the x-direction) with apparent resistivity along the y-direction for all the radial distances are illustrated in Fig. 4.5. It displays that the circular nature remains until the apparent resistivity falls below $\approx 30\ \Omega m$, revealing that the azimuthal curves retain the isotropic character of the upper layer even though the significant current passes through lower anisotropic media as the apparent resistivity are considerably higher than resistivity of first layer. Furthermore, beyond the 50 m radial distance, the changes in the apparent resistivity value are not substantial, as seen from Fig. 4.4, indicating the dominant current flow is mostly in the lower layer. However, the elliptic nature of azimuthal curves becomes more dominant

after this distance. Therefore, this experiment indicates that if the top layer is isotropic, the azimuthal variation in apparent resistivity is first controlled by the top layer till some distance even though the significant current may be flowing through lower anisotropic media at the distance. The elliptic nature of azimuthal apparent resistivity predominantly occurs beyond this distance.

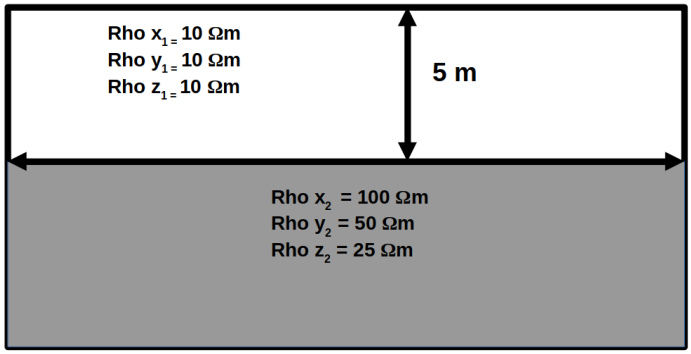

Fig. 4.3 Tri-axial anisotropic model with first layer isotropic having resistivity value of $10\,\Omega m$ and thickness 5 m. The second layer is a half-space with tri-axial anisotropy bearing resistivity values of $100\,\Omega m$, $50\,\Omega m$, and $25\,\Omega m$ in the x, y and z-directions respectively.

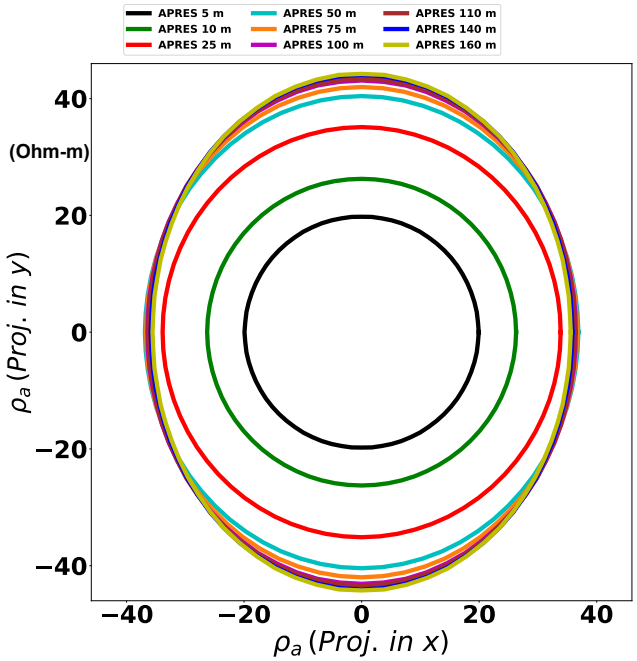

Fig. 4.4 Azimuthal apparent resistivity curves for the tri-axial anisotropy model that is shown in Fig. 4.3. The apparent resistivity curves are obtained at varying radial distances from the source. The APRES used in the legends denote apparent resistivity.

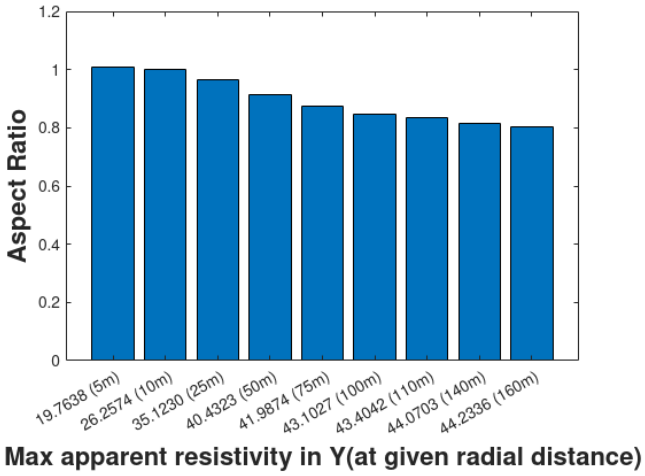

Fig. 4.5 The figure shows the plot of the aspect ratio (resistivity in the y-direction/resistivity in the x-direction) vs resistivity in the y-direction (with increasing radial distance). The numbers in brackets on x-aixs indicate the values taken at increasing radial distance from the source.

For the next experiment, the triaxial anisotropic model used in the above experiment is modified into various tilted transverse isotropic (TTI) models by varying the dip angle of the anisotropy axis. The test are conducted for 0^o (tri-axial anisotropic case), 22.5^o, 45^o, 62.5^o and 90^o dip angles. The azimuthal curves at 160 m radial distance for all five cases are shown in Fig. 4.6. It is observed for the azimuthal curves that as we move from the 0^o to 90^o, the ellipse changes its major axis from the y-direction to the x-direction. Furthermore, it becomes closer to circle around 45^o, indicating an isotropic subsurface-like character. Therefore, we further analyze the behaviors of azimuthal curves for a TTI lower half-space with a 45^o dip angle at different radial distances, and the simulated azimuthal curves for varying radial distances from 5 m to 160 m are shown in Fig. 4.7. The curves at larger radial distances show an elliptic character with the major axis in the y-direction; however, the deviation from the circular nature is very mild. A case in which the curve turns to a circular nature has very significant consequences in the sensitivity of subsurface anisotropy to surface DC resistivity data. Furthermore, the 45^o is, indeed, not a case of a perfect circle or a case of lacking anisotropic character.

To invistigate it further, we experimented with three more cases by varying the resistivity component, ρ_{xx}, of lower half-space as 35 Ωm, 65 Ωm, and 75 Ωm, while keeping other resistivity components (ρ_{yy} and ρ_{zz}) the same. The azimuthal apparent resistivity curves are also simulated for these three models. The ratio of apparent resistivities along the x- and y-direction is plotted for various dip angles of the symmetric axis of anisotropy to investigate the impact of subsurface resistivity on the dip angle. The plots are shown

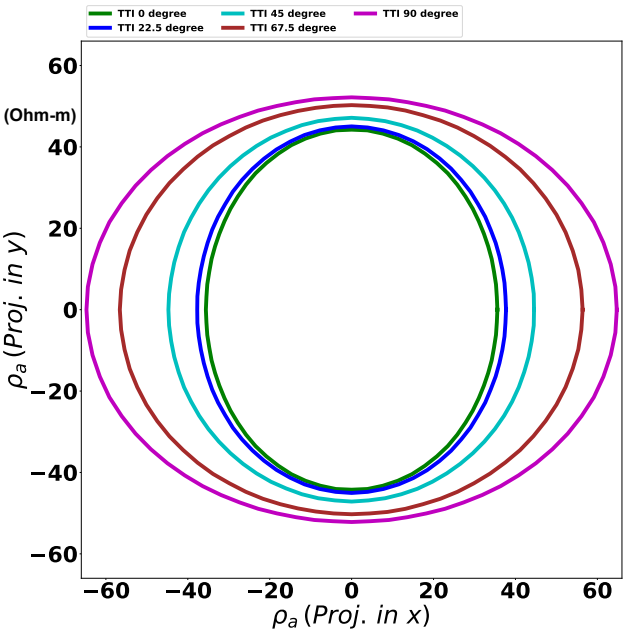

Fig. 4.6 The figure shows the plot for azimuthal apparent resistivity curves obtained for different cases of tri-aixal anisotropic model with varying dip angles (TTI 0^o, TTI 22.5^o, TTI 45^o, TTI 67.5^o, and TTI 90^o. All the curves are obtained at a fixed radial distance of 160 m.

in Fig. 4.8. It is revealed by the plots that for ρ_{xx} = 100 Ωm, the dip angle at which the azimuthal curve will become circular is between 45^o and 67.5^o as the azimuthal curve has a major axis in y-direction at 45^o and at 67.5^o the major axis is in the x-direction. For ρ_{xx} = 75 Ωm, the azimuthal curve is almost circular at 45^o, whereas, for ρ_{xx} = 65 Ωm, the circular nature is likely to be between 22.5^o and 45^o dip angle as the curve cross the aspect ratio equal to one between these angles. Furthermore, in the case of ρ_{xx} = 35 Ωm, the aspect ratio curve remains above one, and it is expected as both ρ_{xx} and ρ_{zz} are less than ρ_{yy}. Consequently, this experiment reveals that the dip angle at which the azimuthal apparent resistivity begins behaving like an isotropic case depends on the resistivity of the subsurface. In case the principal resistivities that belong to the vertical plane below profile (denoted by ρ_{xx} and ρ_{zz} in this study) are both smaller than the resistivity perpendicular to the plane (represented by ρ_{yy} in this study), the DC resistivity measurement shows the sensitivity to subsurface anisotropy. However, in case ρ_{yy} is between the ρ_{xx} and ρ_{zz}, around some angle the surface DC resistivity data may not be sensitive to the subsurface anisotropy. The present experiment suggests that if the $\rho_{xx} - \rho_{yy} > \rho_{yy} - \rho_{zz}$, the angle where the azimuthal curve becomes circular will be above 45^o and for $\rho_{xx} - \rho_{yy} < \rho_{yy} - \rho_{zz}$

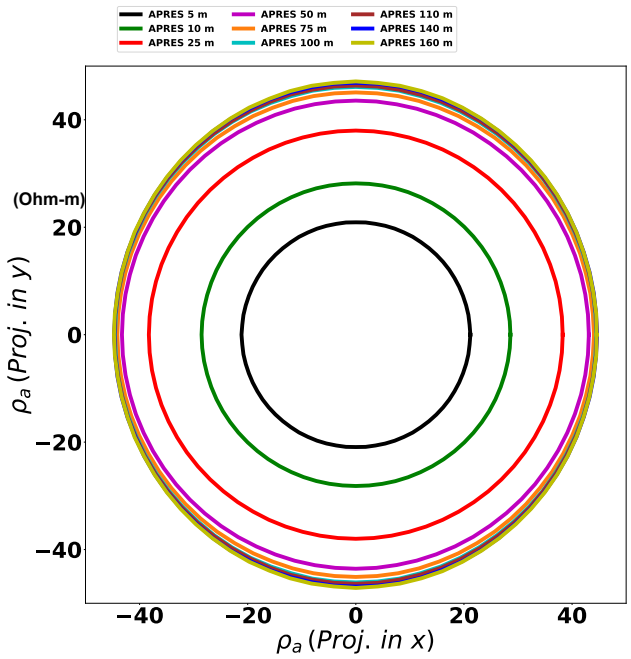

Fig. 4.7 Azimuthal apparent resistivity curves for the case of tri-axial anisotropic model with dip angle 45^o (TTI 45^o case), obtained at increasing radial distances from 5 m to 160 m.

it will be below 45^o. For $\rho_{xx} - \rho_{yy} \approx \rho_{yy} - \rho_{zz}$ the circular character is attained around 45^o. The present experiment was repeated for resistive overburden as appose to the present case of conductive overburden. Since, the current prefers least resisitve path, some modifications are made by taking the thickness of first layer as 30 m for resistive overburden. However, the conclusion remains the same, therefore, the results for these experiments are given as supplementary (see Appendix B). The present experiment exhibited that the azimuthal curves show isotropic character in a particular case of anisotropy; therefore, it is instructive to test whether surface data will be sensitive to the element of conductivity tensor or not.

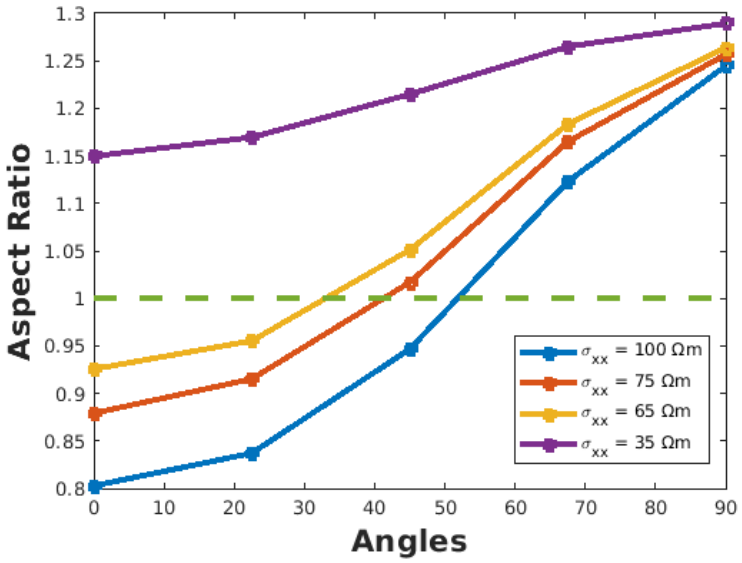

Fig. 4.8 The figure shows the plot of aspect ratio vs angles of different TTI models used (TTI 0^o, TTI 22.5^o. TTI 45^o, TTI 67.5^o, TTI 90^o). The plots are obtained at a fixed radial distance of 160 m for different models bearing the principal resistivity value ($\sigma_{xx} = 100\,\Omega m, 75\,\Omega m, 65\,\Omega m, 35\,\Omega m$) for the second layer.

4.4 Sensitivity Analysis

For any geophysical method to estimate the subsurface property, it is a prerequisite that the data be adequately sensitive to those parameters, and the sensitivity should be higher than the noise floor in typical field data of the method. The data may be sensitive to some of the parameters, like some elements of a conductivity tensor. Consequently, maximally, the inverse modeling can recover only sensitive parameters. Therefore, knowing the parameters that are insensitive to particular data is crucial to avoid over-interpreting the estimated inverse models. This study examines the sensitivity of conductivity tensor elements to DC resistivity data. The conductivity tensor depends on four parameters at most, since we are studying the 2D case. Furthermore, the 2D case implies the data that is being analyzed is recorded along a profile. Therefore, we have simulated the data along the profile oriented in x-direction. For this experiment, a two-layer model consisting of the top isotropic layer of 30 m thickness having 100 Ωm resistivity is taken. For the second layer, different cases are examined as TTI medium with principal resistivities as 10 Ωm, 5 Ωm, and 2.5 Ωm in x, y and z-directions, respectively, for varying angles of symmetry axis. A simple two-layer model is utilized to minimize the impact of the size and geometry of the body being investigated. Therefore, the observations from this analysis are more generic, and the effect of the resolution of the DC method, size, geometry, and depth of

the anomaly are not commented on in this investigation. To estimate the sensitivity, the derivative of apparent resistivity with respect to the principal resistivities for the constant angle of the symmetry axis of the second layer is computed numerically using a difference formula. It can be mathematically expressed as,

$$\frac{\partial \rho_a}{\partial m} = \frac{\partial \rho_a(m+\delta m) - \partial \rho_a(m)}{\delta m}, \tag{4.1}$$

where ρ_a is the apparent resistivity and m (=ρ_{xx}, ρ_{yy}, ρ_{zz}) corresponds to the model parameters. We perturb the m by 5% to compute the derivative. The reference model (depicting the value of the parameter, m) and the perturbed model for all three resistivity elements (representing the value of the parameter, $m+\delta m$) are shown in Fig. 4.9. We use the pole-pole array for this experiment. The sensitivity plots for ρ_{xx}, ρ_{yy}, and ρ_{zz} up to 300 m distance from the source are shown in Fig. 4.10. Since the resistivity of the first layer is invariant in this experiment, the sensitivity for small distances are minimal for all three parameters. The sensitivity of apparent resistivity to ρ_{xx} is smaller than other parameters and increases with distance. It aligns with the anisotropy paradox as the profile is in the x-direction. However, the sensitivity values are of the same order as the other two parameters, indicating that the data also senses the ρ_{xx}, even though the sensitivity to ρ_{yy} and ρ_{zz} parameters being more. The sensitivity of ρ_{yy} increases with distance, and at 300 m, it is approximately equivalent to the sensitivity of ρ_{zz}. The sensitivity of ρ_{zz} first increases rapidly till around 50 m and then fluctuates around 0.75. It is to be noted that the first layer influences sensitivity at near offset. Thus, the sensitivity of ρ_{zz} indicates a somewhat constant value with distance. In summary, the experiment shows that all three parameters show the sensitivity to data simulated along a profile. However, they differ in magnitude and trends, making the profile length a factor as well.

For the second experiment, the resistivity of the tri-axial anisotropic lower half-space used in the first experiment is rotated by 22.5^o to construct a TTI model. For simulation of the response of the perturbed model, the perturbation is done in principal resistivity values of the tri-axial model and is rotated by 22.5^o subsequently. The sensitivity plots for this experiment are shown in Fig. 4.11. Again, the behavior and magnitude of sensitivity values are similar to the tri-axial case with a change that the sensitivity of ρ_{zz} now shows an increasing trend with distance. Therefore, for a TTI model, all three principle resistivities show sensitivity to surface DC observations, and therefore, these parameters are likely to be estimated using such data.

The third experiment is similar to the second experiment with a modification that the resistivity of the lower half-space of the tri-axial anisotropic is rotated by 45^o. The sensitivity plots for this experiment are shown in Fig. 4.12. The behavior and magnitude

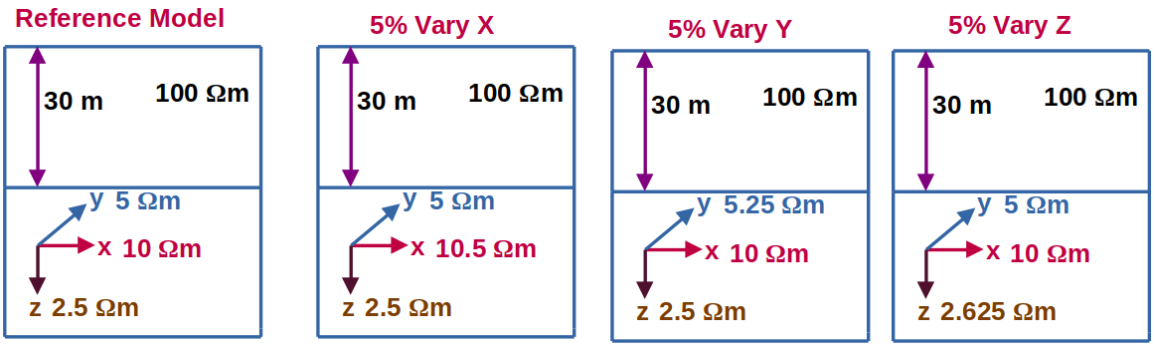

Fig. 4.9 The figure shows the models used for sensitivity analysis. On the extreme left reference model is shown. Further the perturbed models are shown by varying the resistivity values by 5 % for x, y and z-directions respectively in the second layer. The above case is shown for TTI 0^o (tri-axial anisotropic model). However we also perform the sensitivity analysis for TTI 22.5^o, TTI 45^o, TTI 67.5^o, and TTI 90^o. For all the cases the perturbation factor is kept constant at 5 %.

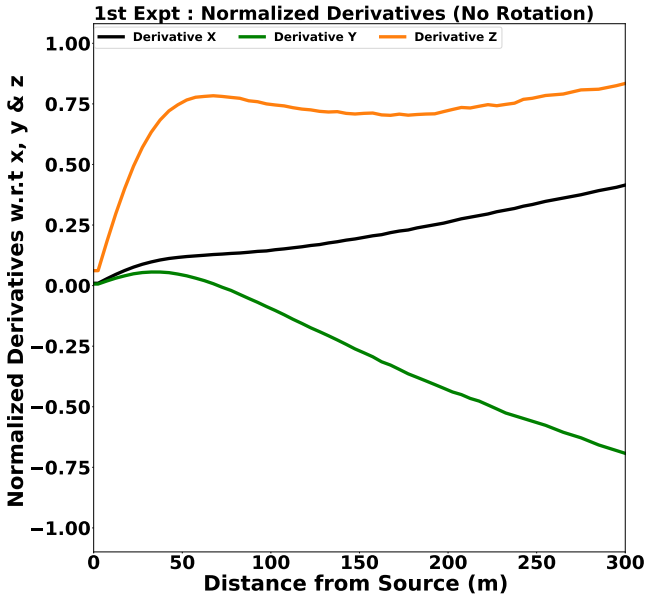

Fig. 4.10 Sensitivity curves of simulated DC resistivity data along x-direction with respect to the three principal resistivities ($\rho_{xx}, \rho_{yy}, \rho_{zz}$) for the reference and perturbed models shown in Fig. 4.9.

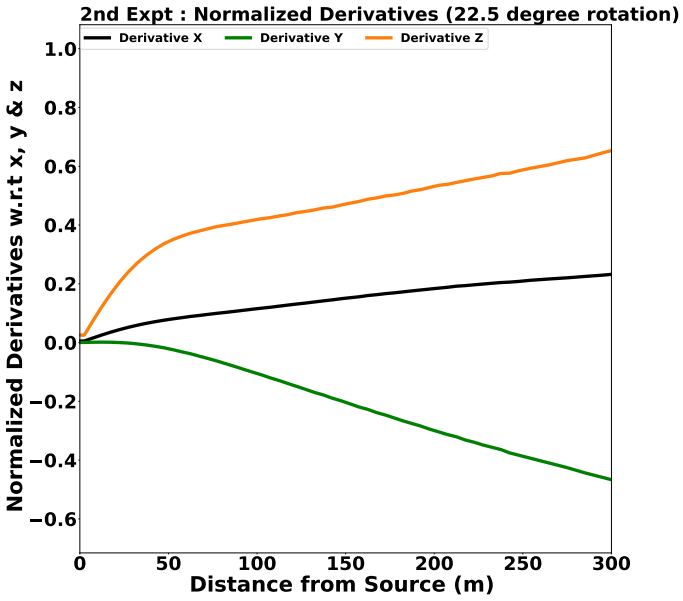

Fig. 4.11 Sensitivity curves of simulated DC resistivity data along x-direction with respect to the three principal resistivities ($\rho_{xx}, \rho_{yy}, \rho_{zz}$) for the reference and perturbed models obtained after the rotation of principal symmetry axis by 22.5^o.

of sensitivity values are similar to the 22.5^o case; however, if we compare the previous and this experiment results, the most significant change is in the reduction in sensitivity of simulated data to ρ_{xx} compared to other two parameters. The next experiment is done with 67.5^o rotation of the symmetry axis. The sensitivity plots for this experiment are given in Fig. 4.13. It indicates the sensitivity of simulated data to the ρ_{xx} is almost vanishing compared to the other previous experiment. However, the sensitivity to the other two parameters has changed significantly less. In the last experiment, the rotation of the symmetry axis is performed using 90^o, and the sensitivity plots for this experiment are given in Fig. 4.14. It shows more sensitivity to ρ_{xx} than 67.5^o. Following our discussion in the previous section, we expect the circular nature of this model to be between 45^o and 67.5^o angles. Therefore, we can argue that when the azimuthal curves for a TTI model turn circular like, as in the case of the isotropic models, the sensitivity of DC resistivity data observed at the surface to the principle resistivity in the direction of the profile vanishes. However, the data still have significant constraints on the other two principal resistivities. Therefore, only two resistivity parameters can be estimated by the observed data in such scenarios. It needs to be stressed that it happens for a particular combination of relative

values of principle resistive values relative to each around a specific angle of the symmetry axis.

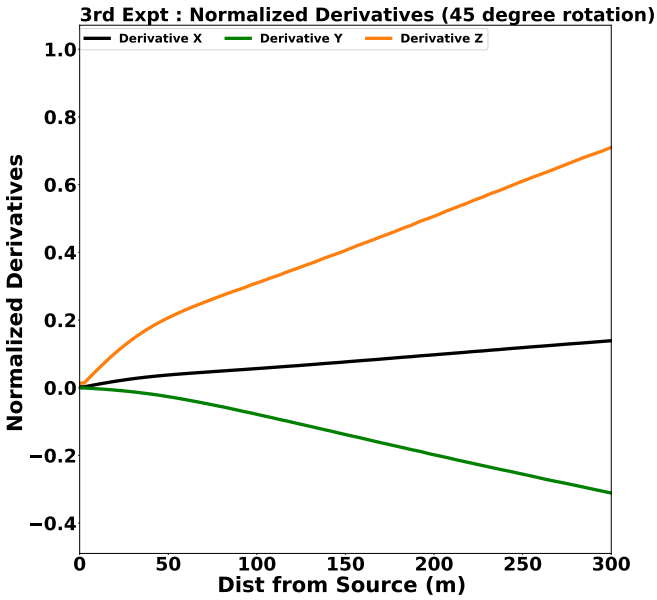

Fig. 4.12 Sensitivity curves of simulated DC resistivity data along x-direction with respect to the three principal resistivities ($\rho_{xx}, \rho_{yy}, \rho_{zz}$) for the reference and perturbed models obtained after the rotation of principal symmetry axis by 45^o.

We have also analyzed the sensitivity of simulated DC resistivity data to the angle of the symmetry axis. For this experiment, the numerical derivative of apparent resistivity concerning the angle of the symmetry axis is computed by perturbing the angle by 5^o. The perturbation by 5^o may not be a reasonable choice around those angle values where the sensitivity changes too sharply with the angle. The sensitivity data are simulated for angles from 2.5^o to 87.5^0 with a 5^o interval, and the experiment results are shown in Fig. 4.15. In general, the sensitivity to near offset is small because the first layer is not perturbed. The plot shows varying sensitivity for different values of angles. However, the sensitivity in the mid-offset ranges is relatively low for an angle around 50^o except for other angles. It shows a correlation to low sensitivity where the azimuthal curves represent an isotropic-like nature.

This study suggests that DC resistivity data insensitivity generally occurs to the principal resistivity in the direction of the profile at the particular tilt angle of resistivity for the TTI case with distinct principal resistivities. If both the principal resistivities in the plane below the profile are smaller than the principal resistivity perpendicular to the profile, the

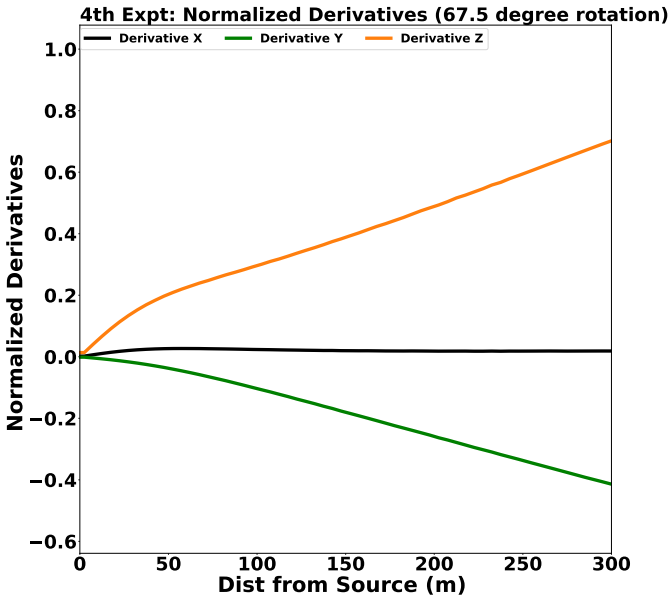

Fig. 4.13 Sensitivity curves of simulated DC resistivity data along x-direction with respect to the three principal resistivities ($\rho_{xx}, \rho_{yy}, \rho_{zz}$) for the reference and perturbed models obtained after the rotation of principal symmetry axis by 67.5^o.

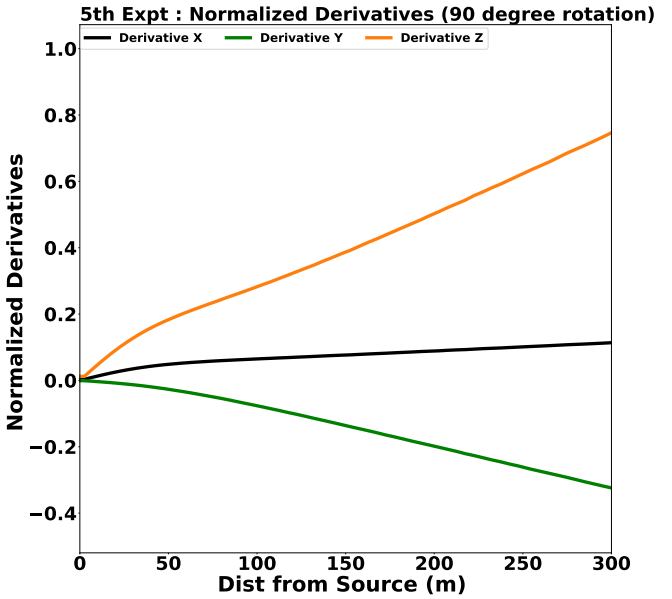

Fig. 4.14 Sensitivity curves of simulated DC resistivity data along x-direction with respect to the three principal resistivities ($\rho_{xx}, \rho_{yy}, \rho_{zz}$) for the reference and perturbed models obtained after the rotation of principal symmetry axis by 90^o.

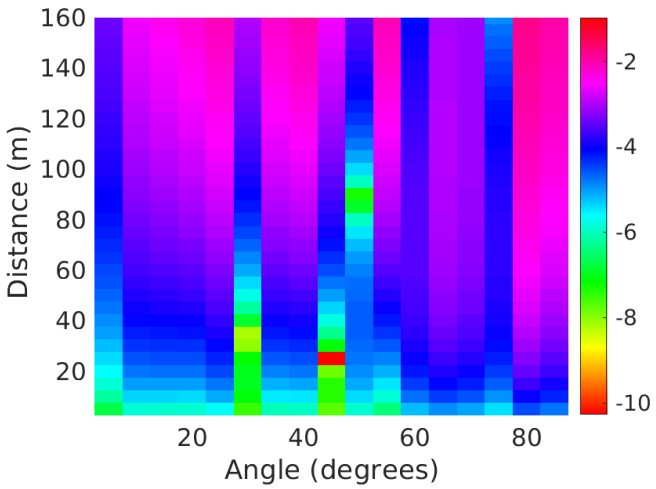

Fig. 4.15 Sensitivity of apparent resistivity data perpendicular to strike direction (along x-direction) with dip angle for reference model shown in Fig. 4.9.

data appears sensitive to all the principal resistivities. Earlier studies have suggested that in the case of HTI media, the vertical resistivity is insensitive to the DC resistivity data. In a nutshell, this discussion indicates that which parameter of the anisotropic will be sensitive (or not) depends on relative values and the tilt of the principal resistivities. Since estimating these subsurface parameters is an objective of the DC resistivity survey, it is like a chicken and egg problem. Nonetheless, this study provides valuable information about the sensitivity of DC resistivity data to the parameters that describe the anisotropy of the subsurface. Even though the experiment is limited to the 2D TTI subsurface, these primarily apply to the DC data recorded along a profile over a predominantly 2D subsurface resistivity distribution. However, an investigation of general anisotropy for 3D model can be performed in the future.

4.5 Conclusion

We have analyzed the sensitivity of DC resistivity data to the anisotropic parameters of the subsurface for a 2D model with a titled symmetry axis of anisotropy. For this case, there can be a maximum of four parameters for specifying the anisotropy: three principal resistivity values and one angle defining the angle of the tilted symmetry of anisotropy. First, the azimuthal apparent resistivity plots for different models with various radial distances from the source and the tilt angle are analyzed. The investigation revealed that the azimuthal apparent resistivity plots are generally elliptic; however, they turn circular at a particular angle, which depends on the relative principle resistivity values. To investigate

whether the DC data shows the sensitivity to all four anisotropic parameters, sensitivity experiments are conducted by calculating the derivatives of modeled data with respect to all four parameters. The results indicate that the data generally shows sensitivity to all four parameters. However, around the point where the azimuthal apparent resistivity plots are circular, the sensitivity to principal resistivity along the profile vanishes. These experiments give some insights into the anisotropic parameter that can be recovered using DC resistivity data; however, the analysis did not consider the size, geometry, and depth of the anomaly into account.

Chapter 5

Conclusion and future possibilities

This thesis aimed to develop a forward modeling algorithm for the 2D DC resistivity problem. The study seeks to address the issues that occur while dealing with real-world imaging problems, such as topography and arbitrary anisotropy, often encountered as inevitable in practical scenarios. Literature study suggests that the mimetic finite difference method is suitable to handle such complexities as it can work with highly distorted, non-orthogonal, rough grids, leading to a versatile algorithm. The first part of the research focuses on the development of a 2D DC resistivity forward modeling algorithm using the mimetic finite difference method. The accuracy of the developed algorithm is demonstrated using dyke model and two-layered anisotropic models utilizing analytical solutions. The algorithm provides accurate solutions even in high conductivity contrasts, proving its strength. To further test the accuracy of the scheme for the topography case, we compared it with published results in the literature because of the unavailability of the analytical solutions. The obtained results show a good match, illustrating that the algorithm is capable of working with complex topography. Furthermore, numerical tests are performed with distorted grids with varying levels of distortion to test the stability of the algorithm. The results show that the algorithm produces accurate results even in the case of highly distorted, non-orthogonal grids, highlighting the developed algorithm's resilience. To understand the computational aspects of the modelling the convergence behavior of the BICGSTAB method is also analysed. It is noted that while the convergence for orthogonal grids is generally smooth, the convergence for highly distorted grids exhibits a non-smooth behaviour. Both, though, require about the same amount of iterations. As a result, in terms of grid distortions, the MFDM technique is both stable and effective. Other models undergo the same analysis, and similar trends are discovered. Hence, the developed 2D DC resistivity forward modeling scheme is accurate, robust, and stable to work with complex topography and anisotropy involving distorted, non-orthogonal grids.

The DC resistivity source exhibits a 3D character, leading to the variation in potential in all three directions, even in the case of a 2D model. Therefore, a wavenumber domain modeling strategy is adopted for efficient computations. However, an analysis of space domain responses calculated using various wavenumber schemes reported in the literature is found to be erroneous at large current-potential electrode spacing, even for the half-space model. An accurate simulation for large electrode spacing requires several wavenumber simulations, making the wavenumber domain approach expensive. Consequently, the present study develops an efficient and versatile 2D DC resistivity algorithm in space domain. A novel boundary condition is devised, utilizing the symmetric nature of potential about the vertical plane that passes through the source position. The numerical scheme is extensively tested and benchmarked for isotropic and anisotropic models, including very high conductivity contrast cases utilizing analytical solutions. The simulated solutions show an excellent match-up to very long electrode spacing. The numerical results for a 2D block model and a variable topography having tilted transversely isotropic subsurface are also discussed to demonstrate the versatility of the developed algorithm. We also present the performance of the proposed algorithm for computation time estimation in comparison with a five-wavenumber scheme for a low contrast model. We compare the computation times of a direct solver and a preconditioned BICGSTAB. In the case of an iterative solver, it is found that the proposed scheme is about 16 times more expensive than a five-wavenumber scheme. The suggested scheme needs 55 times more time for a direct solver. In the case of complex models, it would prove to be efficient if wavenumbers on the order of hundreds were required.

Geophysical investigations aim to estimate subsurface properties; therefore, it is essential to examine the sensitivity of geophysical data to subsurface parameters. Thus, the present study explores the sensitivity of subsurface electrical anisotropy parameters to DC resistivity data. The azimuthal apparent resistivity curves are simulated for two-layered models including isotropic, tri-axial anisotropic, and tilted transversely isotropic models with different tilt angles of the symmetry axis. For all anisotropic cases, the curves are mostly found to be elliptic, except for a few combinations of principal resistivity values around a particular tilt angle of the symmetry axis where the curves turn out to be circular. These patterns inspire us to perform a sensitivity study of the 2D DC resistivity data with respect to model parameters as three principal resistivities and tilt angle of the anisotropy symmetry axis. It is found that the 2D DC resistivity data is sensitive to all the four anisotropic parameters mentioned above, except for the case where the azimuthal apparent resistivity curves turn out to be circular where the sensitivity to the principal resistivity along the profile direction vanishes.

As a future work, the developed forward modeling algorithm can be extended to a 2D DC resistivity inversion algorithm for deterministic and/or stochastic algorithms. Since the forward modeling part can handle anisotropy and complex topography, it becomes a suitable candidate for the inversion of DC resistivity data where complex topography and anisotropic character are present in the subsurface. The applicability of the mimetic finite difference method in a trans-dimensional Bayesian inversion workflow is also a valuable aspect. The finite-difference method has an issue with the trans-dimensional Bayesian scheme because the cell nodes' locations are randomly disrupted in space during optimization. It is difficult for the conventional finite-difference methods to handle such random perturbations. Although finite-element methods are versatile to handle random grids, but they are more sensitive to grid coarsening/refinement than the finite-difference approach. Additionally, the trans-dimensional Bayesian approach needs hundreds of thousands of iterations to compute the responses of models that are randomly perturbed. As a result, the mesh regeneration becomes necessary. And the finite element methods' sensitivity to grid refinement may pose a challenging issue. Consequently, the mimetic finite difference method is a viable option because of its capacity to handle non-orthogonal grids and comparatively lower sensitivity to grid refining. Hence, the developed algorithm can be a good choice for developing a 2D DC resistivity inversion algorithm. Likewise, 3D modeling and inversion using the mimetic finite difference method is another area of future extension of the present work.

References

[1] Abidin, M. H. Z., Saad, R., Ahmad, F., Wijeyesekera, D. C., and Baharuddin, M. F. T. (2011). Application of geophysical methods in civil engineering. In *Malaysian Technical Universities International Conference on Engineering and Technology*.

[2] Aizebeokhai, A. P. (2010). 2d and 3d geoelectrical resistivity imaging: Theory and field design. *Scientific Research and Essays*, 5(23):3592–3605.

[3] Aly, S. A., Farag, K. S., Atya, M. A., and Badr, M. A. (2018). Use of electromagnetic–terrain conductivity and dc–resistivity profiling techniques for bedrock characterization at the 15th-of-may city extension, cairo, egypt. *NRIAG Journal of Astronomy and Geophysics*, 7(1):107–122.

[4] Apparao, A. and Sarma, V. (1983). The modified pseudo-depth section as a tool in resistivity and IP prospecting—a case history. *Pure and applied geophysics*, 121:91–108.

[5] Aristodemou, E. and Thomas-Betts, A. (2000). DC resistivity and induced polarisation investigations at a waste disposal site and its environments. *Journal of Applied Geophysics*, 44(2-3):275–302.

[6] Asten, M. (1974). The influence of electrical anisotropy on *mise a la masse* surveys. *Geophysical Prospecting*, 22(2):238–245.

[7] Baba, K. and Seama, N. (2002). A new technique for the incorporation of seafloor topography in electromagnetic modelling. *Geophysical Journal International*, 150(2):392–402.

[8] Batayneh, A. T. (2001). Resistivity imaging for near-surface resistive dyke using two-dimensional DC resistivity techniques. *Journal of Applied Geophysics*, 48(1):25–32.

[9] Bayrak, M. and Şenel, L. (2012). Two-dimensional resistivity imaging in the kestelek boron area by VLF and DC resistivity methods. *Journal of Applied Geophysics*, 82:1–10.

[10] Benson, A. K., Payne, K. L., and Stubben, M. A. (1997). Mapping groundwater contamination using dc resistivity and VLF geophysical methods; a case study. *Geophysics*, 62(1):80–86.

[11] Berkopec, A. (2010). Analytical solution for DC field, transparency condition, and estimation of resistivity for radially anisotropic sphere of conductivity r^m. *Journal of Electrostatics*, 68(1):85–90.

[12] Bhattacharya, B. and Sen, M. (1981). Depth of investigation of collinear electrode arrays over homogeneous anisotropic half-space in direct current methods. *Geophysics*, 46(5):768–780.

[13] Bhattacharya, P. (1968). Direct current geoelectric sounding: Principles and interpretation. pages 1–135.

[14] Bibby, H. (1978). Direct current resistivity modeling for axially symmetric bodies using the finite element method. *Geophysics*, 43(3):550–562.

[15] Bing, Z. and Greenhalgh, S. (2001). Finite element three dimensional direct current resistivity modelling: accuracy and efficiency considerations. *Geophysical Journal International*, 145(3):679–688.

[16] Blome, M., Maurer, H., and Schmidt, K. (2009). Advances in three-dimensional geoelectric forward solver techniques. *Geophysical Journal International*, 176(3):740–752.

[17] Bochev, P. B. and Hyman, J. M. (2006). Principles of mimetic discretizations of differential operators. In *Compatible spatial discretizations*, pages 89–119. Springer.

[18] Boonchaisuk, S., Vachiratienchai, C., and Siripunvaraporn, W. (2008). Two-dimensional direct current (DC) resistivity inversion: Data space occam's approach. *Physics of the Earth and Planetary Interiors*, 168(3-4):204–211.

[19] Boulanger, O. and Chouteau, M. (2005). 3d modelling and sensitivity in DC resistivity using charge density. *Geophysical Prospecting*, 53(4):579–617.

[20] Braga, A. C. d. O., Malagutti Filho, W., and Dourado, J. C. (2006). Resistivity (DC) method applied to aquifer protection studies. *Revista Brasileira de Geofísica*, 24:573–581.

[21] Brezzi, F., Lipnikov, K., and Simoncini, V. (2005). A family of mimetic finite difference methods on polygonal and polyhedral meshes. *Mathematical Models and Methods in Applied Sciences*, 15(10):1533–1551.

[22] Busby, J. (2000). The effectiveness of azimuthal apparent-resistivity measurements as a method for determining fracture strike orientations. *Geophysical prospecting*, 48(4):677–695.

[23] Candansayar, M. E. and Tezkan, B. (2008). Two-dimensional joint inversion of radiomagnetotelluric and direct current resistivity data. *Geophysical Prospecting*, 56(5):737–749.

[24] Caramana, E., Burton, D., Shashkov, M. J., and Whalen, P. (1998). The construction of compatible hydrodynamics algorithms utilizing conservation of total energy. *Journal of Computational Physics*, 146(1):227–262.

[25] Cardarelli, E. and Fischanger, F. (2006). 2D data modelling by electrical resistivity tomography for complex subsurface geology. *Geophysical Prospecting*, 54(2):121–133.

[26] Castillo, J. E. and Miranda, G. F. (2013). *Mimetic discretization methods*. CRC Press.

[27] Chen, H. and Niu, Q. (2021). Influence of subsurface heterogeneity on critical zone characterizations with electrical resistivity and seismic refraction tomography. In *Sixth International Conference on Engineering Geophysics, Virtual, 25–28 October 2021*, pages 213–216. Society of Exploration Geophysicists.

[28] Coggon, J. (1971). Electromagnetic and electrical modeling by the finite element method. *Geophysics*, 36(1):132–155.

[29] da Veiga, L. B., Lipnikov, K., and Manzini, G. (2014). *The mimetic finite difference method for elliptic problems*, volume 11. Springer.

[30] Dahlin, T. (2001). The development of DC resistivity imaging techniques. *Computers & Geosciences*, 27(9):1019–1029.

[31] Dahlin, T. and Zhou, B. (2004). A numerical comparison of 2D resistivity imaging with 10 electrode arrays. *Geophysical prospecting*, 52(5):379–398.

[32] Dai, S.-K., Ling, J.-X., Chen, Q.-R., Li, K., Zhang, Q.-J., Zhao, D.-D., and Zhang, Y. (2021). Numerical modeling of 3D DC resistivity method in the mixed space-wavenumber domain. *Applied Geophysics*, 18(3):361–374.

[33] Daily, W., Ramirez, A., Binley, A., and LeBrecque, D. (2004). Electrical resistance tomography. *The Leading Edge*, 23(5):438–442.

[34] de la Puente, J., Ferrer, M., Hanzich, M., Castillo, J. E., and Cela, J. M. (2014). Mimetic seismic wave modeling including topography on deformed staggered grids. *Geophysics*, 79(3):T125–T141.

[35] Demirci, I., Erdoğan, E., and Candansayar, M. E. (2012). Two-dimensional inversion of direct current resistivity data incorporating topography by using finite difference techniques with triangle cells: Investigation of kera fault zone in western crete. *Geophysics*, 77(1):E67–E75.

[36] Dey, A. and Morrison, H. (1979a). Resistivity modelling for arbitrarily shaped two-dimensional structures. *Geophysical prospecting*, 27(1):106–136.

[37] Dey, A. and Morrison, H. F. (1979b). Resistivity modeling for arbitrarily shaped three-dimensional structures. *Geophysics*, 44(4):753–780.

[38] Edwards, L. (1977). A modified pseudosection for resistivity and IP. *Geophysics*, 42(5):1020–1036.

[39] Eppelbaum, L. V. (2000). Applicability of geophysical methods for localization of archaeological targets: An introduction. *Geoinformatics*, 11(1):25–34.

[40] Erdoğan, E., Demirci, I., and Candansayar, M. E. (2008). Incorporating topography into 2D resistivity modeling using finite-element and finite-difference approaches. *Geophysics*, 73(3):F135–F142.

[41] Fox, L. (1979). Finite differences and singularities in elliptic problems. *A survey of numerial methods for partial differential equations*, pages 43–68.

[42] Fox, R. C., Hohmann, G. W., Killpack, T. J., and Rijo, L. (1980). Topographic effects in resistivity and induced-polarization surveys. *Geophysics*, 45(1):75–93.

[43] Galetti, E. and Curtis, A. (2018). Transdimensional electrical resistivity tomography. *Journal of Geophysical Research: Solid Earth*, 123(8):6347–6377.

[44] Galis, M., Moczo, P., and Kristek, J. (2008). A 3-D hybrid finite-difference—finite-element viscoelastic modelling of seismic wave motion. *Geophysical Journal International*, 175(1):153–184.

[45] Greenhalgh, M. S. (2009). *DC resistivity modelling and sensitivity analysis in anisotropic media.* PhD thesis, University of Adelaide.

[46] Greenhalgh, S., Marescot, L., Zhou, B., Greenhalgh, M., and Wiese, T. (2009). Electric potential and fréchet derivatives for a uniform anisotropic medium with a tilted axis of symmetry. *Pure and applied geophysics*, 166:673–699.

[47] Greenhalgh, S., Wiese, T., and Marescot, L. (2010). Comparison of DC sensitivity patterns for anisotropic and isotropic media. *Journal of Applied Geophysics*, 70(2):103–112.

[48] Griffiths, D. and Barker, R. (1993). Two-dimensional resistivity imaging and modelling in areas of complex geology. *Journal of Applied Geophysics*, 29(3-4):211–226.

[49] Gündoğdu, N. Y. and Candansayar, M. E. (2018). Three-dimensional regularized inversion of DC resistivity data with different stabilizing functionals. *Geophysics*, 83(6):E399–E407.

[50] Günther, T. (2004). *Inversion methods and resolution analysis for the 2D/3D reconstruction of resistivity structures from DC measurements.* PhD thesis, Freiberg University of Mining and Technology.

[51] Günther, T., Rücker, C., and Spitzer, K. (2006). Three-dimensional modelling and inversion of DC resistivity data incorporating topography—II. Inversion. *Geophysical Journal International*, 166(2):506–517.

[52] Gustafson, K. and Abe, T. (1998). The third boundary condition—was it robin's? *The Mathematical Intelligencer*, 20:63–71.

[53] Habberjam, G. (1972). The effects of anisotropy on square array resistivity measurements. *Geophysical prospecting*, 20(2):249–266.

[54] Habberjam, G. (1975). Apparent resistivity, anisotropy and strike measurements. *Geophysical prospecting*, 23(2):211–247.

[55] Hauck, C., Mühll, D. V., and Maurer, H. (2003). Using DC resistivity tomography to detect and characterize mountain permafrost. *Geophysical prospecting*, 51(4):273–284.

[56] Herwanger, J., Pain, C., Binley, A., De Oliveira, C., and Worthington, M. (2004). Anisotropic resistivity tomography. *Geophysical Journal International*, 158(2):409–425.

[57] Hou, J., Mallan, R. K., and Torres-Verdín, C. (2006). Finite-difference simulation of borehole EM measurements in 3D anisotropic media using coupled scalar-vector potentials. *Geophysics*, 71(5):G225–G233.

[58] Hu, D., Tezkan, B., Yue, M., Yang, X., Wu, X., and Zhou, G. (2021). Prediction of conductive anomalies ahead of the tunnel by the 3D-resitivity forward modeling in the whole space. *Geofluids*, 2021:1–12.

[59] Hvoždara, M. and Kaikkonen, P. (1998). An integral equations solution of the forward DC geoelectric problem for a 3-D body of inhomogeneous conductivity buried in a halfspace. *Journal of Applied Geophysics*, 39(2):95–107.

[60] Hyman, J., Morel, J., Shashkov, M., and Steinberg, S. (2002). Mimetic finite difference methods for diffusion equations. *Computational Geosciences*, 6:333–352.

[61] Hyman, J., Shashkov, M., and Steinberg, S. (1997). The numerical solution of diffusion problems in strongly heterogeneous non-isotropic materials. *Journal of Computational Physics*, 132(1):130–148.

[62] Hyman, J., Shashkov, M., and Steinberg, S. (2001). The effect of inner products for discrete vector fields on the accuracy of mimetic finite difference methods. *Computers & Mathematics with Applications*, 42(12):1527–1547.

[63] Hyman, J. M., Knapp, R. J., and Scovel, J. C. (1992). High order finite volume approximations of differential operators on nonuniform grids. *Physica D: Nonlinear Phenomena*, 60(1-4):112–138.

[64] Hyman, J. M. and Shashkov, M. (1997a). Adjoint operators for the natural discretizations of the divergence, gradient and curl on logically rectangular grids. *Applied Numerical Mathematics*, 25(4):413–442.

[65] Hyman, J. M. and Shashkov, M. (1997b). Natural discretizations for the divergence, gradient, and curl on logically rectangular grids. *Computers & Mathematics with Applications*, 33(4):81–104.

[66] Hyman, J. M. and Shashkov, M. (1998). Approximation of boundary conditions for mimetic finite-difference methods. *Computers & Mathematics with Applications*, 36(5):79–99.

[67] Hyman, J. M. and Shashkov, M. (1999a). Mimetic discretizations for maxwell's equations. *Journal of Computational Physics*, 151(2):881–909.

[68] Hyman, J. M. and Shashkov, M. (1999b). The orthogonal decomposition theorems for mimetic finite difference methods. *SIAM Journal on Numerical Analysis*, 36(3):788–818.

[69] Hyodo, D., Goto, T.-n., Mikada, H., and Takekawa, J. (2013). Pseudo resistivity cross section imaging using VLF-EM data. In *Proceedings of the 11th SEGJ International Symposium, Yokohama, Japan, 18-21 November 2013*, pages 76–79. Society of Exploration Geophysicists of Japan.

[70] Jahandari, H. and Bihlo, A. (2021). Forward modelling of geophysical electromagnetic data on unstructured grids using an adaptive mimetic finite-difference method. *Computational Geosciences*, 25:1083–1104.

[71] Jahandari, H., Bihlo, A., and Donzelli, F. (2021). Forward modelling of gravity data on unstructured grids using an adaptive mimetic finite-difference method. *Journal of Applied Geophysics*, 190:104340.

[72] Jayawickreme, D. H., Van Dam, R. L., and Hyndman, D. W. (2008). Subsurface imaging of vegetation, climate, and root-zone moisture interactions. *Geophysical research letters*, 35(18).

[73] Jianfeng, Z. and Tielin, L. (2002). Elastic wave modelling in 3D heterogeneous media: 3D grid method. *Geophysical Journal International*, 150(3):780–799.

[74] Jing-Tian, T., Wang, F.-Y., and Ren, Z.-Y. (2010). 2.5-d DC resistivity modeling by adaptive finite-element method with unstructured triangulation. *Chinese Journal of Geophysics*, 53(3):708–716.

[75] Kana, J. D., Djongyang, N., Raïdandi, D., Nouck, P. N., and Dadjé, A. (2015). A review of geophysical methods for geothermal exploration. *Renewable and Sustainable Energy Reviews*, 44:87–95.

[76] Karous, M. and Pernu, T. (1985). Combined sounding-profiling resistivity measurements with the three-electrode arrays. *Geophysical Prospecting*, 33(3):447–459.

[77] Kim, J.-H., Yi, M.-J., Cho, S.-J., Son, J.-S., and Song, W.-K. (2006). Anisotropic crosshole resistivity tomography for ground safety analysis of a high-storied building over an abandoned mine. *Environmental and Engineering Geophysics*, 11(4):225–235.

[78] Knödel, K., Lange, G., Voigt, H.-J., Seidel, K., and Lange, G. (2007). Direct current resistivity methods. *Environmental geology: handbook of field methods and case studies*, pages 205–237.

[79] Kuznetsov, Y., Lipnikov, K., and Shashkov, M. (2004). The mimetic finite difference method on polygonal meshes for diffusion-type problems. *Computational Geosciences*, 8:301–324.

[80] Lashkaripour, G. R. (2003). An investigation of groundwater condition by geoelectrical resistivity method: A case study in korin aquifer, southeast Iran. *Journal of Spatial Hydrology*, 3(2).

[81] Li, J.-J., Yan, J.-B., and Huang, X.-Y. (2015a). Precision of meshfree methods and application to forward modeling of two-dimensional electromagnetic sources. *Applied Geophysics*, 12(4):503–515.

[82] Li, P. and Stagnitti, F. (2004). Direct current electric potential in an anisotropic half-space with vertical contact containing a conductive 3D body. *Mathematical Problems in Engineering*, 2004(1):63–77.

[83] Li, P. and Uren, N. (1997). Analytical solution for the point source potential in an anisotropic 3-D half-space I: two-horizontal-layer case. *Mathematical and Computer Modelling*, 26(5):9–27.

[84] Li, S., Liu, B., Nie, L., Liu, Z., Tian, M., Wang, S., Su, M., and Guo, Q. (2015b). Detecting and monitoring of water inrush in tunnels and coal mines using direct current resistivity method: a review. *Journal of Rock Mechanics and Geotechnical Engineering*, 7(4):469–478.

[85] Li, Y. and Pek, J. (2008). Adaptive finite element modelling of two-dimensional magnetotelluric fields in general anisotropic media. *Geophysical Journal International*, 175(3):942–954.

[86] Li, Y. and Spitzer, K. (2002). Three-dimensional DC resistivity forward modelling using finite elements in comparison with finite-difference solutions. *Geophysical Journal International*, 151(3):924–934.

[87] Li, Y. and Spitzer, K. (2005). Finite element resistivity modelling for three-dimensional structures with arbitrary anisotropy. *Physics of the Earth and Planetary Interiors*, 150(1-3):15–27.

[88] Lipnikov, K., Morel, J., and Shashkov, M. (2004). Mimetic finite difference methods for diffusion equations on non-orthogonal non-conformal meshes. *Journal of Computational Physics*, 199(2):589–597.

[89] Loke, M. (2000). Topographic modelling in electrical imaging inversion. In *EAGE 62nd Conf. Tech. Exhib. Glas. Scotland*, pages 62–65.

[90] Loke, M., Chambers, J., Rucker, D., Kuras, O., and Wilkinson, P. (2013). Recent developments in the direct-current geoelectrical imaging method. *Journal of Applied Geophysics*, 95:135–156.

[91] Lowry, T., Allen, M., and Shive, P. N. (1989). Singularity removal: A refinement of resistivity modeling techniques. *Geophysics*, 54(6):766–774.

[92] Lüling, M. G. (2013). The paradox of anisotropy in electric logging: A simple proof and extensions to other physics domains. *Geophysics*, 78(1):W1–W8.

[93] Ma, C., Liu, J., Guo, Z., Guo, R., and Liu, H. (2018). An element-free galerkin method based on adaptive background cells for 2.5 D DC resistivity modeling. In *SEG International Exposition and Annual Meeting*, pages SEG–2018. SEG.

[94] Maillet, R. and Doll, H. (1932). Sur un théorème relatif aux milieux électriquement anisotropes et ses applications à la prospection électrique en courant continu. *Ergänzungshefte für angewandte Geophysik*, 3:109–124.

[95] Margolin, L. G., Shashkov, M., and Smolarkiewicz, P. K. (2000). A discrete operator calculus for finite difference approximations. *Computer methods in applied mechanics and engineering*, 187(3-4):365–383.

[96] Martínez, J. L. F., Gonzalo, E. G., Álvarez, J. P. F., Kuzma, H. A., and Pérez, C. O. M. (2010). Pso: A powerful algorithm to solve geophysical inverse problems: Application to a 1D-DC resistivity case. *Journal of Applied Geophysics*, 71(1):13–25.

[97] Matias, M. S. (2002). Square array anisotropy measurements and resistivity sounding interpretation. *Journal of Applied Geophysics*, 49(3):185–194.

[98] McGillivray, P. R. (1992). *Forward modeling and inversion of DC resistivity and MMR data*. PhD thesis, University of British Columbia.

[99] Moran, J. and Gianzero, S. (1979). Effects of formation anisotropy on resistivity-logging measurements. *Geophysics*, 44(7):1266–1286.

[100] Morel, J., Hall, M. L., and Shashkov, M. J. (2001). A local support-operators diffusion discretization scheme for hexahedral meshes. *Journal of Computational Physics*, 170(1):338–372.

[101] Morel, J., Roberts, R. M., and Shashkov, M. J. (1998). A local support-operators diffusion discretization scheme for quadrilateralr-zmeshes. *Journal of Computational Physics*, 144(1):17–51.

[102] Mukesh, M., Sarkar, K., and Singh, U. (2021). Joint inversion of MT and DC resistivity using meta-heuristic algorithm with gibb's sampler. In *82nd EAGE Annual Conference & Exhibition*, volume 2021, pages 1–5. European Association of Geoscientists & Engineers.

[103] Niklas, L. and Pedersen, L. B. (2004). Evidence of electrical anisotropy in limestone formations using the RMT technique. *Geophysics*, 69(4):909–916.

[104] Oldenburg, D. and Pratt, D. (2007). Geophysical inversion for mineral exploration: A decade of progress in theory and practice. In *Proceedings of exploration*, volume 7, pages 61–95.

[105] Oldenburg, D. W., Li, Y., and Ellis, R. G. (1997). Inversion of geophysical data over a copper gold porphyry deposit; a case history for mt. milligan. *Geophysics*, 62(5):1419–1431.

[106] Osiadacz, A. J. and Yedroudj, M. (1989). A comparison of a finite element method and a finite difference method for transient simulation of a gas pipeline. *Applied mathematical modelling*, 13(2):79–85.

[107] Ozegin, K., Oseghale, A., Audu, A., and Ofotokun, E. (2013). An application of the 2–D DC resistivity method in building site investigation—a case study: Southsouth nigeria. *Journal of Environment and Earth Science*, 3(2):108–112.

[108] Pain, C. C., Herwanger, J. V., Saunders, J. H., Worthington, M. H., and de Oliveira, C. R. (2003). Anisotropic resistivity inversion. *Inverse Problems*, 19(5):1081.

[109] Pan, K. and Tang, J. (2014). 2.5-d and 3-D DC resistivity modelling using an extrapolation cascadic multigrid method. *Geophysical Journal International*, 197(3):1459–1470.

[110] PAN, K.-J., WANG, W.-J., TAN, Y.-J., and CAO, J.-X. (2009). Geophysical linear inversion based on hybrid differential evolution algorithm. *Chinese Journal of Geophysics*, 52(12):3083–3090.

[111] Pawlik, Ł. and Kasprzak, M. (2018). Regolith properties under trees and the biomechanical effects caused by tree root systems as recognized by electrical resistivity tomography (ERT). *Geomorphology*, 300:1–12.

[112] Penz, S., Chauris, H., Donno, D., and Mehl, C. (2013). Resistivity modelling with topography. *Geophysical Journal International*, 194(3):1486–1497.

[113] Pidlisecky, A. and Knight, R. (2008). Fw2_5d: A MATLAB 2.5-D electrical resistivity modeling code. *Computers & Geosciences*, 34(12):1645–1654.

[114] Pridmore, D., Hohmann, G., Ward, S., and Sill, W. (1981). An investigation of finite-element modeling for electrical and electromagnetic data in three dimensions. *Geophysics*, 46(7):1009–1024.

[115] Queralt, P., Pous, J., and Marcuello, A. (1991). 2-D resistivity modeling: An approach to arrays parallel to the strike direction. *Geophysics*, 56(7):941–950.

[116] Ren, Z., Qiu, L., Tang, J., Wu, X., Xiao, X., and Zhou, Z. (2018). 3-D direct current resistivity anisotropic modelling by goal-oriented adaptive finite element methods. *Geophysical Journal International*, 212(1):76–87.

[117] Ren, Z. and Tang, J. (2014). A goal-oriented adaptive finite-element approach for multi-electrode resistivity system. *Geophysical Journal International*, 199(1):136–145.

[118] Rojas, O., Day, S., Castillo, J., and Dalguer, L. A. (2008). Modelling of rupture propagation using high-order mimetic finite differences. *Geophysical Journal International*, 172(2):631–650.

[119] Rojas, S., Muga, I., and Pardo, D. (2016). A quadrature-free method for simulation and inversion of 1.5 D direct current (DC) borehole measurements. *Computational Geosciences*, 20:1301–1318.

[120] Rücker, C., Günther, T., and Spitzer, K. (2006). Three-dimensional modelling and inversion of dc resistivity data incorporating topography—I. Modelling. *Geophysical Journal International*, 166(2):495–505.

[121] Rühlow, A., Tezkan, B., and de Lima, O. L. (1998). DC resistivity and time-domain induced polarization survey for the study of ground-water contamination in bahia, brazil. In *4th EEGS Meeting*, pages cp–43. European Association of Geoscientists & Engineers.

[122] Samarskii, A., Tishkin, V., Favorskii, A., and Shashkov, M. Y. (1981). Operational finite-difference schemes. *Differential Equations*, 17(7):854–862.

[123] Sen, M. K., Bhattacharya, B. B., and Stoffa, P. L. (1993). Nonlinear inversion of resistivity sounding data. *Geophysics*, 58(4):496–507.

[124] Sethi, H., Shragge, J., and Tsvankin, I. (2021). Mimetic finite-difference coupled-domain solver for anisotropic media. *Geophysics*, 86(1):T45–T59.

[125] Shahriari, M., Rojas, S., Pardo, D., Rodríguez-Rozas, A., Bakr, S. A., Calo, V. M., and Muga, I. (2018). A numerical 1.5 D method for the rapid simulation of geophysical resistivity measurements. *Geosciences*, 8(6):225.

[126] Sharma, S. P. (2012). VFSARES—a very fast simulated annealing FORTRAN program for interpretation of 1-D DC resistivity sounding data from various electrode arrays. *Computers & Geosciences*, 42:177–188.

[127] Shashkov, M. (2018). *Conservative finite-difference methods on general grids*. CRC press.

[128] Shashkov, M. and Steinberg, S. (1995). Support-operator finite-difference algorithms for general elliptic problems. *Journal of Computational Physics*, 118(1):131–151.

[129] Shashkov, M. and Steinberg, S. (1996). Solving diffusion equations with rough coefficients in rough grids. *Journal of Computational Physics*, 129(2):383–405.

[130] Simpson, M. and Clement, T. (2003). Comparison of finite difference and finite element solutions to the variably saturated flow equation. *Journal of hydrology*, 270(1-2):49–64.

[131] Singh, A., Mishra, P. K., and Sharma, S. (2019). 2D cooperative inversion of direct current resistivity and gravity data: A case study of uranium bearing target rock. *Geophysical Prospecting*, 67(3):696–708.

[132] Singh, U., Tiwari, R., and Singh, S. (2010). Inversion of 2-D DC resistivity data using rapid optimization and minimal complexity neural network. *Nonlinear Processes in Geophysics*, 17(1):65–76.

[133] Singh, U. K., Tiwari, R. K., and Singh, S. (2013). Neural network modeling and prediction of resistivity structures using VES schlumberger data over a geothermal area. *Computers & Geosciences*, 52:246–257.

[134] Sirota, D., Shragge, J., Krahenbuhl, R., Swidinsky, A., Yalo, N., and Bradford, J. (2022). Development and validation of a low-cost direct current resistivity meter for humanitarian geophysics applications. *Geophysics*, 87(1):WA1–WA14.

[135] Spitzer, K. (1995). A 3-D finite-difference algorithm for DC resistivity modelling using conjugate gradient methods. *Geophysical Journal International*, 123(3):903–914.

[136] Srigutomo, W., Anwar, H., Agustine, E., and Mahardika, H. (2019). Three-dimensional DC resistivity modeling using galerkin finite element method composed by tetrahedral elements. *Journal of Engineering & Technological Sciences*, 51(4).

[137] Storn, R. and Price, K. (1997). Differential evolution–a simple and efficient heuristic for global optimization over continuous spaces. *Journal of global optimization*, 11:341–359.

[138] Sun, Z., Sun, J., and Zhang, D. (2009). 2D DC electric field numerical modeling including surface topography using coordinate transformation method. *Journal of Jilin University: Earth Science Edition*, 39(3):528–534.

[139] Suryavanshi, D. and Dehiya, R. (2023). A mimetic finite-difference method for two-dimensional dc resistivity modeling. *Mathematical Geosciences*, pages 1–28.

[140] Tang, J., Wang, F., Xiao, X., and Zhang, L. (2011). 2.5-D DC resistivity modeling considering flexibility and accuracy. *Journal of Earth Science*, 22(1):124–130.

[141] Tao, S., Yun, L., Yun, W., and Bin, L. (2021). Numerical modeling of anisotropy paradoxes in direct current resistivity and time-domain induced polarization methods. *Applied Geophysics*, 18(1):117–127.

[142] Taylor, R. W. and Fleming, A. H. (1988). Characterizing jointed systems by azimuthal resistivity surveys. *Groundwater*, 26(4):464–474.

[143] Telford, W. M., Geldart, L. P., and Sheriff, R. E. (1990). *Applied Geophysics*. Cambridge university press.

[144] Tsourlos, P. I., Szymanski, J. E., and Tsokas, G. N. (1999). The effect of terrain topography on commonly used resistivity arrays. *Geophysics*, 64(5):1357–1363.

[145] Ulugergerli, E. U. (2011). Two dimensional combined inversion of short-and long-normal dc resistivity well log data. *Journal of Applied Geophysics*, 73(2):130–138.

[146] Vachiratienchai, C., Boonchaisuk, S., and Siripunvaraporn, W. (2010). A hybrid finite difference–finite element method to incorporate topography for 2D direct current (DC) resistivity modeling. *Physics of the Earth and Planetary Interiors*, 183(3-4):426–434.

[147] Vachiratienchai, C. and Siripunvaraporn, W. (2013). An efficient inversion for two-dimensional direct current resistivity surveys based on the hybrid finite difference–finite element method. *Physics of the Earth and Planetary Interiors*, 215:1–11.

[148] Varfinezhad, R. and Oskooi, B. (2020). 2D DC resistivity forward modeling based on the integral equation method and a comparison with the res2dmod results. *Journal of the Earth and Space Physics*, 45(4):43.

[149] Verma, S. and Sharma, S. (1993). Resolution of thin layers using joint-inversion of electromagnetic and direct current resistivity sounding data. *Journal of electromagnetic waves and applications*, 7(3):443–479.

[150] Wait, J. R. (1990). Current flow into a three-dimensionally anisotropic conductor. *Radio Science*, 25(5):689–694.

[151] Wang, T. and Fang, S. (2001). 3-D electromagnetic anisotropy modeling using finite differences. *Geophysics*, 66(5):1386–1398.

[152] Wang, W., Wu, X., and Spitzer, K. (2013). Three-dimensional DC anisotropic resistivity modelling using finite elements on unstructured grids. *Geophysical Journal International*, 193(2):734–746.

[153] Watson, K. A. and Barker, R. D. (1999). Differentiating anisotropy and lateral effects using azimuthal resistivity offset wenner soundings. *Geophysics*, 64(3):739–745.

[154] Wiese, T., Greenhalgh, S., and Marescot, L. (2009). DC resistivity sensitivity patterns for tilted transversely isotropic media. *Near Surface Geophysics*, 7(2):125–139.

[155] Wilhelms, W., Schwarzbach, C., Caudillo-Mata, L. A., and Haber, E. (2018). The mimetic multiscale method for maxwell's equations. *Geophysics*, 83(5):E259–E276.

[156] Wu, X., Xiao, Y., Qi, C., and Wang, T. (2003). Computations of secondary potential for 3D DC resistivity modelling using an incomplete choleski conjugate-gradient method. *Geophysical Prospecting*, 51(6):567–577.

[157] Xu, S.-z., Duan, B.-c., and Zhang, D.-h. (2000). Selection of the wavenumbers k using an optimization method for the inverse fourier transform in 2.5 D electrical modelling. *Geophysical Prospecting*, 48(5):789–796.

[158] Xu, S.-z., Gao, Z., and Zhao, S.-k. (1988). An integral formulation for three-dimensional terrain modeling for resistivity surveys. *Geophysics*, 53(4):546–552.

[159] Yan, B., Li, Y., and Liu, Y. (2016). Adaptive finite element modeling of direct current resistivity in 2-D generally anisotropic structures. *Journal of Applied Geophysics*, 130:169–176.

[160] Yang, J., Liu, Y., and Wu, X. (2017). 3-D DC resistivity modelling with arbitrary long electrode sources using finite element method on unstructured grids. *Geophysical Journal International*, 211(2):1162–1176.

[161] Yang, Z., Yin, C., Ren, X., and Cao, C. Q. X. (2018). Research on DC resistivity for an arbitrarily anisotropic earth using circular scanning measurement. *ASEG Extended Abstracts*, 2018(1):1–7.

[162] Yaoguo, L. and Oldenburg, D. W. (1994). Inversion of 3-D DC resistivity data using an approximate inverse mapping. *Geophysical journal international*, 116(3):527–537.

[163] Yi, M.-J., Kim, J.-H., and Son, J.-S. (2011). Three-dimensional anisotropic inversion of resistivity tomography data in an abandoned mine area. *Exploration Geophysics*, 42(1):7–17.

[164] Yin, C. and Maurer, H.-M. (2001). Electromagnetic induction in a layered earth with arbitrary anisotropy. *Geophysics*, 66(5):1405–1416.

[165] Yin, C. and Weidelt, P. (1999). Geoelectrical fields in a layered earth with arbitrary anisotropy. *Geophysics*, 64(2):426–434.

[166] Yuan, Y., Qiang, J., Tang, J., Ren, Z., and Xiao, X. (2016). 2.5 D direct-current resistivity forward modelling and inversion by finite-element–infinite-element coupled method. *Geophysical Prospecting*, 64(3):767–779.

[167] Zhan, Q., Fang, Y., Zhuang, M., Yuan, M., and Liu, Q. H. (2020). Stabilized DG-PSTD method with nonconformal meshes for electromagnetic waves. *IEEE Transactions on Antennas and Propagation*, 68(6):4714–4726.

[168] Zhao, S. and Yedlin, M. J. (1996). Some refinements on the finite-difference method for 3-D dc resistivity modeling. *Geophysics*, 61(5):1301–1307.

[169] Zhdanov, M. S., Lee, S. K., and Yoshioka, K. (2006). Integral equation method for 3D modeling of electromagnetic fields in complex structures with inhomogeneous background conductivity. *Geophysics*, 71(6):G333–G345.

[170] Zhou, B., Greenhalgh, M., and Greenhalgh, S. (2009). 2.5-D/3-D resistivity modelling in anisotropic media using Gaussian quadrature grids. *Geophysical Journal International*, 176(1):63–80.

[171] Zhou, Z. and Keller, S. M. (2019). The application of least-squares finite-element method to simulate wave propagation in bianisotropic media. *IEEE Transactions on Antennas and Propagation*, 67(4):2574–2582.

[172] Zienkiewicz, O. and Cheung, Y. (1965). Finite elements in the solution of field problems. *The Engineer*, 220(5722):507–510.

[173] Zohdy, A. A. (1969). A new method for differential resistivity sounding. *Geophysics*, 34(6):924–943.

Appendix A

Discretised form of differential operators for mimetic scheme

Without loss of generality and to keep the notations simple, let us consider that we are trying to discretise a problem of this form : $\nabla \cdot [T_{2D}(x,z)\nabla u(x,k,z)]$. The z-direction is taken positive downwards. The discretised form of the differential operator in Eq. (2.11), using the mimetic finite difference method can be given as,

$$
\begin{aligned}
&\nabla \cdot [T_{2D}\nabla u]_{i,j} = \\
&\frac{z_{i+1,j}-z_{i,j+1}}{2CV_{i,j}} * \{\sigma_{xx(i+1,j+1)}[((z_{i+2,j+1}-z_{i+1,j+2})u_{i+1,j+1}+ \\
&(z_{i+1,j+2}-z_{i,j+1})u_{i,j+1}+(z_{i,j+1}-z_{i+1,j})u_{i,j}+ \\
&(z_{i+1,j}-z_{i+2,j+1})u_{i+1,j})/(2NV_{i+1,j+1})]- \\
&\sigma_{xz(i+1,j+1)}[((x_{i+1,j+2}-x_{i+2,j+1})u_{i+1,j+1}+ \\
&(x_{i,j+1}-x_{i+1,j+2})u_{i,j+1}+(x_{i+1,j}-x_{i,j+1})u_{i,j}+ \\
&(x_{i+2,j+1}-x_{i+1,j})u_{i+1,j})/(2NV_{i+1,j+1})]- \\
&\sigma_{xx(i,j)}[((z_{i+1,j}-z_{i,j+1})u_{i,j}+(z_{i,j+1}-z_{i-1,j})u_{i-1,j}+ \\
&(z_{i-1,j}-z_{i,j-1})u_{i-1,j-1}+(z_{i,j-1}-z_{i+1,j})u_{i,j-1})/(2NV_{i,j})]+ \\
&\sigma_{xz(i,j)}[((x_{i,j+1}-x_{i+1,j})u_{i,j}+(x_{i-1,j}-x_{i,j+1})u_{i-1,j}+ \\
&(x_{i,j-1}-x_{i-1,j})u_{i-1,j-1}+(x_{i+1,j}-x_{i,j-1})u_{i,j-1})/(2NV_{i,j})]\}-
\end{aligned}
$$

$$\frac{z_{i,j}-z_{i+1,j+1}}{2CV_{i,j}} * \{\sigma_{xx(i,j+1)}[((z_{i+1,j+1}-z_{i,j+2})u_{i,j+1}+$$
$$(z_{i,j+2}-z_{i-1,j+1})u_{i-1,j+1}+(z_{i-1,j+1}-z_{i,j})u_{i-1,j}+$$
$$(z_{i,j}-z_{i+1,j+1})u_{i,j})/(2NV_{i,j+1})]-$$
$$\sigma_{xz(i,j+1)}[((x_{i,j+2}-x_{i+1,j+1})u_{i,j+1}+(x_{i-1,j+1}-x_{i,j+2})u_{i-1,j+1}+$$
$$(x_{i,j}-x_{i-1,j+1})u_{i-1,j}+(x_{i+1,j+1}-x_{i,j})u_{i,j})/(2NV_{i,j+1})]-$$
$$\sigma_{xx(i+1,j}[((z_{i+2,j}-z_{i+1,j+1})u_{i+1,j}+(z_{i+1,j+1}-z_{i,j})u_{i,j}+$$
$$(z_{i,j}-z_{i+1,j-1})u_{i,j-1}+(z_{i+1,j-1}-z_{i+2,j})u_{i+1,j-1})/(2NV_{i+1,j})]+$$
$$\sigma_{xz(i+1,j}[((x_{i+1,j+1}-x_{i+2,j})u_{i+1,j}+(x_{i,j}-x_{i+1,j+1})u_{i,j}+$$
$$(x_{i+1,j-1}-x_{i,j})u_{i,j-1}+(x_{i+2,j}-x_{i+1,j-1})u_{i+1,j-1})/(2NV_{i+1,j})]\}-$$
$$\frac{x_{i,j+1}-x_{i+1,j}}{2CV_{i,j}} * \{\sigma_{xz(i+1,j+1)}[((z_{i+2,j+1}-z_{i+1,j+2})u_{i+1,j+1}+$$
$$(z_{i+1,j+2}-z_{i,j+1})u_{i,j+1}+(z_{i,j+1}-z_{i+1,j})u_{i,j}+$$
$$(z_{i+1,j}-z_{i+2,j+1})u_{i+1,j})/(2NV_{i+1,j+1})]-$$
$$\sigma_{zz(i+1,j+1)}[((x_{i+1,j+2}-x_{i+2,j+1})u_{i+1,j+1}+$$
$$(x_{i,j+1}-x_{i+1,j+2})u_{i,j+1}+(x_{i+1,j}-x_{i,j+1})u_{i,j}+$$
$$(x_{i+2,j+1}-x_{i+1,j})u_{i+1,j})/(2NV_{i+1,j+1})]-$$
$$\sigma_{xz(i,j)}[((z_{i+1,j}-z_{i,j+1})u_{i,j}+(z_{i,j+1}-z_{i-1,j})u_{i-1,j}+$$
$$(z_{i-1,j}-z_{i,j-1})u_{i-1,j-1}+(z_{i,j-1}-z_{i+1,j})u_{i,j-1})/(2NV_{i,j})]+$$
$$\sigma_{zz(i,j)}[((x_{i,j+1}-x_{i+1,j})u_{i,j}+(x_{i-1,j}-x_{i,j+1})u_{i-1,j}+$$
$$(x_{i,j-1}-x_{i-1,j})u_{i-1,j-1}+(x_{i+1,j}-x_{i,j-1})u_{i,j-1})/(2NV_{i,j})]\}-$$
$$\frac{x_{i+1,j+1}-x_{i,j}}{2CV_{i,j}} * \{\sigma_{xz(i,j+1)}[((z_{i+1,j+1}-z_{i,j+2})u_{i,j+1}+$$
$$(z_{i,j+2}-z_{i-1,j+1})u_{i-1,j+1}+(z_{i-1,j+1}-z_{i,j})u_{i-1,j}+$$
$$(z_{i,j}-z_{i+1,j+1})u_{i,j})/(2NV_{i,j+1})]-$$
$$\sigma_{zz(i,j+1)}[((x_{i,j+2}-x_{i+1,j+1})u_{i,j+1}+(x_{i-1,j+1}-x_{i,j+2})u_{i-1,j+1}+$$
$$(x_{i,j}-x_{i-1,j+1})u_{i-1,j}+(x_{i+1,j+1}-x_{i,j})u_{i,j})/(2NV_{i,j+1})]-$$
$$\sigma_{xz(i+1,j}[((z_{i+2,j}-z_{i+1,j+1})u_{i+1,j}+(z_{i+1,j+1}-z_{i,j})u_{i,j}+$$
$$(z_{i,j}-z_{i+1,j-1})u_{i,j-1}+(z_{i+1,j-1}-z_{i+2,j})u_{i+1,j-1})/(2NV_{i+1,j})]+$$
$$\sigma_{zz(i+1,j}[((x_{i+1,j+1}-x_{i+2,j})u_{i+1,j}+(x_{i,j}-x_{i+1,j+1})u_{i,j}+$$
$$(x_{i+1,j-1}-x_{i,j})u_{i,j-1}+(x_{i+2,j}-x_{i+1,j-1})u_{i+1,j-1})/(2NV_{i+1,j})]\}, \tag{A.1}$$

where $CV_{i,j}$ is the area of the cell (i,j) and $NV_{i,j}$ is the nodal volume as described in the main text.

The Robin boundary conditions as given in Eq. (2.16) can be approximated using the mimetic finite difference method as follows:

$$
\begin{aligned}
&[(\sigma_{xx(i,1)}(\frac{z_{i,2}-z_{i+1,1}}{2}u_{i,1}+\frac{z_{i-1,1}-z_{i,2}}{2}u_{i-1,1}+\\
&\qquad\frac{z_{i,1}-z_{i-1,1}}{2}u_{i-1,0}+\frac{z_{i+1,1}-z_{i,1}}{2}u_{i,0})/NV_{i,1}\\
&\quad-\sigma_{xz(i,1)}(\frac{x_{i,2}-x_{i+1,1}}{2}u_{i,1}+\frac{x_{i-1,1}-x_{i,2}}{2}u_{i-1,1}+\\
&\qquad\frac{x_{i,1}-x_{i-1,1}}{2}u_{i-1,0}+\frac{x_{i+1,1}-x_{i,1}}{2}u_{i,0})/NV_{i,1}\\
&\quad+\sigma_{xx(i+1,1)}(\frac{z_{i+1,2}-z_{i+2,1}}{2}u_{1+1,1}+\frac{z_{i,1}-z_{i+1,2}}{2}u_{i,1}+\\
&\qquad\frac{z_{1+1,1}-z_{i,1}}{2}u_{i,0}+\frac{z_{i+2,1}-z_{i+1,1}}{2}u_{i+1,0})/NV_{i+1,1}\\
&\quad-\sigma_{xz(i+1,1)}(\frac{x_{i+1,2}-x_{i+2,1}}{2}u_{i+1,1}+\frac{x_{i,1}-x_{i+1,1}}{2}u_{i,1}+\\
&\frac{x_{i+1,1}-x_{i,1}}{2}u_{i,0}+\frac{x_{i+2,1}-x_{i+1,1}}{2}u_{i+1,0})/NV_{i+1,1}]\frac{z_{i,1}-z_{i+1,1}}{2lx_{i,1}}\\
&\quad-[(\sigma_{xz(i,1)}(\frac{z_{i+1,1}-z_{i,2}}{2}u_{i,1}+\frac{z_{i,2}-z_{i-1,1}}{2}u_{i-1,1}+\\
&\qquad\frac{z_{i-1,1}-z_{i,1}}{2}u_{i-1,0}+\frac{z_{i,1}-z_{i+1,1}}{2}u_{i,0})/NV_{i,1}\\
&\quad-\sigma_{zz(i,1)}(\frac{x_{i,2}-x_{i+1,1}}{2}u_{i,1}+\frac{x_{i-1,1}-x_{i,2}}{2}u_{i-1,1}+\\
&\qquad\frac{x_{i,1}-x_{i-1,1}}{2}u_{i-1,0}+\frac{x_{i+1,1}-x_{i,1}}{2}u_{i,0})/NV_{i,1}\\
&\quad+\sigma_{xz(i+1,1)}(\frac{z_{i+2,1}-z_{i+1,2}}{2}u_{1+1,1}+\frac{z_{i+1,2}-z_{i,1}}{2}u_{i,1}+\\
&\qquad\frac{z_{i,1}-z_{1+1,1}}{2}u_{i,0}+\frac{z_{i+1,1}-z_{i+2,1}}{2}u_{i+1,0})/NV_{i+1,1}\\
&\quad-\sigma_{zz(i+1,1)}(\frac{x_{i+1,2}-x_{i+2,1}}{2}u_{i+1,1}+\frac{x_{i,1}-x_{i+1,1}}{2}u_{i,1}+\\
&\frac{x_{i+1,1}-x_{i,1}}{2}u_{i,0}+\frac{x_{i+2,1}-x_{i+1,1}}{2}u_{i+1,0})/NV_{i+1,1}]\frac{z_{i,1}-z_{i+1,1}}{2ly_{i,1}}\\
&\qquad\eta(\frac{x_{i,1}+x_{i+1,1}}{2},\frac{z_{i,1}+z_{i+1,1}}{2})\;u_{i,0}=\mu(\frac{x_{i,1}+x_{i+1,1}}{2},\frac{z_{i,1}+z_{i+1,1}}{2})
\end{aligned}
\tag{A.2}
$$

Appendix B

Subsurface anisotropy & DC Resistivity data for resistive overburden

B.1 Resistive overburden

This section consists of models where the 2^{nd} layer is more conductive compared to the overburden layer. The first model shown in Fig. B.1 is an isotropic two-layer model, with the resistivity of the first layer and second layer given by $100\,\Omega m$ and $10\,\Omega m$ respectively. The thickness of the first layer is kept as 30 m shown in Fig. B.1. The azimuthal apparent resistivity curves are obtained at varying radial distance from the source location, at radial distances of $5m, 10m, 25m, 50m, 75m, 100m$, and $110m$ from the source. The apparent resistivity curves are shown in Fig. B.2. It is seen that the curves obtained at all the radial distances are concentric circles with varying radius dependent on the apparent resistivity that is being detected. Since the medium is isotropic, conductivity/resistivity values are same in all the directions and hence the curves turn out to be circles, showing no directional-bias in any particular direction. For the first 10 meters, a considerable amount of current is flowing through the first layer, that is reflected in the values of apparent resistivity curves for 5 m, and 10 m. At 25 m radius curve, there is a significant drop in the apparent resistivity values, thereby indicating the passage of current through the second layer. As we reach the radius of 100 m and 110 m from the source, it is observed that the apparent resistivity curves get saturated and there is hardly any change seen in the values. This is possible when the current is passing entirely through the second layer, thereby detecting the second layer.

The second simulation is performed on a tri-axial anisotropic model shown in Fig. B.3. The first layer is isotropic with a resistivity of $100\,\Omega m$ having a thickness of 30 m, and the

second layer has a tri-axial anisotropy with vaues $10\Omega m$, $5\Omega m$, and $2.5\Omega m$ in the x, y and z-directions respectively. The azimuthal apparent resistivity curves obtained for this experiment are shown in Fig. B.4. It is clearly seen that the curves at 5 m and 10 m radius are drawing the information of the 1st layer; inferred from the high apparent resistivity values. And also the curves are circular thereby detecting first isotropic layer clearly. At 25 m and 50 m radius the curves are still circular but the apparent resistivity values have dropped, thereby indicating the influence of the second layer. As we move ahead and observe the curves at 75 m, 100 m and 110 m,it can be clearly seen that the circular nature is lost and the curves have become elliptical in nature. This clearly shows the presence of anisotropy in the second layer. The apparent resistivity values get saturated at 100 m and 110 m radius and there is no further change.

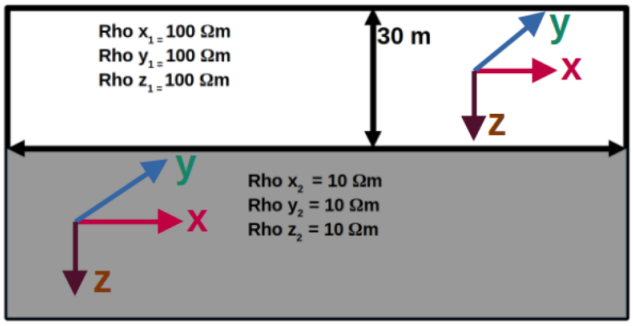

Fig. B.1 The figure shows a two layer isotropic model with resistive overburden of $100\Omega m$. The second layer is an isotropic half-space of $10\Omega m$. The thickness of the first layer is kept at 30 m. Rho x, Rho y, Rho z denote the resistivity values along the principal resistivity directions x, y, and z-directions respectively.

The next set of simulations deals with models having varying degree of rotated anisotropy axis in the $x-z$ plane, referred to as TTI (tilted transverse isotropic) models. The base case model, that is the tri-axial anisotropic model, is shown in Fig. B.3 which can also be referred as TTI 0° case . Subsequent to this, TTI 22.5°, TTI 45°, TTI 67.5°, and TTI 90° are generated, which are shown in Fig. B.5. The previous experiments clearly suggest that there is a saturation of current around 100 m and 110 m radial distance and the curves show the signature of 2nd layer. Hence the apparent resistivity curves for the tri-axial anisotropy cases (i.e TTI 0°), and the other cases of rotation (22.5°, 45°, 67.5°, and 90°) are obtained at 100 m and the corresponding curves are shown in Fig. B.6. It is clearly seen that the curves obtained are elliptic in nature except for the one for 45°, where the curve is nearly circular. It is expected that as the radius increases, the current percolates to deeper depths, thereby sensing the second layer of the model, which in this case is anisotropic. Hence we expect elliptical curves at a radius of 100 m. Another feature that is

noticed is the reversal in the direction of the major and minor-axis of the ellipses formed. As the rotation takes place, the values of resistivity along the principal axis of resistivity also changes. Hence we see a flip in the ellipse at the end-points of rotation, i.e at zero degree rotation and 90° rotation.

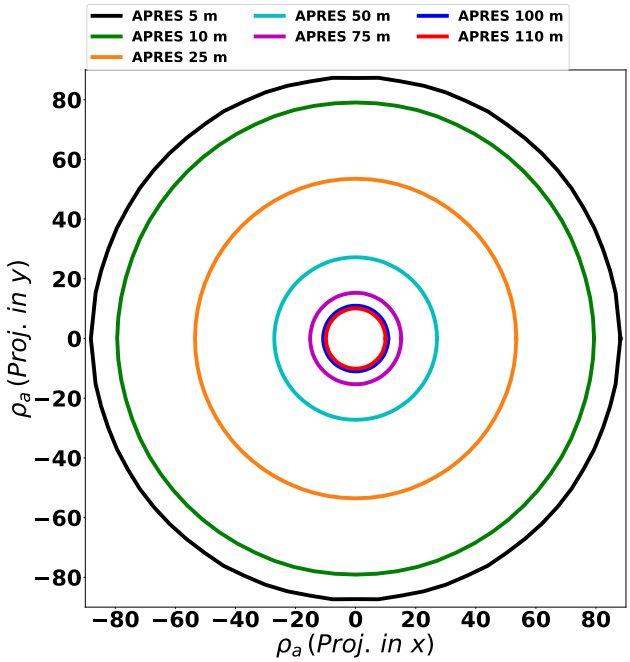

Fig. B.2 Azimuthal apparent resistivity curves obtained for the isotropic model shown in Fig. B.1. The apparent resistivity curves are obtained at increasing radial distance from the source from 5 m to 110 m.

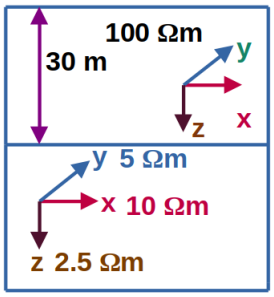

Fig. B.3 The figure shows a tri-axial anisotropic model. The first layer is 30 m thick isotropic layer with resistivity value of $100\,\Omega m$. The second layer is half-space with resistivity values of $10\,\Omega m$, $5\,\Omega m$, and $2.5\,\Omega m$ in the x, y and z-directions respectively.

The 45° TTI case being a special behaviour case, is further probed to understand the behaviour of this model at different distances from the source. Hence we analyze the

azimuthal apparent resistivity curves at varying radial distance from the source. The model and curves are shown in Fig. B.7 (left) and (right) respectively. The curves obtained at 5 m and 10 m bearing high values of apparent resistivity indicates the characteristics of first isotropic layer, and thereby showing the circular nature. There is a decrease in the apparent resistivity values for 25 m, 50 m and 75 m, which shows that the current is also flowing through the second layer, but still the circular nature is maintained. At far offset 100 m and 110 m, where the second anisotropic layer dominates there is a slight deviation from the circular nature of the curves.

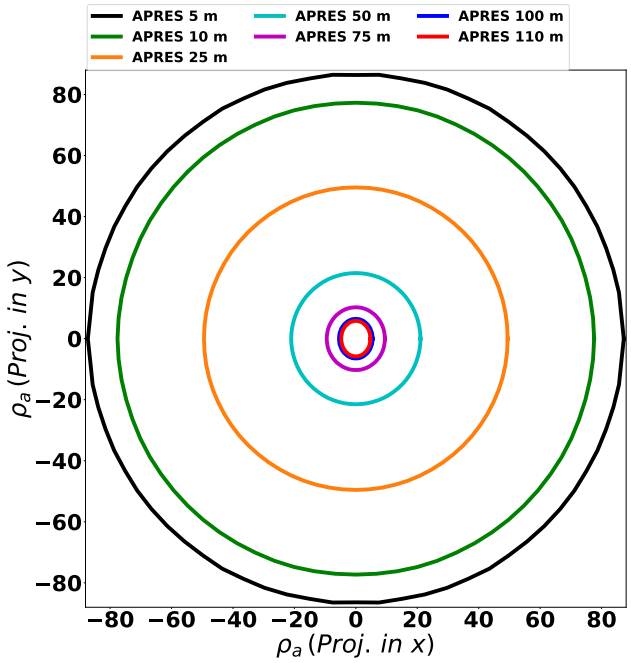

Fig. B.4 The figure shows the azimuthal apparent resistivity curves for tri-axial anisotropic model shown in Fig. B.3 obtained at varying radial distances from the source.

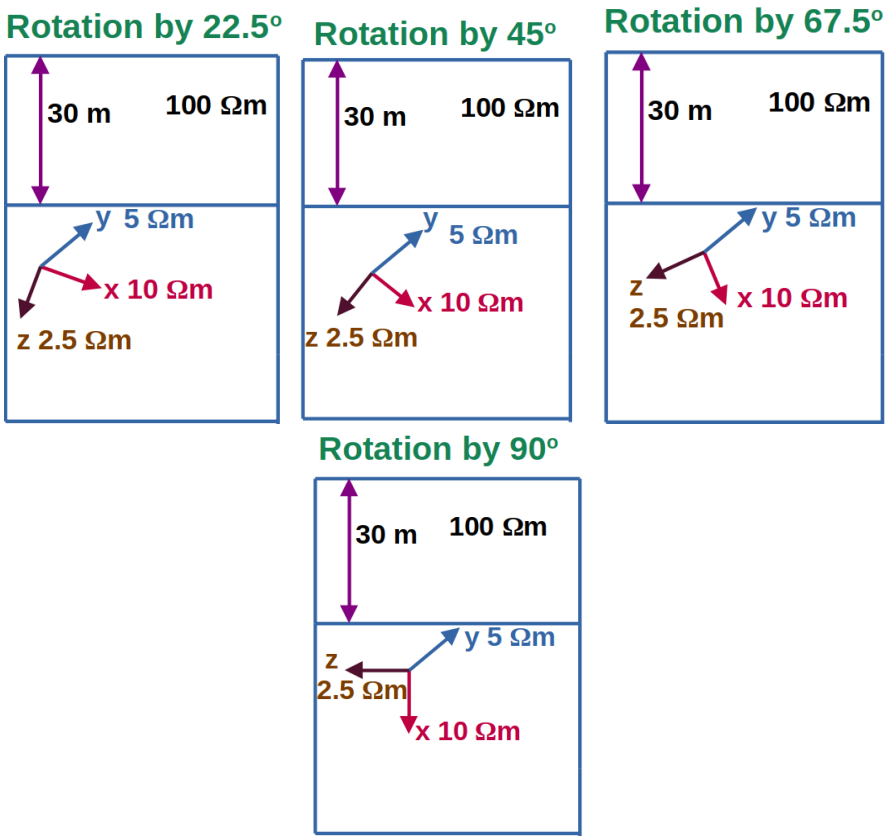

Fig. B.5 The image shows the various models obtained by the rotation of anisotropy axis. On the extreme left the anisotropy axis is rotated by 22.5° in the x-z plane and we refer to this model as TTI 22.5°. Subsequently other models obtained in order are TTI 45°, TTI 67.5°, and TTI 90°.

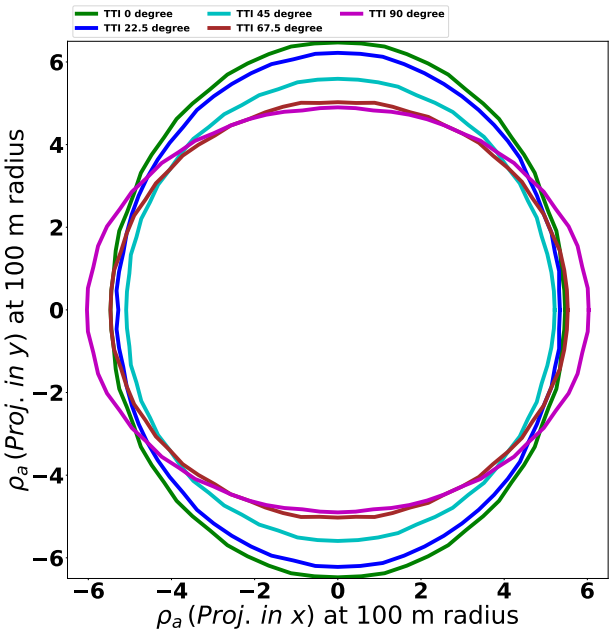

Fig. B.6 The figure shows the azimuthal apparent resistivity curves for TTI 0°, TTI 22.5°, TTI 45°, TTI 67.5°, and TTI 90° at 100 m radial distance.

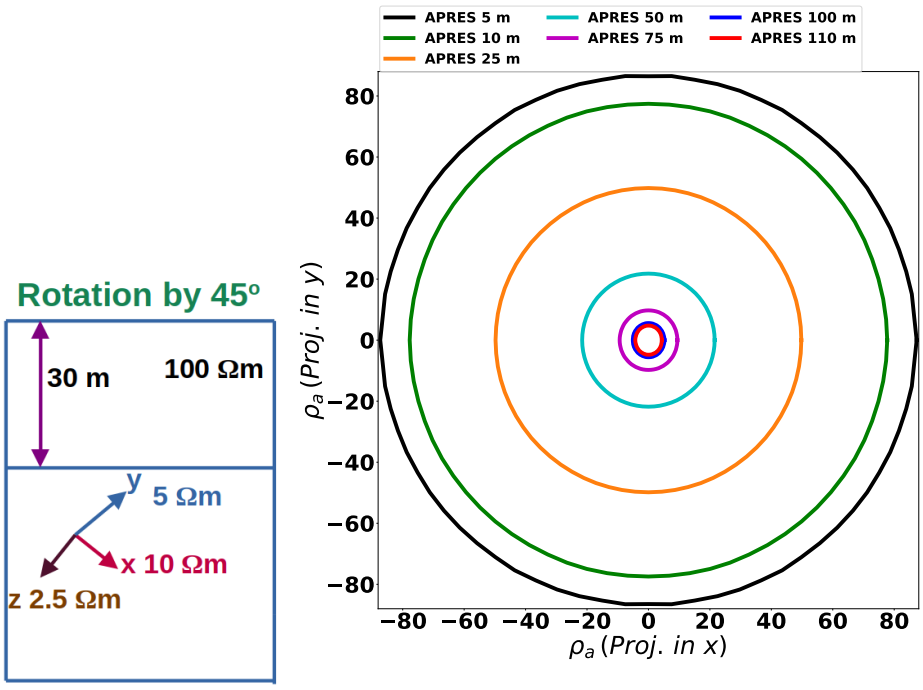

Fig. B.7 The figure shows the model for TTI 45° (left). The corresponding azimuthal apparent resistivity curves obtained are shown on right for increasing radial distances from 5 m to 110 m.